



Università degli Studi di Firenze
Dipartimento di Fisica

Dottorato in Fisica XVII ciclo

**Development of sampling and
digital signal processing techniques
with applications to
Nuclear Physics detectors**

Luigi Bardelli

Supervisore: Prof. Giacomo Poggi

Coordinatore: Prof. Alessandro Cuccoli

January 2005

*"The most exciting phrase to hear in science,
the one that heralds new discoveries,
is not 'Eureka!' but 'That's funny...'"*

Isaac Asimov

DISCLAIMER: No AD Converter, Processor or C++ compiler was injured in the production of this Thesis.

Contents

Acknowledgments	vii
Introduction	ix
1 An overview of detection systems for Heavy-Ion Nuclear Physics experiments	1
1.1 Nuclear Physics in the next decade	1
1.1.1 Isospin effects on nuclear dynamics and thermodynamics	3
1.1.2 Nuclear Structure	4
1.2 Experimental methods	6
1.2.1 Radiation interaction with matter	6
1.2.2 Scintillation detectors	9
1.2.3 Gas detectors	12
1.2.4 Solid-state detectors	12
1.2.5 Pulse-shape analyses	14
1.2.6 Comparison between detector types	15
1.2.7 Analog electronics: high-resolution energy measurements	16
1.2.8 Analog electronics: timing measurements	19
1.3 Requirements for future detection systems	20
2 Sampling systems	23
2.1 Introduction	23
2.2 Analog to digital conversion	24
2.3 Digital to analog conversion	27
2.4 Discrete time signal processing	28
2.4.1 The Fourier and the \mathcal{Z} transforms	28
2.4.2 Sampling and aliasing	30
2.4.3 Sampling and quantization noise	32
2.4.4 FIR and IIR digital filters	34
2.5 Digital signal processors	37

3 Digital signal processing for Nuclear Physics	39
3.1 The choice of an analog to digital converter	40
3.2 Modular DSP electronics	41
3.3 Digital amplitude measurements	44
3.3.1 Event-based and continuously running digital systems	44
3.3.2 Baseline determination	46
3.3.3 Energy measurements with digital shaping	53
3.3.4 Signal Integration	57
3.3.5 Digital replica of a spectroscopy amplifier	58
3.4 Digital timing measurements	62
3.4.1 Interpolation noise	62
3.4.2 ADC parameters influencing timing resolution	69
3.4.3 Digital implementation of ArcCFD timing	75
3.4.4 Coincidence and time-of-flight measurements	77
3.5 Lookup table for on-line signal fitting	81
3.6 Software for off-line analysis	82
4 Experimental tests with various detectors	85
4.1 Identification using ΔE -E Si-CsI	86
4.2 Pulse shape using CsI(Tl)	88
4.3 Pulse shape in silicon	90
4.4 Time of flight using silicon	95
4.5 Energy measurement using germanium	97
4.6 Timing using germanium	99
4.7 Pulse shape in single-chip telescope	101
4.8 Position using gas PSPPACs	103
4.9 Timing using fast plastic scintillators	106
4.10 Timing using NaI(Tl)	109
4.11 Pulse shape in phoswich detectors	110
5 Simulation of silicon current signals	115
5.1 Pulse shape in silicon detectors for HI experiments	115
5.2 Semiconductors as solid-state detectors	119
5.3 Key factors affecting silicon pulse shapes	121
5.4 Formulation in the continuum	124
5.5 Quasi-microscopic simulation	125
5.6 Preliminary results	130
5.7 Conclusions and future developments	136
6 Conclusions	139
Index	I
Bibliography	V

Acknowledgments

I would like to thank all the people that have contributed with suggestions and useful discussions to this work. In particular, I would like to thank Prof. Giacomo Poggi for his guidance and support during the Thesis and for the enthusiastic participation to this work.

I am also grateful to Prof. Maurizio Bini and Gabriele Pasquali for discussions and productive collaboration.

Discussions about detectors physics with Prof. Nello Taccetti and Luca Carraresi are also gratefully acknowledged.

I am very thankful to all the people of the Nuclear Physics group of Florence for help and collaboration. I would like also to thank Roberto Ciaranfi and Marco Montecchi for their technical assistance.

My special thanks to my family, which supported me during my studies, and to Chiara for the priceless time spent together.

Introduction

The birth of Nuclear Physics can be traced back to the works of Becquerel and of Rutherford, who discovered radioactivity (Becquerel, 1896) and proposed a theory where the atom has a massive charged core, the nucleus (Rutherford, 1911). Few years later the Quantum Mechanics was developed (Schrödinger, 1926) and the first machines able to accelerate nuclei were built (Cockcroft and Walton 1930, Van de Graff 1931).

These and other experimental and theoretical findings made it possible to begin a systematic study of the nucleus that is still under way. Our current knowledge of nuclei covers many aspects of nuclear behaviour (radioactivity, energy spectra, nuclear reactions, stellar nucleosynthesis, ...) and it has found also several practical applications in everyday life. Nevertheless, the difficulty of having a unique theory able to explain completely the behaviour of nuclear matter still challenges both theoretical and experimental physicists. From an experimental point of view the goal is to perform high "quality" measurements (high resolution and granularity, low thresholds, ...) that can be used to verify and improve the existing theories.

Experimental systems are based upon arrays of various detector types able to measure the characteristics of the incoming particles (for example energy, charge, ...). For decades the electrical output of a particle detector has been analyzed using (rather sophisticated) analog methods, and using digital electronics only for final data conversion, acquisition and storage.

In the everyday world people is fully accustomed to a digital manipulation of various kind of information: few examples are mobile communications, digital entertainment systems, media broadcasting and data measurement and storage. In these applications some "analog" information (i.e. audio, video, ...) is converted very soon into a digital data stream and subsequently processed and/or transmitted (and possibly converted back to "analog").

In the last few years these technologies have reached such a development status to make them attractive for the nuclear physics field. The electrical output of a particle detector can be digitized and the

corresponding data properly processed to extract all the information needed. If successful this approach would allow a major renovation in the organization of large experiments, due to the important electronic simplification and to the greater flexibility of these methods with respect to the standard analog methods.

Moreover, because of the wide spread of these technologies in the consumer market, many industrial companies are actively developing various components related to digital information manipulation, thus lowering the general cost of these systems.

In this Ph.D. Thesis an extensive study (both theoretical and experimental) of the applicability of digital sampling techniques has been carried out, focusing mainly on detectors that are used for charged particle detection systems. Nevertheless many of the results are of general interest and can be applied or extended also to other systems.

In the first chapter a very brief overview of Heavy-Ions Nuclear Physics is presented together with a discussion of the commonly used experimental methods. In the second chapter a general description of digital sampling systems is reported, focusing on the relevant topics for nuclear signal analyses. In Chap. 3 a description of the hardware and the software that has been proposed, developed and tested in this Thesis is reported, whereas in Chap. 4 the experimentally obtained results are discussed. Some of the reported results and of the performances can be better understood knowing the physics underlying the detector under test: in Chap. 5 a specific case (silicon detector) is deeply investigated.

This Ph.D. Thesis work has thus been focused on the following points:

- Further development of the digital electronics described in [1].
- Characterization of ADC properties for nuclear physics measurements.
- Detailed study and development of algorithms for high resolution energy and timing measurements.
- Experimental tests with various detectors.
- Simulation of current signals in a silicon detector.

Part of this work has been published in several papers [2, 3, 4, 5], and presented at various international conferences [4, 6, 7, 8, 9].

Chapter 1

An overview of detection systems for Heavy-Ion Nuclear-Physics experiments

As in many other fields, in Nuclear Physics the development of new detection methods or the improvements of the existing ones is strictly related to the precise measurement of certain observables that are relevant for the currently open topics.

In this chapter a brief introduction regarding few of the main open topics in Nuclear Physics is given, focusing on the experimental features requested to future experiments in order to improve significantly the existing knowledge in these areas. The commonly used detector types in Nuclear Physics are then described, and some details are given on the detection processes that are often the limiting factor for the achievable performances. The standard analog-electronics methods used to process the output signals of these detectors are also briefly discussed. In the last section a brief overview of the detector/electronic improvements that would be needed in order to meet the theoretical needs is presented. Some of the motivations that lead to the development of a new experimental method based on fast signal processing (that is the main topic of this Thesis) are also discussed.

Here and in the following, the expression “Heavy-Ion Nuclear Physics” will be used to describe Nuclear Physics studies where the properties of heavy nuclei or of their decay products are of interest, with beam energies generally lower or of the order of ~ 100 AMeV.

1.1 Nuclear Physics in the next decade

In the last 50 years a number of accelerators for the study of nuclear

properties has been realized and used all over the world, frequently employing an electromagnetic acceleration. The desired energy is usually reached with two or more consecutive accelerating stages, each of them tailored to the energy range to be covered by the specific stage. Up to now these methods have been restricted to accelerate stable nuclei only, so that a limited region of the nuclear chart has been explored, namely nuclei lying close to the stability valley in the Z versus N plane.

The study of Heavy-Ion Nuclear Physics based on accelerators can be roughly divided into two areas, namely Nuclear Structure and Nuclear Reactions.

In Nuclear Structure a study of the properties of nuclei at low excitation energy is performed, i.e. the nucleus is treated as a bounded quantum system where energy levels can be, for example, studied by means of the gamma excitation processes. A proper description of nuclei must include quantities like the mass (or the binding energy), the lifetime (if not stable), and quantum numbers like spin, orbital angular momentum, . . . , of both the ground state and excited levels. The need of populating states with high values of angular momentum in the final nucleus often requires the use of Heavy-Ion beams.

In Heavy-Ion Nuclear Reactions with $E \gtrsim 15$ AMeV, the dynamical/thermodynamical properties of the nuclear matter are studied. Typically the use of colliding heavy nuclei permits to create excited nuclear matter, which is usually treated as a fluid described by an Equation of State (EoS).

Both in structure and reaction studies the various nuclei and nuclear matter properties are expected to depend upon the N/Z ratio of the involved nuclei (that is related to the isospin degree of freedom). This prediction has been indeed experimentally observed since decades, although, due to the limited region of the nuclear chart available to experiments, a deeper investigation of these properties is still needed.

The study of nuclear properties is relevant also for astrophysical motivations, for example to understand the nucleosynthesis of various light and heavy elements that are found in nature. These processes involve nuclei that play an important role in the stellar environment, but that are unstable in ordinary conditions, thus making it difficult (often impossible) the experimental study of their properties using the today available stable beams. The study of excited nuclear matter as a function of the N/Z ratio would also allow a deeper understanding of cosmic entities like neutron stars.

These and other motivations have led to the development of new generation accelerators where the production of radioactive (i.e. un-

stable) nuclear beams is possible, using a secondary production from a primary stable beam. This comes at the price of a generally low radioactive-beam intensity, mainly due to the two-step mechanism used (production of a stable beam and “conversion” to the radioactive one). These machines (that are being proposed in these years, see for instance [10]) will allow the investigation of nuclear matter far from the stability region, thus considerably extending our knowledge of nuclear matter.

Several open topics in Heavy-Ion Nuclear Physics will benefit from such machines. As an example in the next sections two physics cases are briefly discussed, one referring to reactions and the second one to structure studies.

1.1.1 Isospin effects on nuclear dynamics and thermodynamics

In a thermodynamical approach, nuclear matter can be regarded as a finite size thermodynamic system. This assumption is particularly useful for the study of heavy-nuclei interactions. Like any thermodynamical system, nuclear matter is thus described by an Equation of State (EoS), which notably exhibits an important dependence on the isotopic composition of the nuclear system. As in infinite systems, a phase transition between a liquid-like and a gas-like state in excited nuclear matter is thus predicted, with some “uncommon” features related to its finite size (for example a region of negative heat capacity). If the hypothesis of existence of a thermally equilibrated nuclear system during the interaction is accepted (this point is still debated in the literature), useful thermodynamical information can be retrieved by relating the excitation of the colliding nuclei to their “temperature”. The estimation of the temperature can be performed by following the de-excitation of the system, in particular from the *isotopic* composition of the particles that are emitted from the hot system (mainly light charged particles, LCPs, and intermediate mass fragments, IMFs).

The study of nuclear collisions can be also carried out from a somewhat complementary point of view, i.e. in the framework of a dynamical description of nuclear matter. In this approach the energy-transfer mechanism from the initial relative velocity to the various internal degrees of freedom is studied and the dynamical (non-equilibrium) processes leading to the final state (possibly thermodynamically equilibrated) are of interest. Experimental signatures of such processes can be found in the presence of nuclear matter “drops”, i.e. emitted

LCPs or IMFs with a kinetic-energy distribution compatible neither with statistical thermal emission nor with direct reactions. Recent experiments [11, 12] have for example shown that, for peripheral collisions, an important dynamical de-excitation mechanism is associated to the “neck” emission. In the early times of the interaction, when the two nuclei re-separate, an elongated region of nuclear matter is created in-between (the neck), which nucleons are exchanged through. The driving forces controlling the diffusion processes in the neck are mainly related to differences between the “macroscopic” properties of the two nuclei, like for instance the isospin composition. The neck disappears either by absorption from the two nuclei or by emission of light charged particles. The isotopic composition and energy distribution of the dynamically emitted particles is expected to depend on the detailed emission mechanism.

The availability of Radioactive Nuclear Beams and the development of next generation detectors will allow the study of dynamical and statistical decays of hot nuclei in a wide range of N/Z ratios (i.e. different isospin compositions) for both central and peripheral collisions. Many theoretical models exist that are able to reproduce (with varying degrees of success) the presently available experimental data, but give very different predictions when extrapolated to higher energies or different N/Z ratios. The availability of beams with higher energy and with isotopic compositions far from the stability line will restrict the number of acceptable models and thus will enhance our knowledge of the underlying physical processes.

These studies typically require high granularity and very large solid-angle coverage of the detection system in order to measure high-multiplicity events and the emission direction of the various particles correctly. The determination of the isotopic composition of emitted LCPs and IMFs is also mandatory.

1.1.2 Nuclear Structure

Since the birth of Nuclear Physics the systematic study of half-lives, branching ratios, angular distributions, electromagnetic moments, . . . , of both ground state and excited levels of nuclei has been a very active research field, allowing stringent tests of the available nuclear models.

Up to now the use of stable beams (and targets) limits in practice the production of excited nuclei belonging to $Z - N$ regions close to the stability line or having a slight neutron deficiency (fusion reactions of medium weight nuclei).

The availability of Radioactive Nuclear Beams and of next generation detectors will allow the exploration of a much wider part of

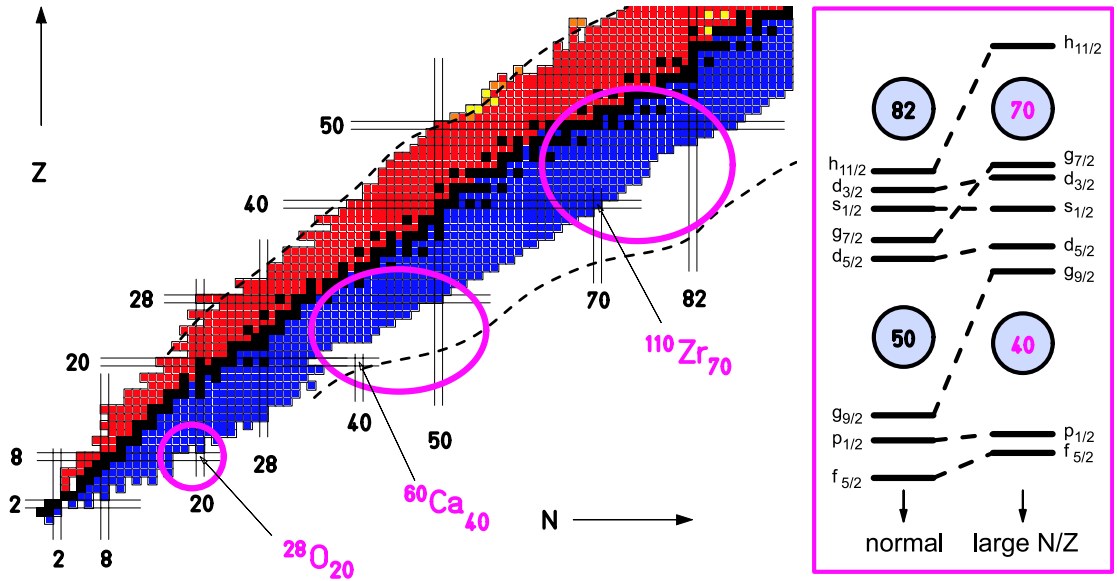


Figure 1.1: Nuclear chart in the light- and medium-mass region. The circles indicate areas with possibly new magic numbers. The right-hand side shows the single particle energies for nuclei close to stability and for nuclei with a large N/Z ratio. Figure from [10].

the nuclear chart, thus making it possible a systematic study of the properties of nuclei with respect to the N/Z ratio, improving considerably the available data for comparison with nuclear structure and astrophysical models.

To give an idea of the physics opportunities that will be available, an example regarding a shell model effect is reported in Fig. 1.1. The surface of very neutron-rich nuclei is expected to be essentially composed of neutron matter only, thus changing significantly the surface properties of the nuclei with respect to the ones close to the stability line. This in turn changes the behaviour of the spin-orbit surface term, which is the leading factor in the determination of the magic numbers of shell models, thus making it possible a significant deviation from the standard magic numbers.

These studies will typically require high-resolution measurements of the γ rays emitted in the de-excitation of the nuclear levels as well as a complete solid-angle coverage in order to increase the available coincidence detection efficiency.

1.2 Experimental methods

In this section a brief overview of the experimental methods that are commonly used in Nuclear-Physics experiments will be given. The discussion will be limited to the main properties of detectors and analog systems that are relevant for the purposes of this Thesis. After a description of the principal interaction properties of radiation, a brief description of the commonly used detectors is given, as well as of the standard analog electronics used to process their signals. Experimental examples (obtained using the digital-signal-processing methods of Chap. 3) of application of these or similar techniques are presented in Chap. 4. More details can be found in various textbooks as for example [13, 14].

1.2.1 Radiation interaction with matter

The principle of operation of all the nowadays commonly used radiation detectors is based on the conversion of the energy deposited by the impinging radiation in the active volume of the detector into some electronic signal. This signal can then be properly analyzed to extract the desired information.

The detailed understanding of the interaction processes between the radiation and the detector material is thus the basis for the design and the use of radiation detectors. The principal radiation types are charged particles, γ rays and neutrons. This Thesis work focuses mainly on heavy charged particles and γ ray detectors. No neutron detector has been studied.

Charged particles

The interaction with a medium causes an energy loss of the impinging charged particle which is slowed down from its original energy E and possibly stopped inside the material. The principal mechanism leading to energy loss is the Coulomb interaction between the particle and the negative charged cloud of the orbital electrons of the absorber atoms. Other mechanisms like electromagnetic or strong interactions with the nuclei are present, although less significant for the purpose of particle detection (but they may be important in particular experimental conditions and definitely in High-Energy Physics).

The energy transferred from the particle to the absorber can be so low to excite atoms and/or molecules (excitation processes) or high enough to produce ionization. The energy deposited in the detector

can thus be found or as atomic/molecular excited states, which subsequently de-excite with the emission of low-energy photons (mainly in the visible range), or as an electron-ion pair (electron-hole in semiconductors) resulting from the ionization processes. Other non-radiative de-excitation processes do exist but they will be neglected in the present discussion.

The specific energy loss dE/dx of a heavy charged particle (with mass $m \gg m_e$, where m_e is the electron mass) is approximately described by the Bethe-Bloch formula [13, 14]:

$$-\frac{1}{\rho} \frac{dE}{dx} \propto \frac{z^2 Z}{\beta^2 A} \left[\log \frac{2m_e \beta^2 c^2}{I(1 - \beta^2)} - \beta^2 \right] \quad (1.1)$$

where z is the charge of the particle, $v = \beta c$ its speed, ρ , Z , A , I are the density, charge, mass and empirical ionization constant of a mono-elemental absorber, respectively. This formula describes the energy loss of heavy charged particles at non-relativistic energies ($\beta^2 \ll 1$) and for energies greater than the shell energies of the absorber. For more details see [13, 14]. As expressed in Eq. 1.1, the energy loss exhibits a strong dependence on the charge and the velocity of the particle, with a moderate dependence on its mass.

Examples of specific energy loss for various particles along their track in a silicon absorber are shown in Fig. 1.2. It is possible to note that the energy deposit along the particle track exhibits a sharp maximum, the Bragg peak. There also exists a well defined distance R (the range of the charged particle) that represents the minimum detector thickness needed to absorb the incoming particles. The range depends on particle type and energy: for example, see Fig. 1.2, the range in silicon for 3 MeV protons is about 90 μm , whereas for a 40 MeV ^{12}C (having almost the same β) is about 45 μm .

When the detector thickness is greater than the particle range the particle deposits its full energy and it consequently stops within the detector. In the opposite case the particle deposits only a fraction of its energy in the detector and emerges with a non-zero residual energy. The deposited fraction of the full energy thus depends on particle type and energy; the correlation between the deposited and the residual energy is the basis of the ΔE - E particle identification method discussed in §4.1.

These considerations are valid when the mass of the incoming particle is much greater than the electron mass, as for example with nuclei. The energy loss of electrons in matter deserves its own discussion, see [14].

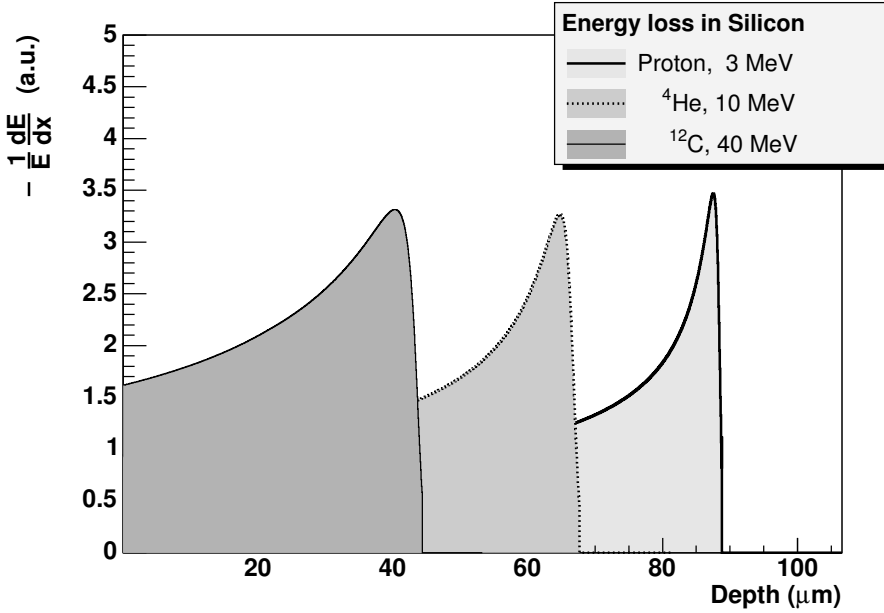


Figure 1.2: Specific energy loss normalized to particle energy (arbitrary units) along the particle track in silicon. Note the strong dependence on particle charge and energy.

γ interactions

There are three main interaction mechanisms that are relevant for the purposes of γ rays detection: photoelectric absorption, Compton scattering, and pair production [13, 14]. In all these processes an absorber electron receives part or all of the γ ray energy and it is the particle actually detected.

In the photoelectric absorption process the photon is completely absorbed in the interaction with a detector atom and this causes the ejection of a high-energetic electron from the atom (photoelectron). The full incident energy of the γ is thus released in the detector.

In Compton scattering an incoming photon with energy E_γ undergoes a scattering with an electron. If θ is the scattering angle, the photon energy E'_γ after the scattering is given by

$$E'_\gamma = \frac{E_\gamma}{1 + \frac{E_\gamma}{m_e c^2} (1 - \cos \theta)} \quad (1.2)$$

where m_e is the electron mass. The deposited energy in the detector is thus $E_{\text{det}} = E_\gamma - E'_\gamma$. The cross section of this process is described

by the Klein-Nishina formula [14]. It is possible to recognize that only a fraction of the total γ energy is released in the detector. In the case of the scattered photon escaping from the detector this causes the formation of a “Compton continuum” in the experimental spectra.

For γ energies E_γ greater than $2m_ec^2$ the pair production is an energetically possible process, although this effect is important only for $E_\gamma \gtrsim 5\text{--}10$ MeV. The full γ energy is released in the detector as kinetic energy of the electron-positron pair and their subsequent annihilation (although one or both of the emitted γ -rays can escape the detector, causing a continuum and single or double “escape peaks”).

These three processes are not exclusive, although their relative importance varies greatly with the γ energy and the charge Z of the absorber (see [14]). Often a γ ray undergoes several interactions before escaping or being completely absorbed in the detector (for example a Compton scattering followed by a photoelectric absorption).

In Fig. 4.11 a typical γ spectrum obtained using a high-resolution detector is shown. Photoelectric peaks as well as the Compton continuum are clearly visible in the figure.

Neutrons

Due to the fact that neutrons carry no electrical charge, they cannot interact with electromagnetic forces, and thus the detection methods used are quite different with respect to the ones previously discussed.

Neutron detection is usually performed by means of indirect methods that exploit strong interactions, i.e. an experimental arrangement is made in order to have a transfer of the neutron kinetic energy to charged particles or to induce a neutron capture followed by γ ray emission.

The conversion techniques are quite different depending on the neutron energy E_n , whether slow neutrons ($E_n \lesssim 0.5$ eV, for example thermal energies) or fast neutrons ($E_n \gtrsim 10$ keV) are used. For more details see [14].

1.2.2 Scintillation detectors

The principle of operation of scintillation detectors is based on the collection of the photons emitted by the material following the detection of a charged particle. The mechanisms leading to the emission of photons after the initial energy deposit vary depending on the scintillator type (for example whether organic or inorganic), but all share the characteristic of producing one or more photons in the visible or

near-visible range. The final number of visible photons is proportional to the energy loss of the detected particle in the material.

Many scintillator materials exist differing for scintillation efficiency, light emission wavelength, time constant of the de-excitation processes, ease of manufacturing, and density (hence stopping power, see Eq. 1.1). For a general review see [14]. Common material choices in Nuclear Physics are NaI(Tl), CsI(Tl) (good efficiency and energy resolution but with relatively long decay times, of the order of few μs) and fast plastic scintillators (low efficiency and poor energy resolutions but with fast decay times, of the order of few ns). Some of the properties of these detectors are briefly discussed in §4.2, §4.9, §4.10.

The light output of a scintillation detector is usually characterized by an exponential decay, due the de-excitation of the scintillator material. Depending on the details of the excitation and de-excitation processes, more than one decay time constant may be present in the output signal.

In order to obtain an electric signal output the scintillation photons coming from the detector must be collected and converted. A common conversion device is the photomultiplier, and the collection is usually enhanced using properly shaped detectors and/or light guides (taking advantage of reflection and diffusion of photons at interfaces).

The structure of a typical photomultiplier is shown in Fig. 1.3. The photons produced by the scintillation process hit the photocathode. The purpose of the photocathode is the conversion of as many of the incident photons as possible into low-energy electrons. This process can be thought as a two step process: first the photon is absorbed by the photocathode, thus transferring its energy to a free electron of the material. Then the electron migrates and, if it reaches the surface of the photocathode, it may escape from the material. The combined efficiency of these processes is quite low and thus for a given number of incident photons only few photoelectrons are produced. Taking into account the various efficiencies, it is possible to estimate that the generation of a photoelectron requires – on average – an incident energy of about 100–500 eV, depending on the used scintillator. This means that the Poissonian fluctuations in the photoelectron number are often the main factor limiting the achievable energy resolution of the detector-phototube system.

The current pulse due to photoelectrons would be very small and thus unfeasible for direct measurement. This problem is solved by the electron multiplier structure of Fig. 1.3. The photoelectrons are accelerated by the imposed electric field in the volume between the photocathode and the first dynode. When they strike the first dynode the acquired energy is high enough to produce a secondary electron

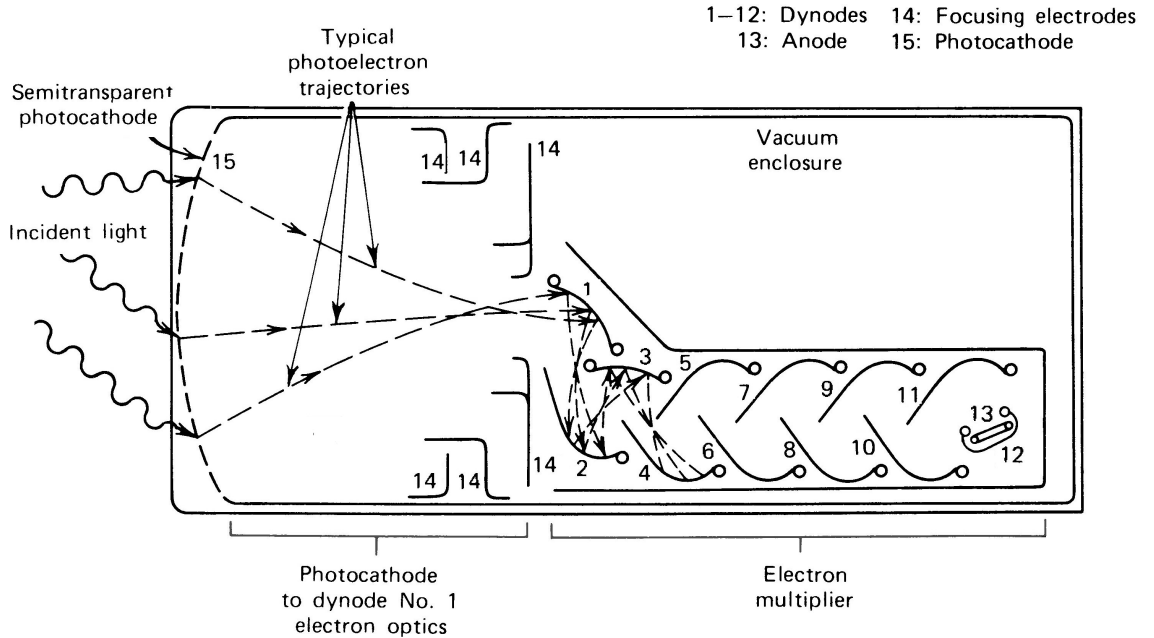


Figure 1.3: Typical photomultiplier structure (adapted from [14]). The photons hit the photocathode causing the emission of a small number of photoelectrons that is subsequently amplified by the dinodes.

emission from the dinode. Typically 3–5 secondary electrons are produced for each primary photoelectron. The secondary electrons are then accelerated towards the next dinode where a further multiplication occurs. This process is repeated several times (12 in Fig. 1.3) until a measurable signal is obtained and output to the anode. This electrode arrangement allows an almost noise-free amplification of the original signal, still retaining the time structure of the original photon burst (if the transit time spread of the photomultiplier can be neglected).

Other devices like photodiodes can be used in place of a photomultiplier for the scintillation photons detection. Their principle of operation is the same of solid-state detectors, that are described in §1.2.4. These devices does not usually provide an amplification of the current (with the exception of avalanche photodiodes) and are characterized by inferior noise properties with respect to phototubes. On the other hand, their very compact size, easy handling and substantial immunity from magnetic fields make photodiodes attractive for the readout of scintillation detectors in some applications.

Scintillation detectors are commonly used for the detection of energetic light particles and for covering large areas (or angular regions)

with a moderate cost. Fast scintillators are used in those applications where the definition of the arrival time of the particle is of paramount importance, at the expense of a much lower energy resolution.

1.2.3 Gas detectors

In gas detectors the energy loss mechanism leading to the formation of ion-electron pairs (§1.2.1) is exploited. The active volume of the detector is filled with a particular gas mixture at low pressure, which is the medium where incoming charged particles deposit part of their energy creating ion-electron pairs. The number of created pairs is proportional to the energy deposited by the incoming particle, and, on the average, about 20–40 eV are required for the production of a pair (this value depends on the used gas mixture and on the particle type).

An electric field is applied over the gas volume, in order to separate ions and electrons and avoid recombination. With such an arrangement, ions and electrons start drifting inside the detector volume in opposite directions, thus inducing a current on the collecting electrodes. The ion drift velocity is several orders of magnitude smaller than the electron one, and in many applications only the faster signal coming from the electron drift is used for measurement.

Depending on the applied voltage and pressure the drift velocity of electrons may become high enough to generate a secondary ionization in the gas. This effect is called “gas multiplication” and it is often used to obtain a higher-level signal as output of the gas detector.

There exist many gas-detector configurations which cover the various needs met in both Nuclear and Particle Physics. In §4.8 the case of Position Sensitive Parallel Plate Avalanche Counter detectors (PSPPACs) is presented. This detector type, used for example in the FIASCO experiment [15], is characterized by low detection thresholds, good timing properties, position sensitivity and poor energy resolution.

From the practical point of view the handling of a gas filled detector within an experiment that operates under vacuum needs particular care.

1.2.4 Solid-state detectors

The principle of operation of solid-state detectors closely resembles the one discussed for gas detectors.

The incoming particle deposits part of its energy into the detector material, which is a high-purity semiconductor junction (usually sili-

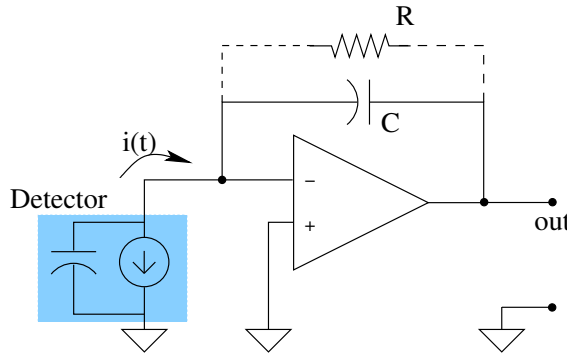


Figure 1.4: Simplified schematic of a charge preamplifier. The current pulse coming from the detector is integrated on the capacity C . The resistor R is used to bring back the output to zero over long times with a time constant equal to RC .

con or germanium); the ionization produces a number of electron-hole pairs proportional to deposited particle energy. About 3.6 eV are required for each electron-hole pair, thus making the contribution to the energy resolution due to fluctuations in the number of carriers much smaller than the previously discussed detector types, taking also into account that the effective fluctuations are reduced with respect to the pure Poissonian case by the Fano factor.

A bias voltage is applied to the semiconductor junction in order to separate electrons and holes and avoid recombination. Drift velocities of holes and electrons are of the same order of magnitude, and thus both charges give an important contribution to the overall current pulse while drifting towards the collecting electrodes.

The current output from the detector is usually processed with a charge-sensitive preamplifier as the one depicted in Fig. 1.4. The preamplifier integrates the current $i(t)$ over the capacitor C , whereas the resistor R is used to bring back to zero the output of the integrator with a decay time $\tau_{\text{pre}} = RC$ (much longer than the current signal duration). For times $t \ll \tau_{\text{pre}}$ the resulting signal is thus very similar to a step but for a non-zero risetime, given the finite duration of the current signal.

Due to the high intrinsic resolution of these detectors, the preamplifier noise often gives a non negligible contribution to the attainable final resolution, especially in those cases where the measurement of low-energy particles or γ rays is of interest. Taking into account the various noise sources of the schematic in Fig. 1.4, the dark current noise of the detector and the bias resistor noise (see [16]), the spectral

noise density [17] of the preamplifier can be approximately described by the following expression:

$$w(\omega) = a \cdot \frac{\tau_{\text{pre}}^2}{1 + \tau_{\text{pre}}^2 \omega^2} + b \simeq \frac{a}{\omega^2} + b \quad (1.3)$$

where a and b are constants that depend on the detector-preamplifier system (the last approximation derives from considering the practical case of very large τ_{pre}). The b term increases with the detector capacitance, thus causing a higher white-noise contribution for high capacitance detectors.

Typical values found in high-resolution germanium-based systems are $\tau_{\text{pre}} = 0.1 - 1$ ms, with a final contribution from the preamplifier noise to the achievable resolution of the order of 0.5–1 keV. A deeper discussion of the noise properties of these systems is given in §1.2.7 and §3.3.

These detectors are usually employed where a high-resolution energy measurement is needed, with the added bonus of good quality timing properties. Germanium detectors can be fabricated with relatively large active volumes (about 300 cm³) and are used for high-resolution γ -ray spectroscopy applications. Silicon-detector sizes are more limited (about 50–100 cm² with 100–500 μm thickness) and they are normally employed for charged-particle detection.

A full discussion of the properties of a particular solid-state detector (silicon) is presented in Chap. 5, where a simulation of its properties starting from the detector physics is presented.

1.2.5 Pulse-shape analyses

As discussed in §1.2.1 the ionization density, proportional to the specific energy loss dE/dx , varies greatly for different particles. In general the presence of a high ionization density produces a reduction of the final signal amplitude (generally indicated as “quenching”) and a distortion of the shape of the current pulse with respect to the low-ionization case. As a consequence, while the total charge of the output pulse is (or should be) proportional to the particle energy regardless of its type, these (and other) factors lead to a dependence of the *pulse shape* on the particle type.

A typical example is the response of the CsI(Tl) scintillator. Its current output can be schematized as the sum of two exponentially decaying pulses with different decay times. The relative weight of these two exponentials is related to the initial specific ionization density, and this finally gives a dependence on the particle charge and mass.

The pulse-shape dependence on the particle type can be effectively

used as an experimental tool for determining, with a single detector, not only the particle energy but also its type.

Commonly used detectors with notable pulse shape properties are scintillation detectors (mainly CsI), that have been used since several years in large Nuclear-Physics experiments. Recently, interest has grown in the application of pulse shape analyses (PSA) to silicon detectors for identification of the detected charged particles: examples of these applications are discussed in §4.3 and Chap. 5.

A different application of pulse shape analysis can be found in coaxial germanium detectors, where a dependence of the pulse shape on the γ interaction point is observed (due to the high inhomogeneous electric field inside the detector). International collaborations [18, 19] are actively working in this field with the goal of reconstructing the γ interaction point using segmented large-volume germanium detectors and digital-sampling methods.

1.2.6 Comparison between detector types

Depending on the particular application, the energy and the type of the particles to be detected, and the possible need for good energy and/or timing measurements, a particular detector type can be chosen. Often no single detector is able to satisfy all the experimental requirements and then two or more different types are used, trying to match their characteristics and to cover the needed detection range.

The comparison between each detector properties is not trivial, and would deserve a much deeper discussion. However, in order to describe better the range of applicability of each detector, in Tab. 1.1 a very simplified comparison is presented.

It is possible to appreciate that the low energy needed for the creation of an electron-hole pair makes solid-state detectors the option of choice for high-resolution energy measurements. The timing performances of the various detector types are similar (although they may vary significantly depending on the particular detector used), except for the case of fast plastic scintillators where the resolution can be as good as 10–30 ps. As a general rule of thumb, the timing properties deteriorate with the increase of the detector size. Silicon detectors can be used to measure charged particles in a very wide charge range, whereas gas detectors have high efficiency only for highly ionizing particles and scintillation detectors are commonly used only in light charged-particle detection applications (besides γ ray detection). Pulse-shape applications are well established in the case of inorganic scintillation detectors, whereas studies are still under way for solid-state devices. Gas detectors are the option of choice in very specific

	Scintillator	Gas	Solid State
Energy/carrier	100–500 eV	20–40 eV	~3 eV
Energy resol. @ 1 MeV	100–500 keV	20–50 keV	1–10 keV
Timing resol. @ 1 MeV	~0.03–1 ns	0.1–1 ns	0.1–2 ns
Detectable particle charge	1–6	>20	all
pulse shape	y	n	y/n
Area limits	100 cm ²	m ²	cm ²
Easy to handle	y	y/n	y
Cost/cm ²	€	€	€€

Table 1.1: Simplified comparison between the different detector types discussed in the text. Only the gross average properties of each detector type when used in a standard configuration have been reported.

applications where a large area/volume coverage is needed. The price for a given angular coverage using solid-state detectors is generally higher than that of scintillation or gas ones.

Whereas the resolution figures reported in Tab. 1.1 refer to ~1 MeV energies, Nuclear-Physics experiments usually operate over wide dynamic ranges, so that other experimental factors (like detector homogeneity, quenching, ...) are usually limiting the finally attainable energy-resolution performances.

A typical Nuclear-Physics experiment will use two or more detector types in order to reach its detection goals. As an example, in the FIASCO experiment [15] a low-threshold detection of low-energy heavy fragments as well as charged-particle identification were needed for nuclear dynamic studies in peripheral and semi-peripheral collisions. A three layer stack of gas, silicon and phoswich detectors (see §4.11) has been used in order to meet these requirements.

1.2.7 Analog electronics: high-resolution energy measurements

For all the discussed detector types, the current output of the system is characterized by an amplitude (or an integral) proportional to the energy deposit of the detected particle. An accurate measure of this quantity thus allows, with proper calibration, the determination of the particle energy.

Solid-state detectors are the most demanding detectors in terms of electronic signal-to-noise-ratio (SNR). The following discussion will

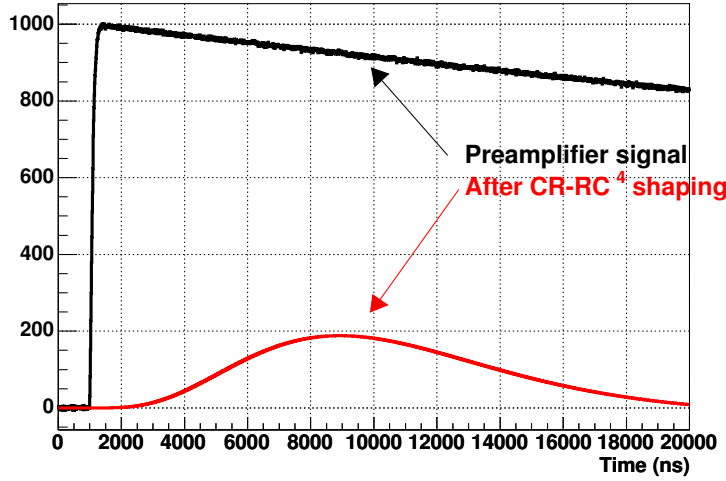


Figure 1.5: Example of shaping of the output of a charge preamplifier used in order to achieve a better signal-to-noise-ratio. A CR-RC⁴ network has been considered in this example.

thus focus on the use of analog electronics to extract the amplitude information on such signals, although many of the presented solutions can be applied to other detectors with small modifications. A careful optimization of the electronic processing chain is usually needed only for solid-state detectors when used for low-energy particle or γ -ray detection, whereas for high-energy particles as well as gas and scintillation detectors the choice of the signal processing methods and parameters is less critical.

As discussed in §1.2.4, silicon and germanium detectors are usually connected to charge-sensitive preamplifiers, whose output spectral noise density (given in Eq. 1.3) is the sum of a white component (b term) and a non-white one (a term) with a $1/\omega^2$ behaviour. A filter is applied to the step-like output coming from the charge preamplifier in order to increase the SNR of the signal. The peak of the filtered signal is measured using Charge-to-Digital Converters (QDCs) or Peak-Sensing converters [14]. An example of signal shaping is presented in Fig. 1.5.

Extensive work about the “optimal” signal-processing electronic chain to be used in this and similar experimental configurations can be found in the literature (see for example [20, 21, 22]). It is found that the best SNR for a signal with these properties is achieved using an “infinite-cusp shaping”, which is a shaping network with an infinite

parameter	CR–RC	CR–RC ⁴
SNR/SNR _{cusp}	0.736	0.858
Step response $G_{\text{step}}(t)$	$\frac{t}{\tau_{\text{sha}}} \exp\left(-\frac{t}{\tau_{\text{sha}}}\right)$	$\frac{1}{24} \frac{t^4}{\tau_{\text{sha}}^4} \exp\left(-\frac{t}{\tau_{\text{sha}}}\right)$
t_{maximum}	τ_{sha}	$4\tau_{\text{sha}}$
α	$\frac{1}{8}$	$\frac{35}{512}$
β	$\frac{1}{8}$	$\frac{5}{512}$
γ	$\frac{1}{e}$	$\frac{32}{3} \exp(-4)$

Table 1.2: Parameters describing the behaviour of a CR–RC and CR–RC⁴ shaping networks. See text for details.

output response (i.e. infinite duration in the time domain) characterized by a sharp cusp. Various practical considerations lead to the use of different shaping networks, whose performances are then usually measured as ratios with the infinite cusp one.

In Tab. 1.2 the SNR of two common configurations is reported: the CR–RC shaping (a differentiation, CR, followed by a low-pass RC) and the CR–RC⁴ (a differentiation, CR, followed by four low-pass RC networks).

In both configurations a single parameter $\tau_{\text{sha}} = RC$ (the shaping time) is used to select the desired frequency band. In Tab. 1.2 the time response of the filter $G_{\text{step}}(t)$ to a step and the time t_{maximum} (the time at which the shaped signal reaches its maximum) obtained with a step signal as input are also reported.

The total output variance of the shaping filter \mathcal{F} (assuming a perfectly noiseless filtering network) can be computed from the filter transfer function $H_{\mathcal{F}}(\omega)$ and from the input spectral noise density $w(\omega)$ (see Eq. 1.3) as:

$$\sigma_{\text{sha}}^2 = \frac{1}{2\pi} \int_0^\infty w(\omega) |H_{\mathcal{F}}(\omega)|^2 d\omega \quad (1.4)$$

The following expression (normalized to signal output) is obtained:

$$\sigma_{\text{sha}}^2 = \frac{1}{\gamma^2} \left(\alpha a \tau_{\text{sha}} + \frac{\beta b}{\tau_{\text{sha}}} \right) \quad (1.5)$$

where γ is the shaped signal amplitude for $t = t_{\text{maximum}}$, α and β are numerical constants. The values of α , β and γ for the two considered

filters are reported in Tab. 1.2.

Differentiating Eq. 1.5 with respect to τ_{sha} allows the determination of the optimal choice of τ_{sha} for a given a, b :

$$\tau_{\text{sha}}^{\text{opt}} = \sqrt{\frac{\beta b}{\alpha a}} \quad (1.6)$$

which gives the following equivalent expressions for the optimal resolution:

$$\sigma_{\text{sha, opt}}^2 = \frac{2}{\gamma^2} \alpha a \quad \tau_{\text{sha}}^{\text{opt}} = \frac{2}{\gamma^2} \frac{\beta b}{\tau_{\text{sha}}^{\text{opt}}} = \frac{2}{\gamma^2} \sqrt{\alpha a \beta b} \quad (1.7)$$

Typical values for germanium detectors employed for low-energy γ -ray measurements are $\tau_{\text{sha}}^{\text{opt}} \simeq 2 - 6 \mu\text{s}$, whereas $\sigma_{\text{sha, opt}}$ is usually in the 0.5–1 keV range.

The above discussion is based on the assumption of a fixed-shape step-like input signal. Whereas this approximation is usually valid for real signals when the signal risetime is much smaller than the shaping constant τ_{sha} , the presence of signals with different shapes gives an additional contribution to resolution worsening. Signals with the same amplitude but different shapes are treated in a different way by the shaping filter and thus the final maximum of the shaped signal depends not only on particle energy but also on signal shape. This effect causes a reduced amplitude for slower signals and it is commonly referred to as “ballistic deficit”.

1.2.8 Analog electronics: timing measurements

Timing electronics is usually employed to perform coincidence measurements (for example to measure the time of flight of a particle) or to obtain information about the shape of the signal. Many analog timing techniques exist, for a review see [14].

A commonly used method is the “constant fraction timing” [23] (CFD), schematically shown in Fig. 1.6. Two copies of the original input signal of Fig. 1.6(a) are produced, one inverted and attenuated by a fraction f and the other delayed by a time amount δ ; a final signal is obtained summing the two signals, as shown in Fig. 1.6(d). The desired time mark is generated in correspondence to the zero-crossing of the final signal.

It is easily shown that, if the signals of interest are characterized by a linear rise and have a fixed shape, the obtained time reference is independent of the final amplitude of the original signal, and it is equal, apart from an offset, to the time where the original signal reaches a fraction of its amplitude (hence the name of the method).

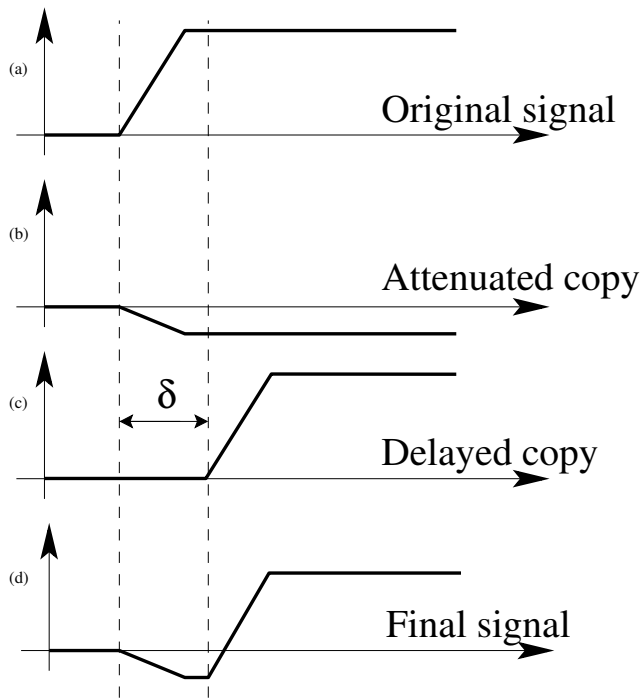


Figure 1.6: Schematic representation of the CFD working principle. One inverted and attenuated and one delayed copy of the original signal are summed to obtain a final signal characterized by a zero-crossing.

The method works properly when the delay δ is greater than the time needed by the signal to reach its asymptotic value (loosely speaking, its risetime).

As a variant of this method, in Amplitude and Risetime Compensated CFD (ArcCFD, [24, 25]) the delay δ is chosen as short as possible taking into account the experimental noise. It is possible to show that this modification allows a time measurement with the same desirable properties of CFD timing plus a compensation for the possibility of different risetimes. This compensation effect is exact for linear signals and only approximate for real signals with a non-linear onset.

1.3 Requirements for future detection systems

In the previous sections a description of the current status of experimental methods to be used in Nuclear Physics have been pre-

sented. It is important to note that, in order to take full advantage of the future radioactive nuclear beam facilities, these methods need to be enhanced or possibly replaced with new techniques. These improvements, if possible, will allow a high-resolution determination of the various measurable quantities that are needed for enhancing our knowledge of nuclear matter, as described in §1.1.

For nuclear dynamics and thermodynamics studies (§1.1.1) the detection over the full solid-angle of charged particles that are emitted during the collision is of paramount importance. A one-unity resolution for charge and mass determination and a precise measurement of the velocity of each particle is needed in order to fully characterize each event, and this in turn requires high granularity, good timing measurements and isotopic identification of the detected particles up to $Z \sim 20$ (more ambitious projects are aiming at isotopic identification up to $Z \sim 30$), for example using composite detectors and pulse shape analysis methods. Where isotopic identification is not any more possible, charge identification up to about $Z \sim 80 - 100$ is aimed at. The energy range of interest for particles to be detected in these applications is about 100 keV–1 GeV, with an energy resolution that is usually dominated by the detector properties, so that an extreme optimization of the relevant electronics is often not needed. The needed precise measurement of time of flight of the particles requires a timing resolution of the order of 100–400 ps.

For nuclear spectroscopy studies (§1.1.2) high granularity is needed for the requested angular-correlation accuracy and for high-resolution energy measurements, where an important effect due to Doppler shift of the γ emitted by the moving source is expected. The use of ancillary detectors for the detection of light charged particles ($Z \lesssim 4$) is also envisaged. The γ -ray energies involved in these applications are of the order of 10 keV–10 MeV, with a needed electronic energy resolution of about 1 keV. Electronic timing with a resolution of the order of few nanoseconds should be adequate for the purposes of these experiments.

As already discussed, a requirement that is common to many applications is the need of high granularity, that in turn translates into the necessity of using a very high number of electronic channels. This means that the size, power dissipation, and cost of each channel must be low enough to allow a practical implementation of the system. Modularity and flexibility are also important issues in systems where the final number of acquisition channels is of the order of 10^4 or more. Another common requirement is a high efficiency for the experimental apparatus. A full 4π solid angle coverage is needed in order to have full event-by-event reconstruction.

In this Thesis a detailed study of digital sampling techniques has been performed, for both high-resolution energy and timing measurements. As it will be discussed in the following chapters, these methods are expected to be able to satisfy most (if not all) of the requirements for future detection systems. Studies about using sampling systems in spectroscopy measurements for Doppler shift corrections (using segmented germanium detectors) are in progress [18, 19]. In this Thesis the discussion focuses mainly on particle detection methods, using different detector types in order to study (from a theoretical and experimental point of view) the performances of sampling systems and their applicability in the next generation experiments.

Chapter 2

Sampling systems

In this chapter a brief description of digital sampling systems is presented: after an introduction the main properties of ADCs and DACs devices are discussed. In §2.4 the basics of the Discrete Time Signal Processing theory will be reported. In §2.5 a particular hardware device type widely used in these kinds of applications will be introduced.

2.1 Introduction

An example of a general system based on digital sampling is shown in Fig. 2.1. An analog input signal is shown on the left as a function of time. It is converted into a digital data stream by an Analog to Digital converter (ADC). After the desired digital processing has been performed on the data, the digital data stream is converted back to an analog signal via a Digital to Analog converter (DAC). Some (common) optional characteristics may include data transmission or reception to/from other devices and recording the digital data on some storage device.

As it will be discussed in the following sections, if the AD and DA conversions do not introduce “excessive” noise in the sampling process, a system like the one depicted in Fig. 2.1 is able to apply any desired algorithm to the input signal and produce the relative output.

Starting from this very general scheme, many different implementations may exist depending on the specific application. In the general case it is possible to identify three basic building blocks: the ADC, the DAC and the digital signal processing section, although in many applications not all of them are needed.

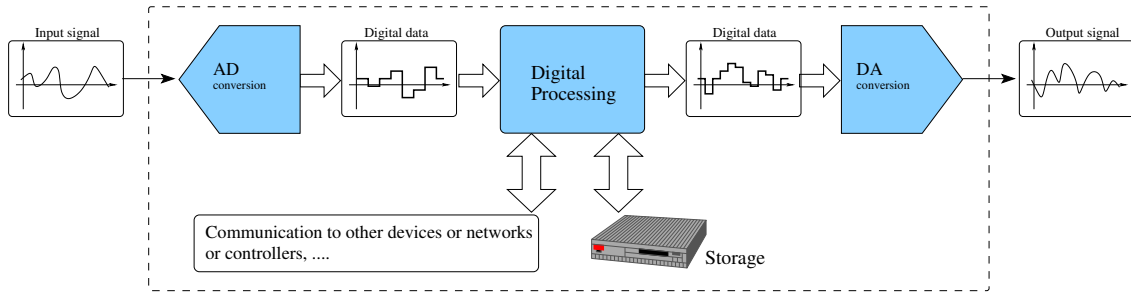


Figure 2.1: Simplified view of a signal-processing system based on digital signal conversion and processing.

2.2 Analog to digital conversion

Generally speaking every system that provides a numerical output proportional to the amplitude of some analog input signal can be regarded as an analog to digital conversion system (ADC). The conversion procedure is usually triggered by some logic signal that fixes the time t at which the conversion occurs. A very common configuration is realized using a periodic logic signal (clock) with a fixed frequency f_s (sampling frequency) to trigger the conversions. In this way the time slice between two successive conversions (or samples) is fixed and equal to $\tau_{\text{clk}} = 1/f_s$ (sampling period). Whereas the amplitude of the analog input signal can assume any value, the digital output from the ADC can assume only a finite number of values (that is usually a power of 2). The converter can thus only approximate the continuous input value with its discrete (digital) output. For example the output of a 12 bit converter can only assume integer values ranging from 0 to $2^{12} - 1 = 4095$. This fixes also the minimum change in the input that can be measured (in our example 1/4096 of the full ADC input range). The smallest digital unit is usually referred to as least significant bit (LSB).

There are characteristics of an *ideal* ADC that are not met in the case of *real* ADCs. A quantitative description of the performances of an ADC is usually given by the manufacturer using the following quantities:

Effective number of bits

In the case of a noiseless constant input signal an ideal AD converter should produce a constant conversion code. This is not the case of real ADCs, that output a digital data stream of different samples fluctuating around the nominal value. The amount of this fluctuation can be quantified with the “effective number of

bits" (ENOB, in general a non-integer quantity). Typical values for high-speed ADCs are 1–2 bits below the "physical" number of bits (for example a 12 bit converter can have 10–11 effective bits). An equivalent quantity to state the effective number of bits is the SNR, usually given in decibels. The following holds:

$$\text{SNR(dB)} = 6.02 \cdot \text{ENOB} + 1.76 \text{ dB} \quad (2.1)$$

A full discussion (together with some useful conversion formulas) is given in [26].

For many applications this effect can be schematized as an additional white-noise source fed into the input of an otherwise perfect ADC. See §2.4.3, §3.3 and §3.4 for a deeper discussion.

Integral non-linearity

For an ideal ADC there exists a simple linear relationship between the amplitude of the input signal and the relative output. The integral non-linearity of a converter measures the maximum deviation from this ideal behaviour. A typical absolute value is 0.2–1 LSB.

Differential non-linearity

For an ideal ADC the width of each LSB (i.e. the interval in Volts between two consecutive converted values) is constant and equal to the full range of the converter divided by 2^{bits} . In real ADCs, depending on the internal architecture of the device, it is possible to have some bits larger or narrower than the nominal value. This effect is measured by the differential non-linearity: a typical value is 0.2–0.5 LSB. In the case of an ADC with a differential non-linearity greater than 1 LSB some valid digital codes cannot be produced by the device (because they would overlap with some neighbour wide bit). This undesired effect is referred to as the presence of missing codes. Typically the absence of missing codes is guaranteed.

Only the principal parameters describing the performances of real ADCs have been presented here: for a detailed discussion see [27, 28].

The circuit used to perform the desired analog to digital conversion varies greatly depending on the requested performances: the key parameters are mainly the sampling frequency f_s and the resolution (i.e. the number of bits) of the converter. The principal conversion techniques are (roughly ordered in ascending f_s):

Single- or dual-slope integrating ADCs

Integrating ADCs provide high resolution and good noise rejec-

tion. The integrating architecture provides a straightforward approach to a high-resolution conversion of a low-bandwidth analog signal into its digital representation. These type of converters often include built-in drivers for LCD or LED displays and are found in many portable instrument applications, including digital panel meters and digital multimeters.

$\Sigma - \Delta$ ADCs

The sigma-delta ADC uses oversampling of a low-resolution converter (usually 1 bit) followed by digital filtering to obtain a much higher resolution sampling. These ADCs are used predominately in low-speed applications requiring a trade-off between speed and resolution. Bandwidths are typically less than 1 MHz with a range of 12 to 18 effective bits.

Successive-approximation register

SAR ADCs are frequently the architecture of choice for medium-to high-resolution applications with sample rates under 5 MS/s. SAR ADCs most commonly range in resolution from 8 to 16 bits.

Pipelined flash ADCs

This method combines the speed of the Flash ADCs with a successive approximation method (called also sub-ranging) to achieve a high-resolution/high-speed trade-off. This conversion method is employed in the AD converter used in this Thesis and it is described with some detail in §3.1.

Flash ADCs

This parallel encoder method is the fastest A/D conversion technique. The input signal voltage is fed simultaneously to one input of each comparator (8 bit requires $n = 256$ comparators), the other inputs of which are connected to n equally spaced reference voltages. A priority encoder generates a digital output corresponding to the highest comparator activated by input voltage.

Analog pipelining

This event-based conversion technique uses a capacitor array to perform a fast analog sampling of the signal (up to few GHz) followed by a slower standard AD conversion. This method is used for example in proprietary ADCs that can be found in some digital oscilloscopes.

A full discussion of these conversion methods can be found in [27, 28].

As an example of the available converters in Tab. 2.1 the current (at the time of this writing) production status of a company

Resolution (bits)	Sampling rate f_S					
	< 10 kS/s	10 kS/s to 100 kS/s	100 kS/s to 1 MS/s	1 MS/s to 10 MS/s	10 MS/s to 100 MS/s	> 100 MS/s
> 17	•	•	○			
14–16	•	•	•	•	○	○
12–13		•	•	•	•	•
10–11		•	•	•	•	•
8–9			•	•	•	•
< 8					•	

Table 2.1: Production status of ADCs as a function of the sampling frequency and resolution (at the time of this writing). Widely available configurations are denoted with •, whereas ○ refers to announced but yet unavailable converters or to configurations where only one converter is presently available.

leader in the ADC market is presented. The choice of a particular converter depends strongly on the specific application: for example 44.1 kHz - 16 bit converters are the standard for digital audio applications, whereas 96 kHz - 24 bit converters are used for high-fidelity audio/video systems. Higher frequency ($\gtrsim 1$ MS/s) converters are usually employed in communication systems.

In §3.1 a discussion of the ADC used in this Thesis will be presented.

2.3 Digital to analog conversion

The digital to analog conversion (DAC) process can be simply regarded as the functional counterpart of the analog to digital conversion.

An analog output signal is produced from a digital input data stream, that is often characterized by having a constant time spacing between two consecutive samples, i.e. a fixed sampling frequency f_S .

Most of the description and many of the definitions given in §2.2 for AD converters can be also applied for DA converters *mutatis mutandis*.

In this Thesis no DA converters have been used: for more details on this topic see [27, 28].

2.4 Discrete time signal processing

In this section a brief introduction to the theory underlying Discrete Time Signal Processing (i.e. the linear processing of signals known only at discrete times) is presented. The discussion is limited to the case of signals sampled at a constant sampling frequency f_s , i.e. with a constant time spacing τ_{clk} between samples. This is a very common choice in Digital Signal Processing and it has been used in the experimental measurements of this Thesis.

These topics are extensively discussed in many textbooks, as for example [29, 30].

The following notation will be used:

τ_{clk}	Sampling period ($\tau_{\text{clk}} = 1/f_s$)
f_s	Sampling frequency (with radian frequency $\omega_s = 2\pi f_s$)
f_N	Nyquist frequency
$S(t)$	Continuous signal as a function of time
$S[k]$	Discrete signal as a function of the integer index k
$\mathcal{F}_S(\omega)$	Fourier transform of $S(t)$ into the frequency domain
$\mathcal{Z}_S(z)$	\mathcal{Z} transform of the signal $S[k]$ into the z domain
$(f * g)(t)$	Folding integral (convolution) between two functions of time $f(t)$ and $g(t)$

Although the formalism can be applied independently of the sampling period τ_{clk} (for example using the adimensional time variable $x = t/\tau_{\text{clk}}$ and the adimensional frequency $f' = \tau_{\text{clk}} \cdot f$), in the following the explicit dependence on τ_{clk} will be retained (where useful) in order to better clarify the underlying processing.

2.4.1 The Fourier and the \mathcal{Z} transforms

Given a continuous (complex) function $S(t)$, its Fourier transform (and its inverse) is defined¹ as:

$$\begin{aligned} \mathcal{F}_S(\omega) &= \int_{-\infty}^{+\infty} S(t) \cdot e^{-j\omega t} dt \\ S(t) &= \frac{1}{2\pi} \int_{-\infty}^{+\infty} \mathcal{F}_S(\omega) \cdot e^{+j\omega t} d\omega \end{aligned} \quad (2.2)$$

Thus in the general case $\mathcal{F}_S(\omega)$ is a complex quantity.

A complete discussion of the mathematical properties of the Fourier

¹ Other definitions of the Fourier transform exist differing from Eq. 2.2 only for a multiplying numerical factor. This difference is not relevant for the purposes of the present discussion.

transform is reported for example in [29, 30]. To name a few: (a, b complex quantities, $f(t)$ and $g(t)$ functions of time)

$$\begin{aligned} \text{Linearity: } & \mathcal{F}(af + bg) = a\mathcal{F}_f + b\mathcal{F}_g \\ \text{Convolution: } & \mathcal{F}(f * g) = \mathcal{F}_f \cdot \mathcal{F}_g \\ \text{Parseval's theorem: } & \int |f(t)|^2 dt = \frac{1}{2\pi} \int |\mathcal{F}_f(\omega)|^2 d\omega \end{aligned}$$

If it exists a frequency f_N such that $\mathcal{F}_S(\omega) = 0$ for $|\omega| > 2\pi f_N$, then the input signal $S(t)$ is defined a “bandlimited signal”, and f_N is called the “Nyquist frequency” of that signal [31].

In the case of a discrete signal $S[k]$ the Fourier transform can be defined, in analogy with Eq. 2.2, as (see also Eq. 2.8)

$$\mathcal{F}_S(\omega) = \sum_{k=-\infty}^{+\infty} S[k] \cdot e^{-j\omega k \tau_{\text{clk}}} \quad (2.3)$$

In the case of finite length sequence (i.e. $S[k] \neq 0$ only for $0 \leq k < N$) the summation in Eq. 2.3 is limited to N terms and thus it exists and is finite for every finite input sequence $S[k]$.

A very computational efficient method for performing the Fourier transform exists for the case of discrete values of ω given by $\omega_k = kf_S/N$, $k = 0..N$, the Fast Fourier Transform (FFT, see [32]).

For many applications (like digital filtering, see §2.4.4) it is preferable to use a different linear transform, the \mathcal{Z} transform. Given an input sequence $S[k]$, where k is an integer index, the \mathcal{Z} transform \mathcal{Z}_S of $S[k]$ is defined as:

$$\mathcal{Z}_S(z) = \sum_k S[k] \cdot z^{-k} \quad (2.4)$$

A simple relation between the Fourier transform and the \mathcal{Z} transform can be found writing the complex variable z as $z = re^{j\omega}$ in Eq. 2.4:

$$\mathcal{Z}_S(re^{j\omega}) = \sum_k (S[k]r^{-k}) \cdot e^{-jk\omega} \quad (2.5)$$

It possible to note that the discrete Fourier transform of the sequence $S[k]$ is equal to \mathcal{Z}_S evaluated on the circle $|z| = 1$.

A complete discussion of the \mathcal{Z} transform properties can be found in [29]. Such properties can be briefly summarized:

- The \mathcal{Z} transform of a stable system (that is an infinite length sequence of finite $S[k]$) has no poles (i.e. divergences of \mathcal{Z}_S)

inside the unity circle $|z| < 1$.

- Many of the properties of the Fourier transform have a simple equivalent for the \mathcal{Z} transform.
- Given a sequence $S[k]$, shifting the sequence in time we have:

$$S[k - k_0] \xleftrightarrow{\mathcal{Z}} z^{-k_0} \cdot \mathcal{Z}_S(z) \quad (2.6)$$

where k_0 is a positive integer.

2.4.2 Sampling and aliasing

The process of sampling a continuous input signal at a fixed sampling frequency f_S can be mathematically treated as a two step process [29]:

1. Modulation of the signal $S(t)$ with the periodic signal:

$$C(t) = \sum_k \delta(t - k\tau_{\text{clk}}) \quad (2.7)$$

where $\delta(x)$ is the Dirac delta function. The function $C(t)$ is sometimes referred to as the “sampling comb”.

2. Conversion of the obtained impulse sequence to a discrete sequence.

At step 1. we thus obtain the following:

$$S_{\text{modulated}}(t) = S(t) \cdot \sum_k \delta(t - k\tau_{\text{clk}}) \quad (2.8)$$

The Fourier transform of $S[k]$ is equal to the convolution between $\mathcal{F}_S(\omega)$ and the transform of $C(t)$ that can be proved to be $\mathcal{F}_C(\omega) \propto \sum_h \delta(\omega - h\omega_S)$ [33].

This effect is schematically shown in Fig. 2.2.²

It is possible to demonstrate that the modulation of a bandlimited input signal with the sampling comb creates a signal with a Fourier transform periodical with period f_S . Two cases can happen depending on the Nyquist frequency of the original signal: (we define a “band” as a frequency interval f_S -wide centered in an integer multiple of f_S , see Fig. 2.2)

$f_N < f_S/2$

In this case there is no overlap between two adjacent frequency

²The definition of the discrete Fourier Transform given in the previous section can also be regarded as the continuous transform of Eq. 2.8, apart from the periodicity in the frequency domain.

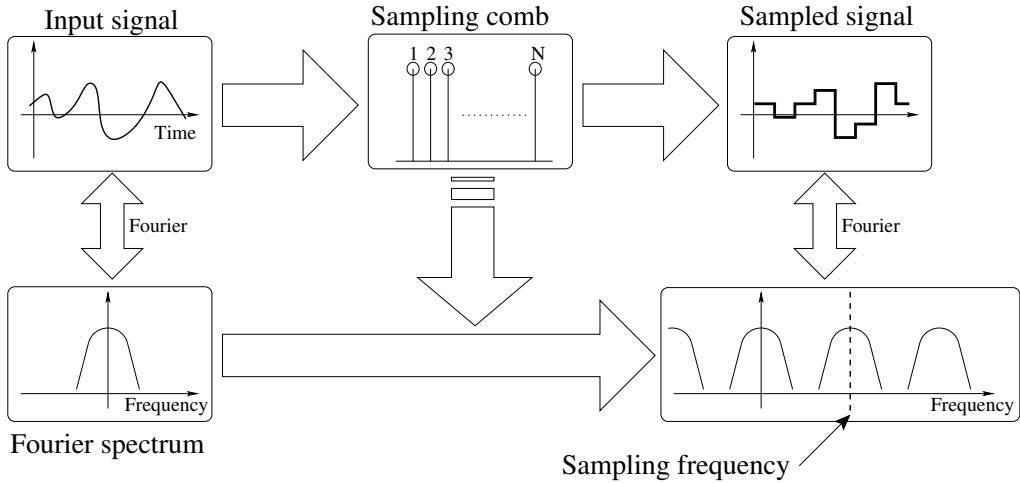


Figure 2.2: Effect of sampling in the frequency domain. On the left a bandlimited input signal and its Fourier spectrum are shown. On the right the results obtained sampling that signal. Note the periodicity modulo f_s of the Fourier transform after sampling. The figure shows the case of a Nyquist frequency $f_N < f_s/2$.

bands. Each band is well separated from its neighbours and then it can be separated without any distortion if desired (for example with a band-pass filter).

$f_N > f_s/2$

In this case there is overlap between two adjacent bands. Each band contains additional frequency components that were not present in the original continuous signal. This is called “aliasing”. It is no more possible to recover the original frequency spectrum from the sampled one.

Aliasing is a usually unwanted phenomenon that occurs when the sampling frequency of the AD converter is less than $2f_N$ of the input signal. This is contained also in the following theorem:

Sampling Theorem

Given a continuous bandlimited function $S(t)$ with $\mathcal{F}_S(\omega) = 0$ for $|\omega| > 2\pi f_N$, the function can be perfectly reconstructed from a noiseless sampling $S[k]$ at any frequency $f_s > 2f_N$. The reconstruction formula is given by:

$$S(t) = \sum_{k=-\infty}^{+\infty} S[k] \cdot \text{sinc}(t/\tau_{\text{clk}} - k) \quad (2.9)$$

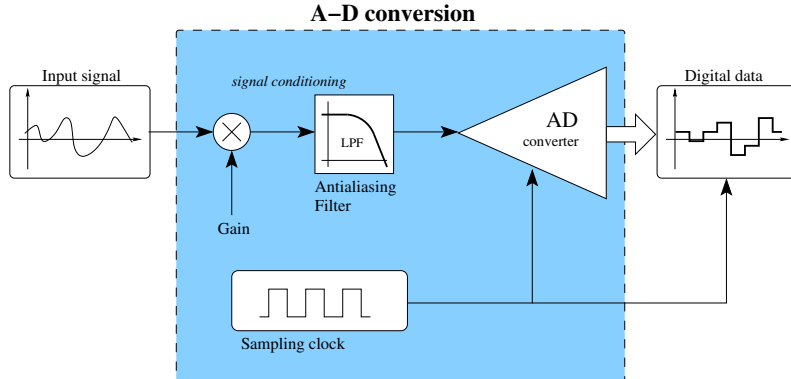


Figure 2.3: Typical ADC configuration. The input signal is first amplified or attenuated in order to have an optimal match with the input range of the AD converter. A proper antialiasing filter is then applied before the sampling.

with the definition $\text{sinc}(x) = \frac{\sin(\pi x)}{\pi x}$.

For a proof of this theorem as well as a detailed discussion of aliasing see [29, 30].

It has to be noted that the reconstructed signal $S(t)$ of Eq. 2.9 is simply obtained as a discrete convolution between the sampled sequence $S[k]$ and the function $\text{sinc}(x)$ (that sometimes is called “interpolation kernel”). More details about signal interpolation will be given in §3.4.1.

Because of the aliasing effect a typical ADC configuration includes an analog “antialiasing filter” to remove frequencies above $f_s/2$ that may be present in the input signal (see Fig. 2.3). The performances and the complexity of this analog filter vary depending on the particular application: in §3.1 an example will be briefly presented.

2.4.3 Sampling and quantization noise

The total output noise from an AD converter can be schematized as the (uncorrelated) sum of two noise contributions: one coming from the quantization process (in the following called “quantization” noise, directly related to the physical number of bits of the converter) and one coming from the internal processing of the ADC prior to quantization (in the following called “sampling” noise, directly related to the effective number of bits of the converter).

The quantization process can be mathematically treated as a non-linear operator applied to the input signal. For each non-quantized

sample $S_{\text{n.q.}}[k]$ a quantized sample $S[k]$ is produced such that

$$S[k] = \text{round} \left(\frac{2^{\text{bit}}}{R} S_{\text{n.q.}}[k] \right) \quad (2.10)$$

where R denotes the full range of the ADC in the used configuration, and the rounding operator `round()` has been introduced.³

Thus for quantization error $\Delta_k = S[k] - S_{\text{n.q.}}[k]$ we have $-\frac{1}{2}$ LSB $\leq \Delta_k \leq \frac{1}{2}$ LSB.

Depending on the importance of the quantization error Δ_k with respect to the noise characterizing the ADC analog input two scenarios are possible:

small Δ_k

(this is the most common scenario) In realistic operating conditions [29] the quantity Δ_k can be schematized as a random stationary white [34] variable with a uniform distribution and no correlation with the original sequence $S_{\text{n.q.}}[k]$. With these hypotheses it is possible to compute the mean value of Δ_k as 0 LSB and the variance σ_Q^2 of the quantization error in analog input units as:

$$\sigma_Q^2 = \frac{R^2}{12} \cdot \frac{1}{4^{\text{bit}}} \quad (2.11)$$

where R is the full ADC range.

large Δ_k

In this scenario the white-noise approximation is no more applicable, for example because no dithering [29] occurs to mitigate the quantization effects. An analytical treatment of this case is difficult, and thus a full simulation of the process is advisable.

In §2.2 the concept of effective number of bits of a converter has been introduced. This effect can be schematized as an additional white-noise source fed into the input of the converter. Thus for the total variance of a sampling ADC having ENOB effective bits and B “physical” bits we have (in the white quantization noise hypothesis):

$$\begin{aligned} \sigma_{\text{ADC}}^2 &= \frac{R^2}{12} \left[\frac{1}{4^B} + \frac{1}{4^{\text{ENOB}}} \right] = \frac{R^2}{12} \cdot \frac{1}{4^{\text{ENOB}}} \left[1 + \frac{1}{4^{B-\text{ENOB}}} \right] \\ &\approx \frac{R^2}{12} \cdot \frac{1}{4^{\text{ENOB}}} \end{aligned} \quad (2.12)$$

where the last approximation derives from noting that for many commercial ADCs $B-\text{ENOB} \approx 1-2$ LSB.

The overall sampling plus quantization noise is then dominated by

³It can be easily seen than the choice of a truncating operator instead of a round one would not affect this discussion.

the effective number of bits of the converter.

With the hypothesis of a white-noise spectrum, the spectral noise density due to the sampling process is simply given by⁴

$$w_{\text{ADC}}(\omega) = \begin{cases} \sigma_{\text{ADC}}^2 \frac{2}{f_s} & ; \quad \text{if } f < f_N \\ 0 & ; \quad \text{otherwise} \end{cases} \quad (2.13)$$

2.4.4 FIR and IIR digital filters

In linear signal processing (both analog and digital) we are often interested in the attenuation or enhancement of some frequencies of the input signal. This is accomplished using linear filters.

In general a linear time-invariant filter is completely defined given its response $G(t)$ to a δ -like excitation [28, 29]. In fact, processing an input signal $S(t)$ with a filter having response function $G(t)$ produces an output $R(t)$ given by:

$$R(t) = \int_0^t S(\tau)G(t - \tau)d\tau = (S * G)(t) \quad (2.14)$$

Thus the output $R(t)$ is given by a folding integral between $G(t)$ and $R(t)$.

In the same way, the digital filtering of a sequence $S[k]$ to give an output sequence $R[k]$ can be obtained with a discrete convolution of $S[k]$ with a proper discrete response function $G[k]$. This is practically possible only if the sequence $G[k]$ has a finite length, and thus digital filters implemented as direct convolution are called FIR digital filters (Finite Impulse Response).

As an example of the opposite case, i.e. an infinite-response system, let us consider, with reference to Fig. 2.4, the response function of an RC low-pass circuit:

$$G(t) = \begin{cases} \frac{1}{RC} \exp\left(-\frac{t}{RC}\right) & ; \quad \text{if } t > 0 \\ 0 & ; \quad \text{if } t < 0 \end{cases} \quad (2.15)$$

The digital equivalent of this response function is:

$$G[k] = \begin{cases} \frac{1}{RC} \exp\left(-\frac{k\tau_{\text{clk}}}{RC}\right) & ; \quad \text{if } k \geq 0 \\ 0 & ; \quad \text{if } k < 0 \end{cases} \quad (2.16)$$

It has to be noted that the sequence $G[k]$ of equation Eq. 2.16 has an infinite length and thus it cannot practically be implemented as a

⁴In Eq. 2.13 a perfect antialiasing filter cutting at the Nyquist frequency has been assumed.

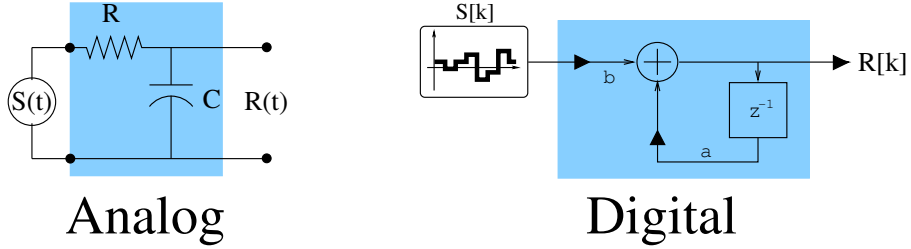


Figure 2.4: Equivalence between a particular analog filter (simple RC low-pass) and a 1-pole digital filter. See text for details.

FIR filter. The output of this system to a general input $S[k]$ can be mathematically computed as:

$$R[k] = \sum_{h=0}^k S[h] \cdot \frac{1}{RC} \exp\left[-\frac{(k-h)\tau_{\text{clk}}}{RC}\right] \quad (2.17)$$

With some algebra it is possible to note that the following holds:

$$R[k] - \exp\left(-\frac{\tau_{\text{clk}}}{RC}\right) \cdot R[k-1] = \frac{1}{RC} S[k] \quad (2.18)$$

Eq. 2.18 implements a *recursive* computation of the output sample $R[k]$ given the input sample $S[k]$ and the already computed output $R[k-1]$. A schematic view of this implementation is given in Fig. 2.4 (right). Digital filters implemented recursively are usually called IIR digital filters (Infinite Impulse Response).⁵

A general IIR system is defined by:

$$R[k] - \sum_{h=1}^N a_h R[k-h] = \sum_{h=0}^M b_h S[k-h] \quad (2.19)$$

Once the recursion coefficients $\{a_h\}$ and $\{b_h\}$ have been determined for a particular filter (for that purpose very sophisticated methods exist, see for example [29] and §3.3.5) the application of Eq. 2.19 allows a very computational efficient implementation of the desired filter (for example, in the simple case of the RC low-pass filter, only

⁵It has to be noted that some *finite* response filters may have also a recursive implementation. An example is the moving average defined as $R[k] = \frac{1}{N+1} \sum_{h=0}^N S[k-h]$ (FIR version). This is equivalent to $R[k] - R[k-1] = \frac{1}{N+1} (S[k] - S[k-N-1])$ (IIR version). To be strictly correct, for these type of filters the definition “Recursive filters” instead of “IIR filters” would be more appropriate.

two multiplications and two additions are required to compute one output sample).

Making use Eq. 2.6, we can see that the digital filter defined with Eq. 2.19 has the following \mathcal{Z} transform:

$$\mathcal{Z}(z) = \frac{b_0 + b_1 z^{-1} + \dots + b_M z^{-M}}{1 - a_1 z^{-1} - \dots - a_N z^{-N}} \quad (2.20)$$

The “poles” of the filter are then defined as the (complex) roots of the polynomial $(1 - a_1 z^{-1} - \dots - a_N z^{-N})$, whereas the “zeros” are the roots of $(b_0 + b_1 z^{-1} + \dots + b_M z^{-M})$.

Equation 2.20 plays a very important role in the design of digital filters. For any filter having a rational \mathcal{Z} transform given by the ratio of two polynomials in z , it is possible to re-write it in the form of Eq. 2.20 and then directly obtain a very efficient digital filter implementation as in Eq. 2.19.

In spite of its computational efficiency, the use of a recursive formulation has an important drawback: when the intermediate computations are performed with a finite precision (i.e. $R[k]$ and/or the coefficients $\{a_h\}$, $\{b_h\}$ are rounded to the machine precision) the errors on the $R[k-1], R[k-2], \dots, R[k-N]$ can accumulate and influence the computation of $R[k]$. This effect distorts the desired output of the filter and moreover in some cases it can give a nearly unpredictable behaviour depending on the very details of the input signal and of the filter [29].

This problem can be solved by rearranging the computations in Eqs. 2.20 and 2.19 in various ways [29]: although each of these “forms” has identical impulse response in the case of infinite precision computations, they may have a very different behaviour with respect to finite precision implementations, and they pose different hardware requirements for efficient implementation. As an example, in Fig. 2.5 two simple equivalent implementations of a biquad digital filter ($N = M = 2$ in Eq. 2.19) are shown. On the left a “direct form I” implementation is shown, that is simply the block representation of Eq. 2.19. On the right a “direct form II” structure is shown: this structure is also referred to as “canonic form implementation” because it minimizes the needed number of delays z^{-1} (in this example 2 delays are needed instead of 4 for the Direct Form I structure).

These important topics are fully discussed in [29] and they will not further addressed here.

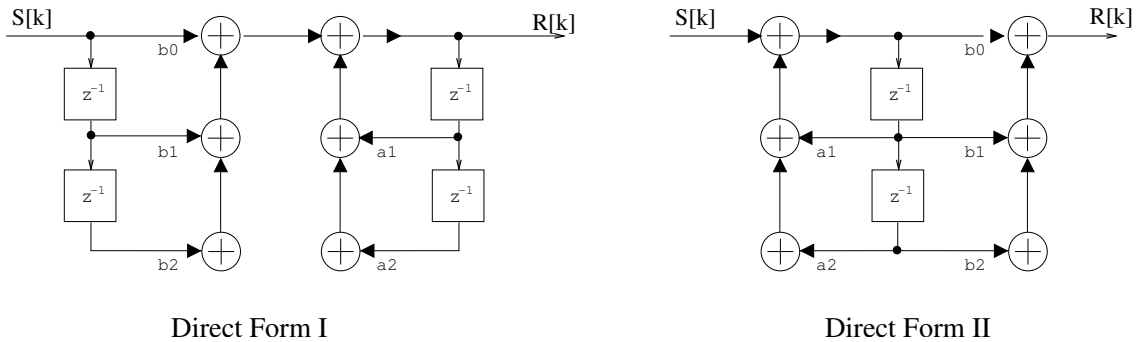


Figure 2.5: Block diagrams of a direct recursive filter implementation as in Eq. 2.20. Examples of Direct Form implementations of a biquad filter.

2.5 Digital signal processors

As we have seen in the previous section Digital Signal Processing is carried out mainly by mathematical operations. This is somewhat different from the typical operations requested, for example, to a personal computer where for many applications an important fraction of the processing power is used for data collection/sorting and only a few for mathematical operations. Processors used for personal computing have thus not been targeted to high-performance math computations and for example MMX, SSE and similar SIMD (Single Instruction Multiple Data) instructions [27] are a relatively recent addition to the basic x86 instruction set. A different class of processors have thus been developed specifically targeted to digital signal processing, the “digital signal processors” (DSPs). These are the main differences with respect to a standard processor:

Instruction set

The instruction set of a DSP processor usually includes, apart from standard operations, a set of instructions able to perform multiple operations in one clock cycle. A typical one is the Multiply and ACCumulate (MAC) instruction, where the DSP performs simultaneously 1 multiplication, 1 addition and a memory fetch (reading one or more values from memory). This instruction (and similar ones) is extremely useful for example in the implementation of digital filters like in Eq. 2.19.

Hardware support for loops and circular buffers

The implementation of a recursive digital filter requires, apart from MAC operations, a control loop for looping over the samples and a delay line for storing the intermediate values. Many

DSPs have a hardware support for loops and circular buffers so that the software operations needed to check for the end of the loop and for managing the delay line can be avoided, thus saving considerable processing time.

Multicore architecture

Many (high end) DSPs have a multicore architecture: this effectively means having twice the processing power (or possibly more) controlled by a single software. This for example makes it possible to apply in parallel two different digital filters to one input signal.

High-speed Input/Output

DSP processor are usually equipped with high-speed input and output interfaces (both parallel and serial) in order to provide a simple and fast communication channel to other peripherals, like ADCs, DACs or memories.

No external hardware

A typical DSP processor is usually meant to be used in a standalone configuration, and thus almost no external hardware is needed to run a DSP processor inside a digital signal acquisition system. On the contrary, standard processors usually rely on external hardware like controllers, bridges, . . . , for proper operation (see [27] for some examples).

For a general introduction to DSPs see [30].

To achieve maximum performances, apart from a careful optimization of the algorithms, a typical DSP processor will be directly programmed in its own assembler language. This requires a deep knowledge of the internal structure of the DSP. It can be non portable to other DSPs (with an exception for processors belonging to the same family from the same manufacturer), and it can be somewhat time consuming. On the other side, many manufactures provide a C or C-like compiler for their DSPs that allows an implementation of the processing software in a higher level language like C [35]. This speeds up considerably the developing time but it usually does not reach the same performances level of an assembly-written software.

In the last years DSPs are being replaced in some applications with FPGAs (Field Programmable Gate Arrays, [27, 36]). Although the complexity of the algorithms than can be implemented on such devices is limited with respect to DSPs capabilities, other factors like costs, speed and integration with existing hardware make these devices an alternative to DSP processors.

Chapter 3

Digital signal processing for Nuclear Physics

In this chapter the digital signal processing hardware and software that have been developed during this Thesis for measurements in nuclear physics will be presented.

The experimental tests performed (see Chap. 4) are mainly related to Heavy-Ion experiments for nuclear dynamic and thermodynamic studies (see also §1.1). However, the algorithms presented in this chapter (in particular the detailed discussion on energy measurements) are meant to be general enough to find application in other areas, as for example in Nuclear-Structure measurements.

Firstly a brief introduction on the developed hardware will be given, mainly focusing on the few key parameters that influence the “quality” of the collected data, as for example the choice of the Analog to Digital Converter. In §3.3 and §3.4 a detailed discussion of the developed algorithms for high-resolution energy and timing measurements will be presented, together with an investigation of the main ADC and noise properties that affect their performances. It has to be noted that a very wide class of detectors can be properly handled once the digital system is able to perform good energy and timing measurements (with their variants).

In §3.5 a method developed for fast signal fitting (which has no analog counterpart) will be briefly presented, whereas in §3.6 some details about the software that has been developed for testing the algorithms will be given.

Experimental data obtained using these algorithms will be presented in Chap. 4.

All the proposed algorithms have been designed for on-line processing of signals, thus being simple and fast. Many of them have been also translated into a DSP software that is now under test [37].

3.1 The choice of an analog to digital converter

The main properties of Analog to Digital Converters have already been discussed in §2.2. It has been explained that the two key parameters for choosing an ADC are the sampling rate and the effective number of bits. It is then important to understand what are the requirements of the experiment in terms of resolution and sampling period τ_{clk} .

In the following sections a detailed discussion of the effect of these parameters on the various measurements will be presented. As a rule of thumb we can say that the converter of choice must satisfy the following points (that are related each other):

1. Sampling and quantization noise (see §2.4.3) must be smaller than the intrinsic analog noise of the front-end electronics connected to the detector.
2. Once point 1. is satisfied, the fastest ADC available on the market can be chosen, taking also into account power dissipation and cost.

In §1.2 and §1.3 the intrinsic resolutions and characteristics of the output of some nuclear detectors have been discussed, together with the experimental features requested by the next generation detection systems. The typical time scales of the current pulses range from few nanoseconds to several microseconds, with a dynamic range (or signal-to-noise ratio) of about 100–3000. The typical bit resolution of Peak Sensing ADCs [14] used in standard spectroscopy systems is 12–13 bits.

Taking into account these considerations the first prototype of digital sampling system (custom designed and built in the mid of 2000, see [1, 2]) uses a 12 bit (10.8 effective) 100 MS/s converter from Analog Devices (AD9432). At that date this converter was the only available choice on the market meeting our requirements; the AD9432 was indeed tested as soon as released by the manufacturer. As presented in Tab. 2.1 the actual situation (at the time of this writing) has slightly improved, although the number of available converters with resolution greater than 12 bit and speed greater than 100 MSamples/s is still very limited.

To achieve these performances the AD9432, as well as other converters, employs a pipelined conversion technique. A simplified view of this method is shown in Fig. 3.1, where a 8 bit ADC is considered as an example.

The input signal undergoes a first AD conversion at low resolution

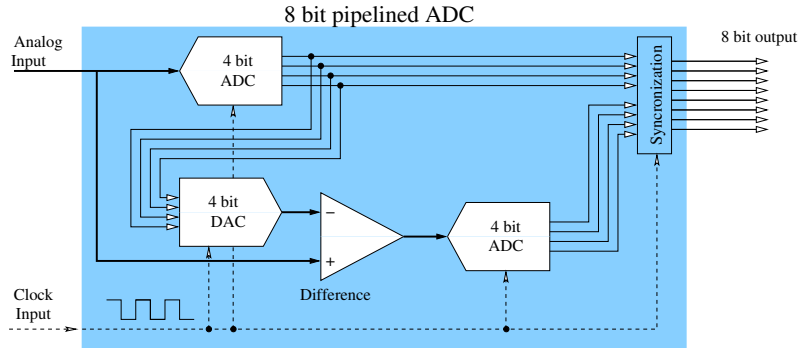


Figure 3.1: Ideal schematic of an 8 bit pipelined Analog to Digital Converter. The Sample and Hold system is not shown.

(typical: 4 bit) using techniques like Flash conversion (see §2.2). The obtained digital code is converted back to analog using a DA converter in order to compute the difference between the analog input and the converted value. This difference, possibly amplified, is converted by a second Flash converter. This method is called also “sub-ranging”, because of the different equivalent input ranges of the two internal ADCs (in Fig. 3.1 about a $1/2^4$ ratio holds). The system depicted in Fig. 3.1 performs a correct conversion as long as the input signal does not change significantly during 3 clock cycles (one for the first AD conversion, one for the DA conversion, one for the final AD conversion). To overcome this limitation, commercial ADCs include a sample and hold system [27] able to store the analog value with the proper synchronization.

As discussed in §2.4.2 the input signal must be filtered prior to sampling in order to avoid the aliasing effect. A proper analog antialiasing filter has thus been employed, and a full description and its schematics can be found in [1, 2]. Briefly, the filter uses a 3-pole active Bessel configuration [27, 36] in order to minimize signal distortion. The filter noise is well below the equivalent of 1 LSB of the converter. In the design phase extensive simulations have been done with the SPICE simulator [38] and reported in [1, 2].

3.2 Modular DSP electronics

The converter described in the previous section has been used in a prototype system fully described in [1, 2]. The configuration used in the prototype board is shown in Fig. 3.2 (left). The prototype does

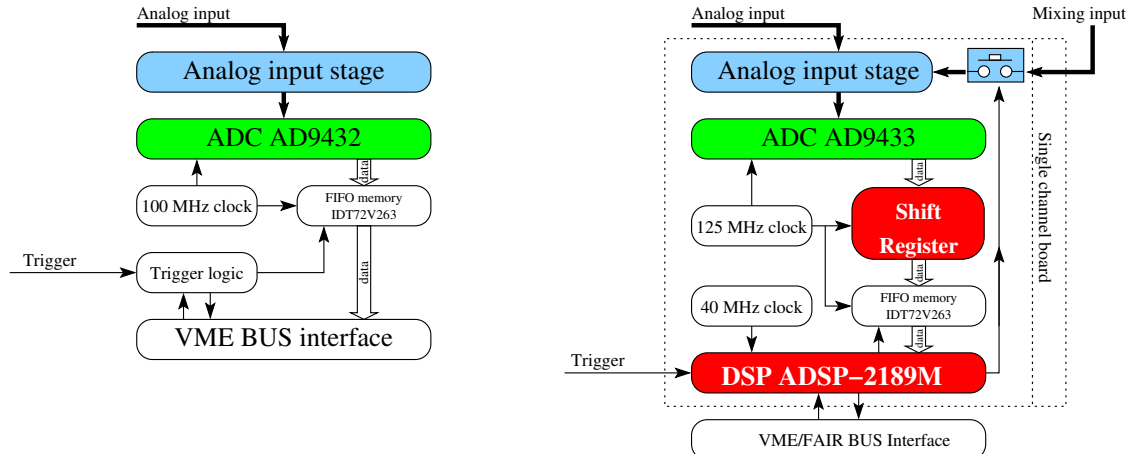


Figure 3.2: Block diagram of a custom digital-sampling hardware targeted to nuclear-physics applications. On the left: block diagram of a first prototype without signal-processing capabilities. On the right: block diagram of an improved version with on-board DSP and signal-mixing capabilities. See text for details.

not provide any on-line signal-processing capability, because after each data acquisition it transfers the complete acquired waveform to the acquisition system. This solution is clearly unfeasible for a large scale application of the device (the requirements on data transmission and storage would be unacceptable even for a relatively small experiment), but it has allowed detailed off-line studies of the characteristics of the acquired signal waveforms. Various algorithms (see §3.3, §3.4, and §3.5) have been developed and optimized analyzing data obtained from different detectors (for the experimental results see Chap. 4) and then it is now possible to implement them into an on-line signal-processing system.

A new modular system has thus been developed [39] including an on-board DSP for on-line signal processing. The system is meant to be used in the GARFIELD [40] experiment for the NUCL-EX collaboration. Its block diagram is shown in Fig. 3.2 (right).

The main differences with respect to the original prototype are the use of a faster AD converter (AD9433, 125 MS/s 12 bit) and the presence of a DSP processor (fixed point ADSP2189 from Analog Devices). Data coming from the ADC are stored in a temporary memory (the function of the shift register is discussed in §3.3.1 and §3.3.2) that is subsequently read by the DSP. At boot time a suitable DSP software is loaded into the processor (through the acquisition interface)

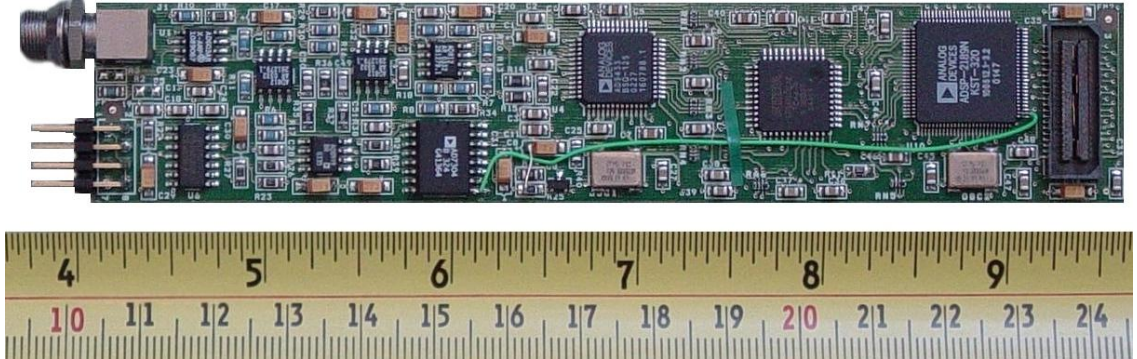


Figure 3.3: Photo of a single digital acquisition channel of the custom modular system described in the text. The board size is about 14×2.5 cm 2 . An on-board DSP is included.

depending on the information that needs to be extracted from the collected waveforms. The few extracted values are then transferred to the general acquisition system of the experiment. Each channel of the modular system is also provided with a common mixing analog input in order to apply the time-of-flight or coincidence method discussed in §3.4.4.

Both the prototype and the new system use a trigger-based acquisition logic. Whereas the AD converter is continuously running,¹ the signal waveform is stored on the FIFO memory (and possibly processed) only when a general trigger signal is received by the board. More details about the used trigger logic are presented in §3.3.1 and [1, 15].

From the electronic/mechanical point of view, the new system employs a highly modular design: each acquisition channel is realized on a small sized board that houses the whole electronics needed for a complete signal acquisition and on-line processing (a photo of a single channel PCB is presented in Fig. 3.3). Each of these single channel boards is connected to a “motherboard” card able to house up to 8 channels. The motherboard acts as a complex interface between the DSPs and the acquisition system, and makes it possible to integrate the card with standard VME [41] or FAIR [42] acquisition systems. The FAIR acquisition interface will be used inside the GARFIELD [40] apparatus, that planned an upgrade based on these sampling systems.

¹This is the recommended solution in order to maintain a good stability of the AD conversion against temperature and counting rate.

3.3 Digital amplitude measurements

Many nuclear-physics detectors give an output pulse having an amplitude or an integral proportional to the energy loss of the particle in the active volume of the detector. Several electronic configurations exist for processing the output of a nuclear physics detector. This discussion will focus on a charge preamplifier one that, as discussed in §1.2.7, is the usually preferred configuration for high-resolution detectors (like germanium or silicon). However the main points of this discussion can also be applied, with minor modifications, to other configurations.

In the first section a distinction between two different configurations used in digital sampling systems relevant for the purposes of energy measurements is presented. The computation of the digital energy resolution achievable taking into account the problem of baseline determination and signal shaping is reported. Then a very simple and fast algorithm to be used with low energy resolution detectors is presented. Finally an example of design of the “exact” digital equivalent of a standard analog spectroscopy amplifier is described.

3.3.1 Event-based and continuously running digital systems

From a structural point of view, digital sampling systems can be divided in event-based systems and continuously running ones. The analog to digital converter is almost always used in a free-running configuration, i.e. a digital data stream with fixed sampling period τ_{clk} is produced at any instant. The main difference between these two configurations resides in the way the digital data are on-line analyzed and in the resulting hardware and software requirements.

In event-based systems (as the one described in §3.2) the DSP processor or FPGA device connected to the AD converter is usually in an idle state, waiting for the arrival of a logic trigger signal. Thus the digital data stream coming out from the converter is normally ignored and no digital signal processing is performed. When a detector event occurs a logic signal is generated by some ancillary analog system (possibly physically integrated into the ADC board) and used to trigger the digital system. Once this “first level” trigger has been fired, the DSP processor transfers into its memory the digital data pertaining to the time window of the current event and starts performing the desired computations. With this simple configuration the DSP would not be able to acquire the very rise of the signal, which is the portion that generated the trigger. To overcome this strong limitation, a circular

buffer is usually inserted between the AD converter and the DSP system (this is the purpose of the block named “shift register” in Fig. 3.2). Old samples are discarded and new samples are stored in such a way that at each instant the last T_{BL}/τ_{clk} converted samples are available. With this modification the triggered DSP is able to include in its processing a “baseline time” T_{BL} preceding the arrival of the detector signal.

On the contrary, in continuously running systems the digital data stream coming from the AD converter is continuously processed by a DSP or FPGA device. This poses no restriction on the available T_{BL} time preceding each signal and thus, at variance with respect to event-based systems, effectively makes it possible to fully realize digital equivalents of standard analog systems (that do not have any limitation on T_{BL}). To achieve these results the processing speed must be high enough to withstand the output data rate of the AD converter.

The latter point is relevant in order to define the hardware and software requirements needed for a continuously running digital system: the acceptable input rate of the digital-processing section (either made using a DSP or FPGA device) must be equal or greater than the ADC throughput rate. Depending of the AD converter used, this requirement may severely restrict the available choices of the processing hardware: for example if a ~ 100 MSamples/s converter is used (as in §3.2 or in the proposals [18, 19]), only fast FPGAs would be feasible, ruling out most – if not all – of the today available DSP processors on the market. On the contrary, an event-based system can afford the use of less performing DSPs, due to the fact that the digital data stream is memorized on the temporary buffer. This allows the use of more sophisticated algorithms that can be easily coded for DSP hardware, taking full advantage of the flexibility of these processors with respect to FPGAs. For example the same event dataset can be processed using two or more non-parallelizable algorithms, while this task is difficult or hardware-expensive to accomplish using FPGAs.

In conclusion, continuously running systems are the option of choice for applications where the ultimate counting rate capability and energy resolution (due to no T_{BL} restrictions, see §3.3.3) are of paramount importance and relatively simple algorithms can be used. On the contrary, the use of more sophisticated algorithms (with the added bonus of the possible use of DSP processors that give a much greater flexibility and ease of programming) is possible in event-based systems.

The systematic study of digital energy measurements using continuously running systems has been carried out in several papers from E.Gatti *et al.* (see for example [43] and references therein), taking into account various experimental conditions and looking for the optimal

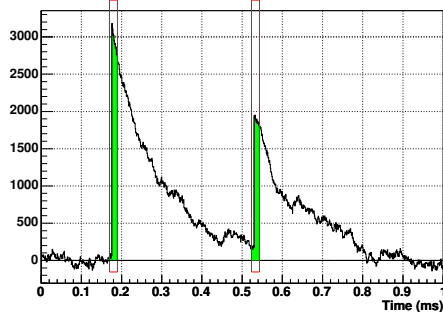


Figure 3.4: Example of the output of a charge preamplifier over a long time scale. Two distinct events can easily be seen. The shaded areas correspond to the time windows available to an event-based system.

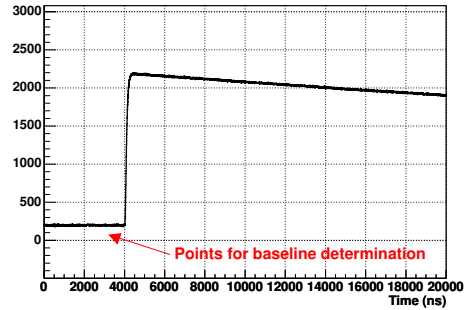


Figure 3.5: Example of digitized event to be used in an event-based analysis. Note the very different time scale with respect to the one used in Fig. 3.4.

choice of the various processing parameters (i.e. the parameter set that gives the best resolution for a given experimental configuration).

The topic of the restriction to a finite time window that occurs in event-based system is a liming factor for high-resolution energy measurement that has not yet been addressed in the literature: in the following sections some details are presented.

The discussion will be limited to low counting-rate experiments, where pile-up effects can be neglected.

3.3.2 Baseline determination

In event-based digital systems only a portion of the detector output is available for signal processing, i.e. all the relevant information must be extracted by the available T_{BL}/τ_{clk} samples before the rise of the signal (T_{BL} is the “baseline time”) and the following samples. A visual representation of the actual situation is presented in Fig. 3.4, where a typical output of a charge preamplifier over a relatively long time scale is shown. Two distinct events can easily be seen, together with the corresponding time windows used by an event-based system (supposed to have $T_{BL} = 4 \mu s$ and a total measuring time of $20 \mu s$). It is possible to see that the output of a realistic charge preamplifier is apparently characterized by a low-frequency noise, due both to the intrinsic preamplifier properties (see §1.2.4) and to pick-up and inter-

ferences from the experimental environment (a typical example is a ~ 50 Hz noise related to the power lines). In Fig. 3.5 an example of acquired digital sequence is presented: its main feature is the presence of a finite time T_{BL} ($4 \mu\text{s}$ in the figure) preceding the rise of the detector signal.

The natural choice for obtaining a high-resolution energy measurement from a sampled sequence $S[k]$ like that in Fig. 3.5 is the application of a digital shaping filter similar to the ones used in analog systems, for example a CR-RC⁴ network (see §1.2.7). This is often the option of choice for continuously running systems where, as in the analog counterparts, no restriction on T_{BL} is present, and thus the digital filter as the analog one is allowed to use as much signal information as needed for its proper operation.

On the contrary, this method cannot directly be applied to the case of finite T_{BL} : the associated difficulties are schematically shown in Fig. 3.6 (and they will be mathematically treated later). From the filter point of view, the constant baseline value is treated as a suddenly applied step signal at the time conventionally chosen as $t = 0$, i.e. the starting time of the sampled sequence $S[k]$. The response of a CR-RC⁴ filter when a constant value is applied as input is asymptotically zero, but the settling time needed to approximate this value is of the order of several shaping time constants τ_{sha} . For example the time needed for a CR-RC⁴ filter to filter an input step down to 0.1% of its initial value is $\sim 17 \tau_{sha}$. As shown in Fig. 3.6 the settling time is thus long enough to give a significant contribution in the time range where the maximum of the shaped signal is reached, that is the time region where the actual energy measurement is performed ($4\tau_{sha}$ for a CR-RC⁴ filter). Any fluctuation in the baseline level thus translates in an added noise contribution to the determination of the signal amplitude, thus significantly deteriorating the achievable energy resolution.

An intuitive solution to this problem, which have a simple implementation, is the determination and subtraction of the average baseline value of the current event: this allows the use of the digital shaping filter in better conditions (apart from residual baseline determination errors, see the following discussion). For each event the baseline is estimated as an average of the N_{BL} samples available in the first portion of the signal:

$$BL = \frac{1}{N_{BL}} \sum_{k=1}^{N_{BL}} S[k] \quad (3.1)$$

The obtained BL value is then subtracted from the whole sequence $S[k]$, and a digital shaping filter is applied.

Following this qualitative description, a quantitative computation

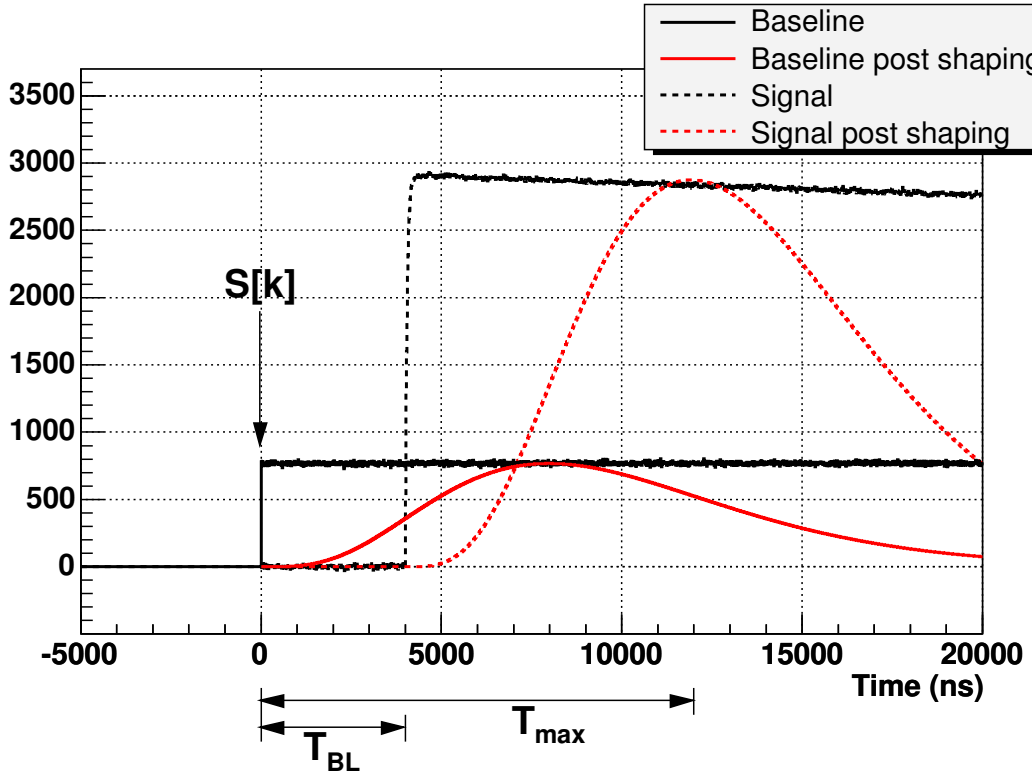


Figure 3.6: Shaping of a digital acquired signal $S[k]$ taking into account the presence of a finite T_{BL} ($T_{BL} = 4 \mu s$ in the figure). The baseline is treated by the filter as a step at $t = 0$. A normalization of $1/\gamma$ (Tab. 1.2) has been applied to the filter output for a better presentation.

of the noise properties of the system can be performed, taking into account the possibility of a baseline subtraction. It is important to note that this computation cannot be performed in the frequency domain because the acquired sequence $S[k]$ is non stationary, since $S[k] = 0$ for times $t < 0$. The evaluation must be carried out in the time domain.

The signal $S'[k]$ after baseline subtraction can be decomposed into its noise and signal components:

$$S'[k] = S[k] - BL = n[k] + S_{step}[k] - BL \quad (3.2)$$

where $S_{step}[k]$ is the noiseless ideal signal to be measured ($S_{step}[k] = 0$ for $t < T_{BL}$, having for example a step-like shape), and $n[k]$ an added noise component. With this notation, the subtracted BL value is thus given by $BL = \sum n[k]/N_{BL}$, with $1 \leq k \leq N_{BL}$.

For a noisy preamplifier with a zero DC offset in the output, $n[k]$

(and thus BL) has zero expectation value. When a non-zero offset (possibly slowly varying) is present, the baseline subtraction method (Eq. 3.2) allows a compensation of this effect. Therefore, no hypothesis on the $n[k]$ expectation value is required for the following computations.

A shaping filter is applied to $S'[k]$, giving the output $R[k]$:

$$R[k] = \sum_{h=1}^k S'[h]G[k-h] \quad (3.3)$$

where, as usual, the filter response to a δ -like input signal is denoted by $G[k]$. The integral of $G(t)$ (i.e. the response of the filter to a perfect step) will be denoted with $G_{\text{step}}(t)$.

With reference to Fig. 3.6, the overall energy resolution (in shaper output units²) can be computed as the variance of $R[k]$ at the desired time T_{\max} (where $T_{\max} > T_{\text{BL}}$). The following equation is obtained ($N_{\max} = T_{\max}/\tau_{\text{clk}}$):

$$\begin{aligned} \sigma_{\text{full}}^2(T_{\max}) &= \mathbb{E}_e \left\{ \left(S'[N_{\max}] - S_{\text{step}}[N_{\max}] \right)^2 \right\} = \\ &= \mathbb{E}_e \left\{ \left(\sum_{h=1}^{N_{\max}} (n[h] - \text{BL}) G[N_{\max} - h] \right)^2 \right\} \end{aligned} \quad (3.4)$$

where the notation $\mathbb{E}_e\{\theta\}$ represents the expectation value [16] of the quantity θ over an ensemble of events. The noisy samples $n[k]$ are supposed to be described as a stationary random process with an autocorrelation function [16] $\mathcal{R}(t)$.

The following quantity (or similar ones) is needed in the computation of Eq. 3.4:

$$\mathbb{E}_e \left\{ \sum_{k,h=1}^N n[k]n[h] \right\} \stackrel{\text{ergodic}}{=} \sum_{k,h=1}^N \mathbb{E}_t \left\{ n[k]n[h] \right\} = \frac{1}{\tau_{\text{clk}}^2} \iint_{x,y=0}^T dx dy \mathcal{R}(x-y) \quad (3.5)$$

The first equivalence follows from an ergodic hypothesis on the system, i.e. the equivalence between averages $\mathbb{E}_e\{\theta\}$ computed over ensemble of events and averages $\mathbb{E}_t\{\theta\}$ computed over time for a single

² In order to obtain the resolution in preamplifier output units or for comparison between different filters with different gain, a normalization factor $G_{\text{step}}^2(T_{\max} - T_{\text{BL}}) = \gamma^2$ (Tab. 1.2) must be applied.

event. The second equivalence follows from the stationary process hypothesis of $n[k]$ and from passing to continuous variables ($T = N\tau_{\text{clk}}$).

It has to be noted that the quantity BL in Eq. 3.4 is not a constant but rather a value extracted from the noisy samples $n[k]$ for $1 \leq k \leq N_{\text{BL}}$.

Carrying on the computations, the energy resolution becomes:

$$\begin{aligned} \sigma_{\text{full}}^2(T_{\max}) &= \underbrace{\iint_{x,y=0}^{T_{\max}} G(T_{\max} - x) G(T_{\max} - y) \mathcal{R}(x - y) dx dy}_{\textcircled{1}} + \\ &+ \frac{1}{T_{\text{BL}}^2} \underbrace{\left[\int_{x=0}^{T_{\max}} G(T_{\max} - x) dx \right]^2}_{\textcircled{2}} \cdot \underbrace{\left[\iint_{x,y=0}^{T_{\text{BL}}} \mathcal{R}(x - y) dx dy \right]}_{\textcircled{3}} + \\ &- \frac{2}{T_{\text{BL}}} \underbrace{\left[\int_{x=0}^{T_{\max}} G(T_{\max} - x) dx \right] \cdot \left[\int_{x=0}^{T_{\max}} dx \int_{y=0}^{T_{\text{BL}}} dy G(T_{\max} - x) \mathcal{R}(x - y) \right]}_{\textcircled{4}} \end{aligned} \quad (3.6)$$

When baseline subtraction is not performed, only the term $\textcircled{1}$ must be retained.

A more manageable expression of $\textcircled{1}$ and $\textcircled{3}$ can be obtained with the substitution $\delta = x - y, \kappa = x + y$, performing the integral in the resulting (δ, κ) plane, and noting that by definition $\mathcal{R}(x) = \mathcal{R}(-x)$. One then obtains:

$$\begin{aligned} \textcircled{1} &= \int_{\delta=0}^{T_{\max}} d\delta \int_{\kappa=\delta}^{2T_{\max}-\delta} d\kappa G\left(\frac{\kappa+\delta}{2}\right) G\left(\frac{\kappa-\delta}{2}\right) \mathcal{R}(\delta) \\ \textcircled{3} &= 2T_{\text{BL}} \int_{\delta=0}^{T_{\text{BL}}} \mathcal{R}(\delta) \left(1 - \frac{\delta}{T_{\text{BL}}}\right) d\delta \end{aligned} \quad (3.7)$$

The expansion of $\textcircled{2}$ and $\textcircled{4}$ gives:

$$\begin{aligned} \textcircled{2} &= G_{\text{step}}(T_{\max}) \\ \textcircled{4} &= \int_{x=0}^{T_{\text{BL}}} dx G(T_{\max} - x) \left[\int_{\delta=0}^{T_{\text{BL}}-x} \mathcal{R}(\delta) d\delta + \int_{\delta=0}^x \mathcal{R}(\delta) d\delta \right] + \\ &+ \int_{x=T_{\text{BL}}}^{T_{\max}} dx G(T_{\max} - x) \int_{\delta=x-T_{\text{BL}}}^x \mathcal{R}(\delta) d\delta \end{aligned} \quad (3.8)$$

Substituting Eq. 3.7 and Eq. 3.8 into Eq. 3.6 an analytical expression for the overall energy resolution can be obtained for any shaping filter given its $G(t)$ (and thus G_{step}) and noise spectral density, given $\mathcal{R}(t)$.

For the case of a charge preamplifier output with preamplifier decay time τ_{pre} (§1.2.4) the autocorrelation function can be obtained

from Eq. 1.3 using the Wiener-Khinchin theorem [16] and taking into account that the sampling system is limited towards high frequencies by the Nyquist frequency of the system $f_N = f_S/2$.³ An approximated expression of $\mathcal{R}(t)$ is the following:

$$\mathcal{R}(t) = \frac{1}{4}a\tau_{\text{pre}} \exp\left[-\frac{|t|}{\tau_{\text{pre}}}\right] + b\frac{f_S}{2}\delta(t) \quad (3.9)$$

A full computation of Eq. 3.6 using this correlation function is presented later, while an useful insight into Eq. 3.6 can be directly gained by further approximating Eq. 3.9 as $\mathcal{R}(t) \simeq A + B\delta(t)$, valid for $t \ll \tau_{\text{pre}}$. With this simplistic autocorrelation function, Eq. 3.6 can be easily computed as:

$$\begin{aligned} \sigma_{\text{full}}^2(T_{\text{max}}) &= G_{\text{step}}^2(T_{\text{max}})A + (\dots)B + && \text{from } \textcircled{1} \\ &+ G_{\text{step}}^2(T_{\text{max}})A - 2G_{\text{step}}^2(T_{\text{max}})A + (\dots)B = && \text{from } \textcircled{2}, \textcircled{3}, \textcircled{4} \\ &= (\dots)B \end{aligned} \quad (3.10)$$

The A terms do cancel out, while the B -related terms (not reported here for brevity) do not. Recalling the fact that the $\textcircled{2}, \textcircled{3}, \textcircled{4}$ terms are introduced by the baseline subtraction algorithm, Eq. 3.10 shows that, in the adopted approximation, the main effect of the baseline subtraction is to fully remove the low-frequency noise component as expected from the anticipated qualitative discussion. These results, though obtained in a simplifying hypothesis, demonstrate the need for baseline subtraction when an event-based system is used.

The general features of Eq. 3.6 are expected to be quite independent of the used shaping filter (as long as “standard” filters are used), although the quantitative details may depend on the particular filter choice. As an example, in Fig. 3.7 an exact computation⁴ of Eq. 3.6 is presented. The results for a typical high-resolution experimental setup are shown as a function of the baseline time T_{BL} for a “standard” shaping method (i.e. no baseline subtraction) and for a baseline subtracted shaping.

The achieved improvement of the baseline-subtracted results over the non-subtracted ones is evident. The main effect of the baseline

³ The digitizer contribution to the noise can be included into the white-noise b term, as discussed in §2.4.3. More details are presented in §3.3.3.

⁴The data presented in Fig. 3.7 have been obtained using a detector-preamplifier configuration similar to the ones used in the next section (typical of high-resolution measurements with germanium detectors), using a standard semigaussian shaping (namely $CR-RC^4$ with a $3 \mu\text{s}$ shaping time, $T_{\text{max}} = 4\tau_{\text{sha}} + T_{\text{BL}}$). The contribution from the AD converter can be easily included in the b term. More details are presented in the next section, taking into account the AD converter noise.

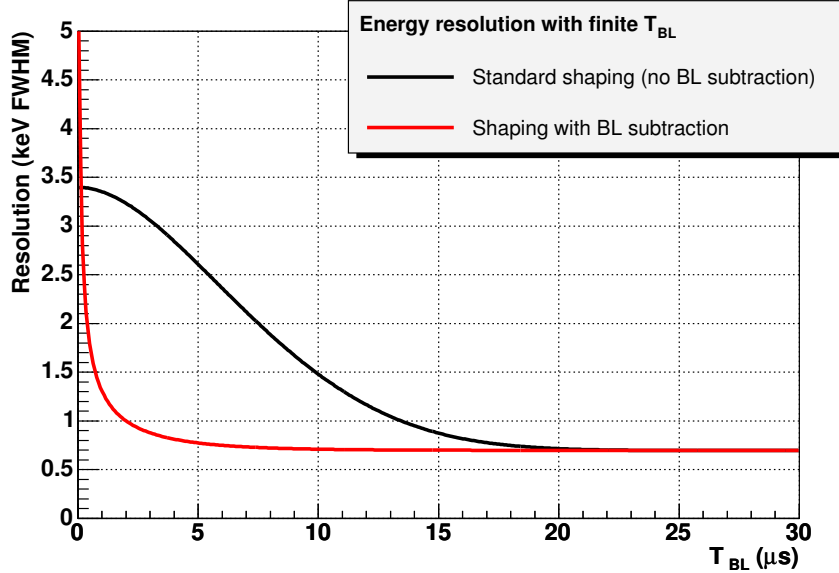


Figure 3.7: Exact computation of Eq. 3.6 using finite T_{BL} , standard semigaussian shaping and realistic noise characteristics (see text). The baseline subtraction method significantly improves the attainable energy resolution.

subtraction is thus an important reduction (or full elimination as in Eq. 3.10) of low-frequency noise components that cannot be properly handled by the shaping filter when the baseline time T_{BL} is too short compared to the filter settling time (that is $12 \mu s$ for the filter used in Fig. 3.7). This conclusion can be extended also to those cases where, due to experimental interferences (like a 50 Hz pick-up), the spectral noise density of the detector-preamplifier system is not given by a simple expression as Eq. 1.3.

From the figure it is apparent that an event-based system, once signal shaping includes a baseline subtraction evaluated over $T_{BL} \sim 2\tau_{sha}$ (about $6 \mu s$ in Fig. 3.7), is able to reach almost the same energy resolution of its continuously running counterpart.

For low T_{BL} values ($T_{BL} \lesssim 1 \mu s$ in Fig. 3.7) the baseline-subtracted results exhibit a $\sigma^2 \propto 1/T_{BL}$ behaviour, i.e. the standard expression that is obtained by averaging a white sequence of samples over a time T_{BL} . In these cases the resolution is dominated by the white-noise component, given the nearly perfect subtraction of the low-frequency noise. Finally, for very low values of T_{BL} ($T_{BL} \lesssim 0.1 \mu s$ in Fig. 3.7), the $1/T_{BL}$ white contribution becomes so large that the

baseline subtraction method is no longer the best choice (although other experimental noise sources like pick-up or interferences are not considered in the figure).

3.3.3 Energy measurements with digital shaping

As already discussed in the previous section and §2.4.3, the sampling process introduces, owing to the quantization and to a possibly finite T_{BL} , additional noise contributions with respect to the intrinsic noise of the detector output. In this section an evaluation of these contributions is carried out, focusing on the general case of finite available baseline time T_{BL} , i.e. event-based systems. The special (important) case of continuously running systems can be simply obtained using $T_{BL} \rightarrow \infty$ in the following formulas.

In §1.2.7 the achievable resolution using a perfect noiseless shaping of the noisy output of a charge preamplifier has been shown. In particular the following result has been obtained (Eq. 1.5, using the hypothesis of a large τ_{pre} time):

$$\sigma_{sha}^2 = \frac{1}{\gamma^2} \left(\alpha a \tau_{sha} + \frac{\beta b}{\tau_{sha}} \right) \quad (3.11)$$

where α , β and γ are numerical constants (Tab. 1.2), and τ_{sha} is the filter shaping time. The quantity a gives the non-white contribution to the total spectral noise density, whereas b refers to the white-components.

In §2.4.3 it has been shown that, under realistic hypotheses, the effect of the sampling process can be schematized as an additional white-noise source with a spectral density $w(\omega)$ given by Eq. 2.13. With this assumption, the effect of sampling noise to the final $\sigma_{dig,sha}^2$ can be easily included⁵ in Eq. 3.11 using an effective white noise given by:

$$b' = b + \frac{R^2}{12} \left[\frac{1}{4^{ENOB}} + \frac{1}{4^B} \right] \frac{2}{f_S} \quad (3.12)$$

From Eq. 3.12 it is easily seen that, neglecting for a while the baseline contribution, the final resolution of the digital system can be practically as good as the one obtained with analog systems as long as the additional white-noise density is much smaller than the one present at

⁵In this case the total output variance of the filter should be computed with an integral like Eq. 1.4 but limited to an upper frequency $f_{max} = f_S/2$. The effect of this correction is of the order of $\sim (f_{max}\tau_{sha})^{-7}$ and thus negligible. The effect of sampling can then be properly approximated in this case as as non-bandlimited white-noise.

the preamplifier output. The key parameters to obtain this result are the effective number of bits or (although with smaller influence) the sampling frequency f_s of the converter.

The effect of baseline subtraction can be included using the formalism developed in §3.3.2, and in particular using Eq. 3.6, substituting the b term with the “effective” white-noise component b' of Eq. 3.12.

It is thus possible to carry on the computation for the overall resolution for any given digital shaping filter. The example of a semigaussian CR-RC⁴ filter (that is a popular configuration in analog spectroscopy amplifiers, apart from the use of active filters) will be considered. The response G_{step} of this filter type to a step input has already been presented in Tab. 1.2. Although the evaluation of Eq. 3.6 has been carried out analytically, the final result is somewhat cumbersome and it is not reported here. It has to be noted that, if the contribution to the overall resolution coming from the digital sampling system is small (i.e. $b' \simeq b$ and $T_{\text{BL}} \rightarrow \infty$) the digital shaping resolution approaches the shaping value used in analog measurements (Eq. 1.6), as expected.

In order to check the correctness of the approach followed for obtaining Eq. 3.6 and Eq. 3.12 a realistic numerical simulation has been implemented. The detector-preamplifier system is characterized by its simulated performances under a noiseless analog shaping, that is a resolution of $\sigma_{\text{sha,} \text{opt}}^2 = 0.7 \text{ keV}$ using an optimal shaping time $\tau_{\text{sha}}^{\text{opt}} = 3 \mu\text{s}$. The detection system used in the simulation is thus a typical configuration for high-resolution γ ray experiments, for example using germanium detectors. Using Eq. 1.6 and Eq. 1.7 these two values allow the determination of the quantities a and b for the detector-preamplifier system and thus its spectral noise density. Signals have been simulated with the proper noise contribution, digitized and processed by a simulated digital system running at 100 MSamples/s sampling speed, using a baseline subtraction algorithm followed by digital CR-RC⁴ shaping.

The used digital shaping time $\tau_{\text{sha}} = 3 \mu\text{s}$ is not the optimal choice for the digital system (taking into account both $b' \neq b$ and the presence of a finite T_{BL}); however the energy resolution difference between the optimal and the non-optimal shaping is expected to be small and thus it has been neglected.

A full range $R = 10 \text{ MeV}$ has been used (compatible with the requirements of γ ray experiments like [18, 19]). About 1000 events have been used for determining the simulated energy resolutions.

In Fig. 3.8 and Fig. 3.9 the simulation results are compared with the predictions of Eq. 3.6 for $T_{\text{BL}}=1$ and $4 \mu\text{s}$ respectively, whereas Fig. 3.10 refers to the case of infinite baseline time. In each figure the points marked with ■ represent the simulation results, whereas the prediction of Eq. 3.6 is shown as a continuous curve. The digi-

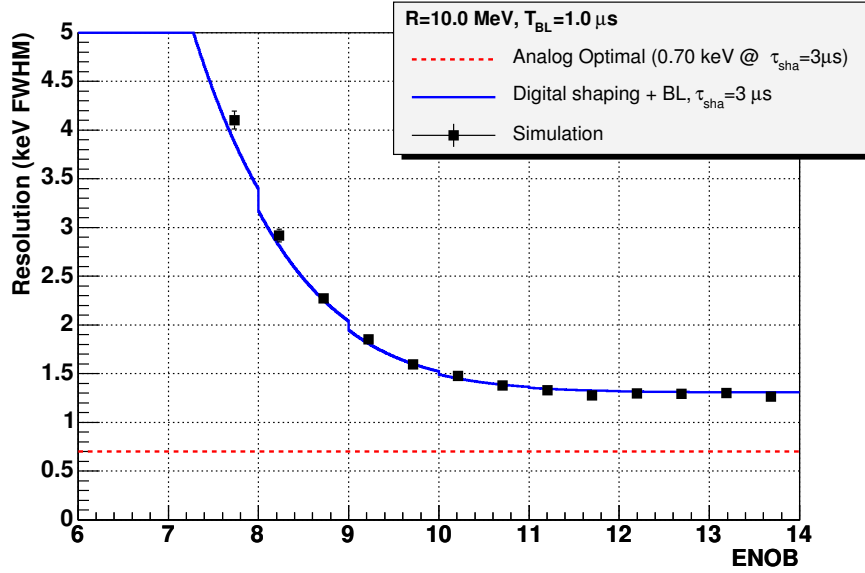


Figure 3.8: Digital energy resolution as a function of the effective number of bits of the converter, using a baseline time $T_{\text{BL}}=1\ \mu\text{s}$. A comparison between the detailed simulation presented in the text and the prediction of Eq. 3.6 (continuous curve) is included.

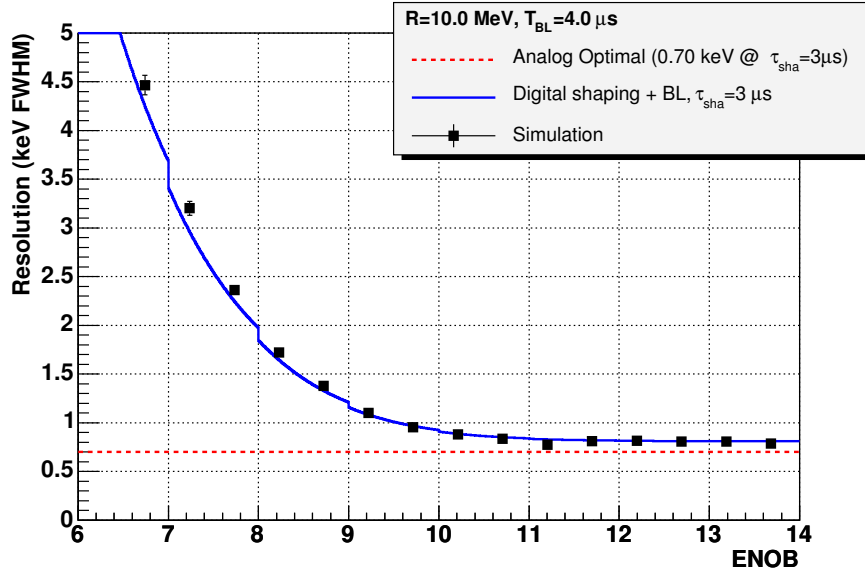


Figure 3.9: Same as Fig. 3.8, but using a baseline time $T_{\text{BL}}=4\ \mu\text{s}$.

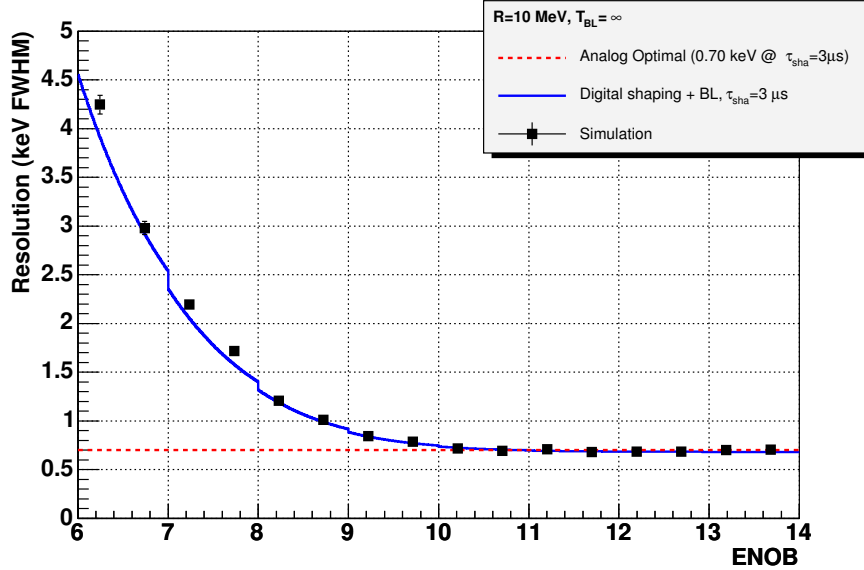


Figure 3.10: Same as Fig. 3.8, but using an infinite baseline time T_{BL} .

Digital shaping energy resolution is shown as a function of the effective number of bits (ENOBI) of the converter. The staircase-like behaviour seen in the figures is associated to the integer number of “physical” bits B (chosen as $\text{int}(\text{ENOBI})+2$, i.e. $B = 12$ for ENOB = 10.3).

From the figures it is evident a good agreement between the simulated points and the analytical expression of Eq. 3.6 for the explored range of converter resolutions and T_{BL} times. There is an appreciable discrepancy at low values of ENOB, where the simulated points are characterized by a worse resolution than the predicted one. In §2.4.3 it has been shown that the hypotheses used for the evaluation of the sampling noise are accurate only when the quantization noise is smaller than the noise characterizing the ADC analog input. For low ENOB values this assumption is no longer valid (no dithering [29] occurs) and thus a discrepancy with respect to the predicted value is indeed observed in the expected direction.

From the presented results it is possible to recognize that (in the used realistic example) the achievable digital resolution is almost saturated using an AD converter having 11–12 effective bits (if a sampling period of 100 MSamples/s is used). Depending on the experimental requirements, an event-based digital system with a short baseline time $T_{BL} = 1 \mu s$ can be used to obtain a resolution about two times worse than the best theoretically attainable one, whereas at least $T_{BL} = 4 \mu s$

must be used if a resolution within 15% of the analog one is needed (0.8 keV with respect to 0.7 keV in Fig. 3.9). For maximum resolution a very long baseline time is needed, and thus a continuously running digital system would be the option of choice.

This section has been devoted to the study of the achievable energy resolution due to electronic noise only. It has to be noted that the detection physics for a typical germanium detector (mainly statistical fluctuations in carrier number, but also trapping effects, ...) gives a contribution of about $\sigma_{\text{detector}} \simeq 1.4$ keV for an incident γ energy of 1 MeV ($\sigma_{\text{detector}}^2$ decreases linearly with the γ energy). This means that the detailed study presented is important only in those cases where low-energy high-resolution measurements are of paramount importance.

3.3.4 Signal Integration

For many relatively low-resolution detectors (for example organic or inorganic scintillators) the maximum achievable energy resolution is largely dominated by the physics of the detection process, as for example the fluctuations in the number of information carriers (in this example fluorescence photons). For these cases the electronic resolution gives a negligible contribution to the final energy resolution and thus simple (and fast) algorithms like signal integration can be applied without any significant degradation of the detector performances.

As an example, in Fig. 3.11 the output of a CsI(Tl) scintillator detector is shown.⁶ The energy information can be recovered by integration of the whole pulse (after having subtracted the signal baseline, see §3.3.2):

$$E \propto \int_{t_{\min}}^{t_{\max}} S(t) dt \quad (3.13)$$

The application of Eq. 3.13 to a sequence $S[k]$ of sampled data is straightforward as long as the integration limits are integer multiple of the sampling period τ_{clk} , i.e. $t_{\min} = k_{\min}\tau_{\text{clk}}$ and $t_{\max} = k_{\max}\tau_{\text{clk}}$:⁷

$$E \propto \sum_{k=k_{\min}}^{k_{\max}} S[k] \quad (3.14)$$

As it will be discussed in §4.11, for pulse shape analysis it is often

⁶A high-energy signal was assumed so that the single photoelectron contribution cannot be appreciated in the figure.

⁷The equivalence between Eq. 3.13 and Eq. 3.14 is exact for simple interpolating methods as linear, cubic and “penta” (see §3.4.1) when $S[k] = 0$ at the beginning and at the end of the sequence. For the $\sin(x)/x$ interpolation a small correction factor should be considered, but it is negligible in all practical cases.

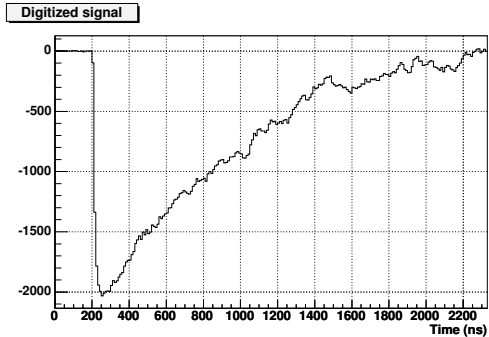


Figure 3.11: Example of a CsI(Tl) scintillator signal. The energy information can be recovered by integration of the whole pulse.

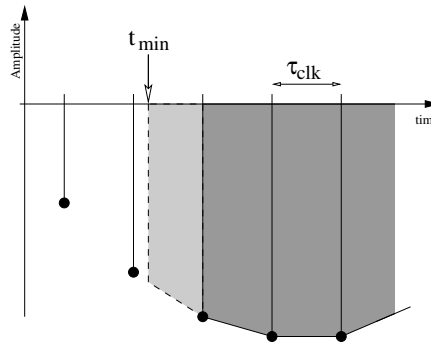


Figure 3.12: Example of a signal integration with non-integer boundary points. A simple interpolation can be used.

desirable not to integrate the whole pulse, but only a subset of it, possibly with a starting time experimentally extracted from the signal itself. Thus the case of non-integer integration limits is experimentally relevant. In Fig. 3.12 a simple solution is depicted for the case of non-integral t_{\min} : a simple linear interpolation between samples has been employed, reducing the integral to a trapezoid integration (this method is described in [1, 2]). Depending on the needed resolution, the method can be simply extended by using more sophisticated interpolation methods (some of them are discussed in §3.4.1).

Using the results of §3.3.2 and arguments similar to the ones discussed in §3.3.3, it is possible to evaluate the expected variance in the computation of the signal integral. In practice this derivation has not been carried out, because the detailed optimization of the electronic noise of this method is not relevant when comparing the electronic resolution with the much larger detector noise (mainly due to the specific detection processes of the used detector).

Some experimental results obtained applying this method to a non-standard detector configuration are presented in §4.11.

3.3.5 Digital replica of a spectroscopy amplifier

In §2.4.4 the main general properties of digital filters have been discussed. From the theory it is known that a digital filter can mimic any linear analog system, although for many applications we are interested in the general features (noise, bandwidth, ...) of the filter and not in the fine details of its response. In this subsection an exception to this

rule is presented.

The GARFIELD apparatus [40] uses CsI(Tl) detectors (see §1.2.2 and §4.2) for detection of light charged particles. The total light output from this scintillator is approximately proportional, for a given impinging particle, to the energy deposited in it. However, a residual significant dependence of the light output from the charge and the mass of the detected particle is also observed (see [44] and the discussion in §4.2). This makes the absolute energy calibration of the detector somewhat complex. Several beams have been dedicated during the last few years to the purpose of energy calibration. Each CsI(Tl) detector was connected to a standard spectroscopy amplifier (CAEN N568); the amplitude of the shaped signals was measured using a standard peak Sensing ADC (analog shaping networks have been introduced in §1.2.7). Thus the energy information is obtained using the maximum of the shaped signal.

As it has been discussed in §3.2, the GARFIELD experiment is planning an upgrade based on digital sampling techniques. It is thus important to be able to transfer the calibration work already done on the “old” data (obtained by analog means) to the “new” one (obtained by digital means). For this purpose it has been necessary to design a digital filter characterized by the following properties:

Replica of the existing analog hardware

In order to have the same response with respect to the analog spectroscopy amplifier (CAEN N568) to the various signal shapes of the CsI(Tl) a digital replica is needed. Not only the general features, but the fine details of the transfer function have to be reproduced, in order to achieve the same response as the analog filter for the various signal shapes.

Fast processing

This filter will be operated by the DSP described in §3.2. Its on-line application will require a fast processing, i.e. a low number of poles and zeros (see §2.4.4). Signal decimation (i.e. reduction of sampling rate [29]) may be used as long as it preserves the needed resolution.

16 bit quantization

This filter will be operated by the DSP described in §3.2 that is a 16 bit fixed point DSP. Thus the filter needs to be robust and stable with respect to a 16 bit quantization of its parameters.

As a first step, the response of the analog filter has been measured by injecting a signal from a pulser and sampling both the input $S(t)$

– thus obtaining a sequence $S[k]$ – and the output $R_{\text{analog}}(t)$ – obtaining $R_{\text{analog}}[k]$ – of the filter. The problem of designing the desired filter can be expressed both in the time or in the frequency domain, selecting which of the two domains will be more accurately reproduced by the final filter. In this application we are mainly interested in the time properties of the signal (the analog chain measures only the peak amplitude of the signal) and thus the filter design has been carried out in the time domain.

The desired filter \mathbb{F} has to minimize the following quantity:

$$\chi_{\mathbb{F}}^2 = \sum_k (R_{\text{analog}}[k] - R_{\mathbb{F}}[k])^2 \quad (3.15)$$

where $R_{\mathbb{F}}[k]$ is the output of the digital filter \mathbb{F} using $S[k]$ as input. The digital filter \mathbb{F} is completely defined by the following parameters:

Number of poles and zeros

A trivial method of increasing the available degrees of freedom in order to obtain a better fit of the filter is the increase of the number of poles and zeros. Apart from stability problems (see [29]), a higher number of poles and zeros requires more computational power in the on-line application and thus it translates in a higher computation time. Thus a compromise between few poles/zeros (for better computational speed) and many poles/zeros (for better reproduction) must be found.

a_h , b_h coefficients

Once the number of poles and zeros has been fixed, the proper coefficients a_h , b_h of Eq. 2.19 for the recursive filter must be determined. Because of the internal precision of the used DSP (16 bit) these coefficients will be truncated, thus altering the location of the original poles and zeros. This means that only a discrete set of poles and zeros is available for the quantized filter.

Gain and time shift

Trivial parameters for matching the experimental data.

The minimization of Eq. 3.15 can be carried out using a standard minimization package such for example MINUIT [45]. It has been verified that, possibly due to the very high sensitivity of the $\chi_{\mathbb{F}}^2$ function to the location of poles and zeros, MINUIT is not able to converge to a satisfying solution for the desired filter parameters. A second minimization package based on a genetic algorithm (differential evolution [46]) has instead proved to be robust in the evaluation of the

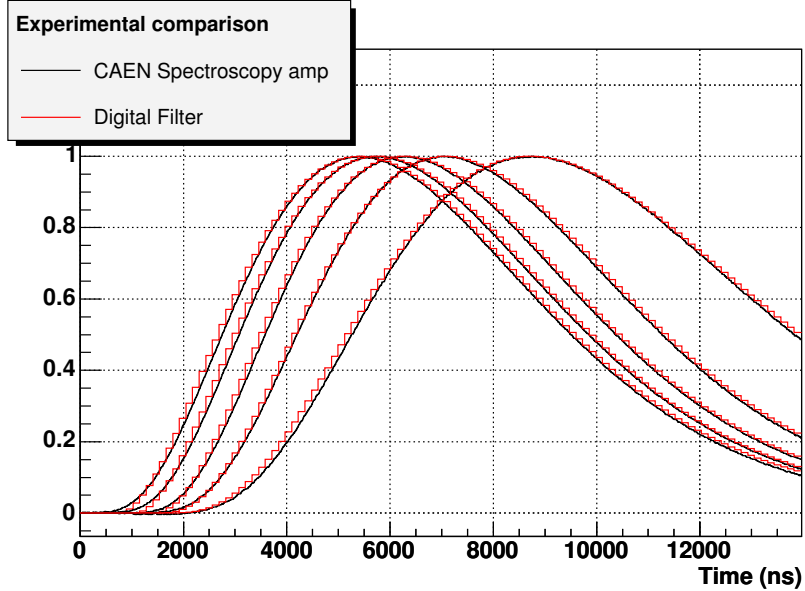


Figure 3.13: Experimental comparison between the output of the CAEN N568 amplifier (with various pulser input signals) and its digital counterpart discussed in the text (a normalization factor has been applied). A good reproduction of the overall signal shape is evident.

parameters.⁸

The final filter uses 2 zeros and 3 poles and signal decimation (the final τ_{clk} is 128 ns) for fast processing speed. An assembler software for the DSP processor has been written [37], taking into account the finite-precision issues present in the DSP processor used.

In Fig. 3.13 an experimental comparison between the analog filter and its digital counterpart is presented. Pulser signals with different risetimes (50, 100, 500, 2000, 5000 ns) have been injected into the analog shaper in order to test its behaviour, and its responses have been sampled. The pulser signal has been acquired too and processed by a DSP with the finally adopted version of the digital filter.

A good reproduction of the desired signal shape is evident largely matching the limited resolution achievable with CsI(Tl) detectors (of the order of few percents).

In the next future this digital filter will be employed in the GARFIELD apparatus and a more systematic comparison with its analog counterpart will be performed.

⁸A slightly modified version of χ^2_F has been used as energy function for the genetic minimization procedure.

3.4 Digital timing measurements

A high-resolution determination of the time properties of a signal produced by a nuclear-physics detector can be used to perform different type of measurements, ranging from coincidence or time of flight measurements to particle identification, as discussed in §1.2.

Given a sampled sequence $S[k]$ (obtained by sampling a continuous signal $S(t)$ with a τ_{clk} sampling period), a general timing measurement can be regarded as the determination of the time t_0 at which the original signal was equal to some level S_0 (possibly not fixed and related to the type of timing method used). Thus a noise-free reconstruction of $S(t)$ from $S[k]$ would allow the solution of the equation $S(t_0) = S_0$ and then the determination of the desired timing information t_0 .

The reconstruction of the original $S(t)$ can be performed using a low noise digitizer coupled to an adequate interpolation procedure between the discrete samples $S[k]$. Both these points influence the final achievable resolution and thus a study (by analytical and numerical means) of these effects has been carried out.

3.4.1 Interpolation noise

The process of obtaining a continuous signal $S(t)$ starting from its sampling $S[k]$ is known as signal interpolation or reconstruction. In §2.4.2 the sampling theorem was introduced (Eq. 2.9). The formula for a perfect reconstruction (under the theorem hypotheses) is:

$$S(t) = \sum_{k=-\infty}^{+\infty} S[k] \cdot \eta(t/\tau_{\text{clk}} - k) \quad (3.16)$$

with $\eta(x) = \text{sinc}(x)$. The continuous function $\eta(x)$ is called interpolation kernel. The Fourier transform of the $\text{sinc}(x)$ function is equal to one for normalized frequencies below 0.5 and zero for the others. It is also characterized by being of infinite time length (i.e. there is no x_0 such that $\forall |x| > x_0 \text{sinc}(x) = 0$). This means that all the samples of an infinite length sequence $S[k]$ are used (with proper weights) to reconstruct the signal $S(t)$. This interpolation kernel is then non-causal, i.e. points before and after the time t are used for interpolation.

It has also to be noted that a perfect interpolation (i.e. the one stated in the Sampling Theorem) is not always needed from an experimental point of view. For example the interpolation of a noisy signal (as the ones we are interested in) can be allowed to deviate from the ideal interpolating kernel as long as the introduced overall noise is well

below the experimental one.

This allows the use of simpler interpolating kernels $\eta(x)$ in Eq. 3.16. For example a finite length kernel ($\eta(x) = 0$ for $|x| > x_0$) truncates the infinite sum of Eq. 3.16 to only $2x_0$ points. This makes it possible to employ fast interpolating procedures to be used in on-line signal processing.

In Fig. 3.14 some simple interpolating kernels are presented, together with their Fourier Transform; as a reference in panels (k) – (l) the $\text{sinc}(x)$ function is reported. Only the non-zero part of each kernel has been shown in the examined time domain.

The simplest interpolating procedure is probably the linear one, Fig. 3.14(a) – (b). It consists of connecting the consecutive samples $S[k]$ with a straight line (that is a polynomial of order 1). More complex interpolations can be obtained by using a higher order polynomial: for example 3th order (panels (c) – (d), cubic interpolation) or 5th order (panels (e) – (f), “penta” interpolation). It is also possible to operate a truncation of the $\text{sinc}(x)$ using a windowing function [29]. Two examples of kernels for 6 and 8 points windowed sinc (6 or 8 points $S[k]$) are needed for the computation of Eq. 3.16) are reported in panels (g) – (h) and (i) – (j).⁹ The main difference between the simple polynomials (first three rows of Fig. 3.14) and the sinc-related kernels is the presence of important high-frequency components beyond the Nyquist frequency. These components can be traced back into the time domain to the presence of sharp cusps with a non-continuous first derivative. Conversely, the roll-off of the polynomial interpolations near the Nyquist frequency is sharper than the sinc-related kernels of the same length.

The interpolating choice for on-line processing will be the simplest kernel (i.e. the shortest) compatible with the desired signal-to-noise ratio. It has also to be noted that the first three kernels of Fig. 3.14 have a very simple analytical expression and thus they are very attractive for on-line computations.

An estimate of the noise introduced by a particular interpolating kernel can be performed considering an ideal noiseless sampling of a given input signal and taking into account the asynchronous sampling performed by the AD converter. The total error on the reconstruction of the input signal at some fixed time t_0 can then be computed and used as an estimate of the interpolating noise.

With reference to Fig. 3.15 we consider an ensemble of different noiseless samplings $S_\delta[k]$ of a noiseless input signal $S(t)$, differing only for the relative phase between the input signal and the sampling comb

⁹A standard Blackman [29] windowing has been used. The overall discussion is not affected by the windowing choice, although the actual performances may vary.

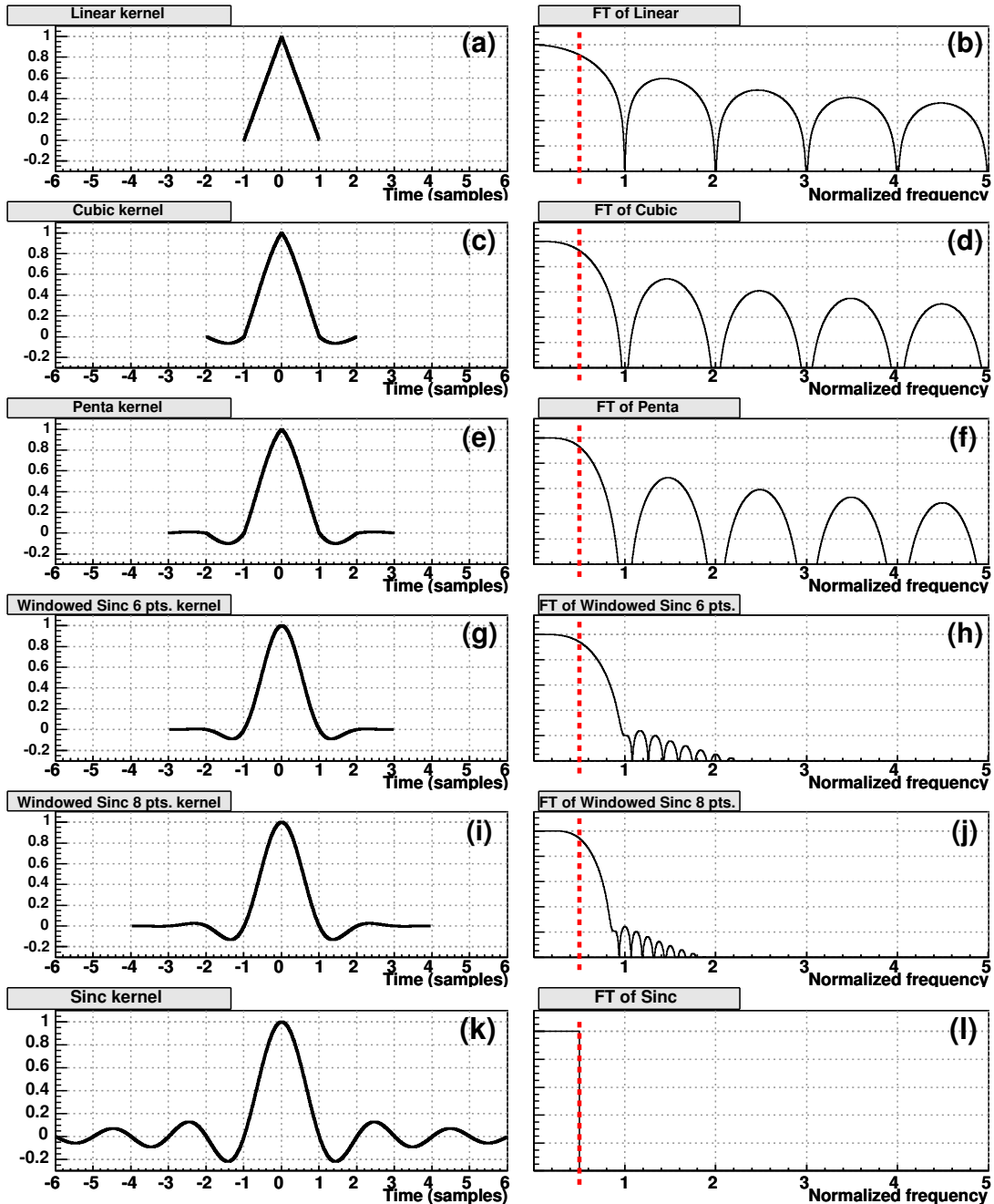


Figure 3.14: Comparison between various interpolating kernels: on the left column the non-zero part of each kernel is plotted, whereas its Fourier transform modulo (with vertical log scale) is reported on the right. Panels: (a) – (b) linear interpolation, (c) – (d) cubic interpolation, (e) – (f) “penta” interpolation, (g) – (h) 6 points windowed sinc, (i) – (j) 8 points windowed sinc, (k) – (l) $\text{sinc}(x)$. See text for details.

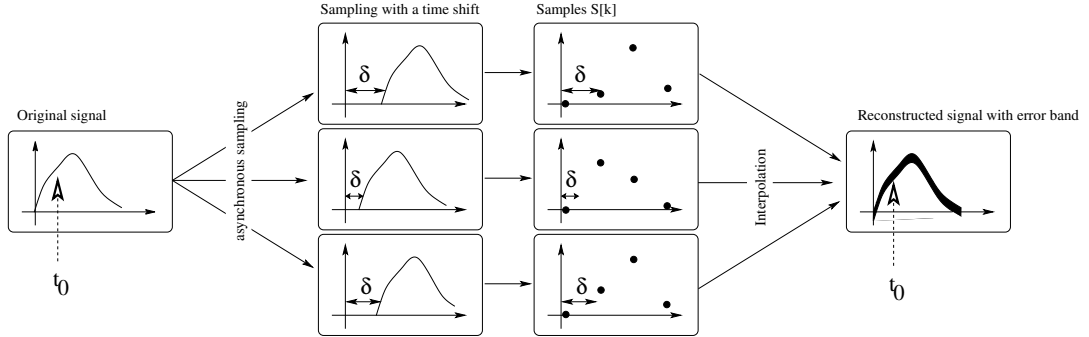


Figure 3.15: Effects of asynchronous sampling and interpolation on signal reconstruction. A continuous signal is sampled with different phases and then reconstructed. See text for details.

(defined in §2.4.2). The phase difference can be expressed as a time delay δ that ranges from 0 to τ_{clk} .¹⁰ For each sampled sequence the original (time shifted) signal can be reconstructed using:

$$S_\delta(t) = \sum_{k=-\infty}^{+\infty} S_\delta[k] \cdot \eta\left(\frac{t}{\tau_{\text{clk}}} - k\right) \quad (3.17)$$

If a perfect interpolation could be achieved, $S(t - \delta) = S_\delta(t)$ should hold. In the adopted noiseless sampling hypotheses $S_\delta[k] = S(k\tau_{\text{clk}} - \delta)$.

The variance on the reconstructed $S_{0,\delta} = S_\delta(t_0 + \delta)$ with respect to the true value $S_0 = S(t_0)$ over the considered ensemble can then be computed as:

$$\begin{aligned} \sigma^2 &= \frac{1}{\tau_{\text{clk}}} \int_0^{\tau_{\text{clk}}} \left[S_0 - S_\delta(t_0 + \delta) \right]^2 d\delta \\ &= \frac{1}{\tau_{\text{clk}}} \int_0^{\tau_{\text{clk}}} \left[S_0 - \sum_{k=-\infty}^{+\infty} S(k\tau_{\text{clk}} - \delta) \cdot \eta\left(\frac{t_0 + \delta}{\tau_{\text{clk}}} - k\right) \right]^2 d\delta \end{aligned} \quad (3.18)$$

Equation 3.18 gives a simple method to estimate the interpolation “quality” of a given interpolating kernel $\eta(x)$. For a given function $S(t)$ and desired time t_0 the signal-to-noise ratio obtained using Eq. 3.18 can be compared with the experimental SNR, that is a combination of the AD noise (mainly due to finite effective number of bits) and detector noise.

¹⁰The notation can be simplified using an adimensional time variable t/τ_{clk} . This more general approach has been used for the axes labeled with “samples” in Fig. 3.16 and Fig. 3.19. An explicit τ_{clk} dependence has been retained in the discussion for a clearer presentation.

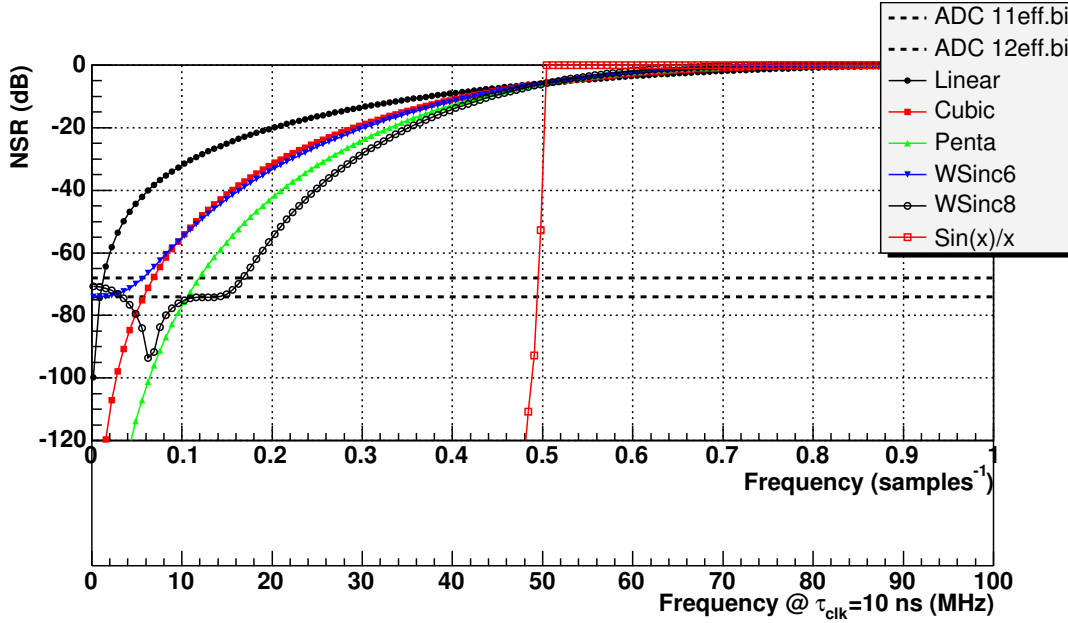


Figure 3.16: Interpolation error (estimated using Eq. 3.18) for various interpolation kernels using the bandlimited function of Fig. 3.17. See text for details.

As an example of application of Eq. 3.18 in Fig. 3.16 the results for various interpolating kernels using $S(t) = \sin(2\pi ft)$ (shown in Fig. 3.17) are presented. On the vertical axis the noise-to-signal-ratio (NSR) is reported (in decibels) as computed with Eq. 3.18. On the horizontal axes the signal frequency f is reported, both in physical units (assuming a $\tau_{\text{clk}}=10$ ns) and in adimensional units (this is a more general description that allows the application of these results to any AD converter). As reference points, the theoretical NSR of 11 and 12 effective-bits AD converters are shown.

The chosen $S(t)$ is a perfect bandlimited signal and thus the sampling theorem (§2.4.2) ensures a perfect reconstruction using a kernel $\eta(x) = \text{sinc}(x)$, as long as its input frequency is below $1/2 \cdot f_S$. This is indeed¹¹ the behaviour seen in Fig. 3.16, where the SNR for the sinc kernel is very good for $f < 0.5 \text{ samples}^{-1}$. The various interpolating kernels have different performances depending on the kernel length: as a general rule, the longer the interpolation kernel the better the achieved performance (usually at the cost of more processing time).

It is interesting also to compare the performances of the “penta”

¹¹The deviation seen in Fig. 3.16 for the sinc interpolation kernel from the ideal behaviour for $0.48 < f < 0.5$ is due to the finite precision (24 bit mantissa) of the program used for the computation of Eq. 3.18.

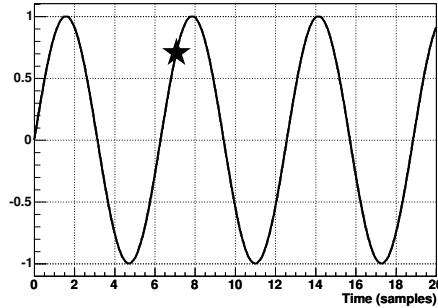


Figure 3.17: Function $S(t)$ used for the computation shown in Fig. 3.16. The star \star indicates the point used for the evaluation of Eq. 3.18.

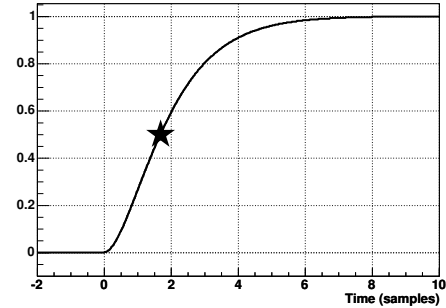


Figure 3.18: Function $S(t)$ used for the computation shown in Fig. 3.19. The star \star indicates the point used for the evaluation of Eq. 3.18.

interpolation (5^{th} order polynomial) and of the 6 points windowed sinc, both having the same kernel length. The polynomial interpolation, which has a natural representation in the time domain, is superior in this time-domain comparison to the windowed sinc one (optimized for performance in the frequency domain). The opposite is true in applications where a frequency related comparison is of interest (for example harmonic distortion in a periodic signal). It is also interesting to note that the performance of the windowed sinc interpolations is limited in the low-frequency part of Fig. 3.16 due to residual Gibbs [29] effects.

A more interesting example from the experimental point of view of an application of Eq. 3.18 is shown in Fig. 3.19, where the case of the function $S(t)$ shown in Fig. 3.18 is presented.¹² This function can be regarded as an oversimplified model for the output of a charge preamplifier. It is a non-bandlimited function that resembles the conditions met in experimental measurements. The 10–90% risetime of the signal is reported on the horizontal axes of Fig. 3.19, both in physical (with $\tau_{\text{clk}}=10$ ns) and in adimensional units. As reference points, the theoretical NSR of 11 and 12 effective-bits AD converters are shown, together with the SNR obtained in an experimental test using the AD converter of §3.1 connected to a silicon detector (this experiment is

¹²The analytical expression used for $S(t)$ is the convolution between $f(t) = 1 - \exp(-t/\tau)$ and $g(t) = 1/\tau \cdot \exp(-t/\tau)$ with τ as time constant. This should roughly describe the response of a finite-risetime charge preamplifier with a finite-width signal as input.

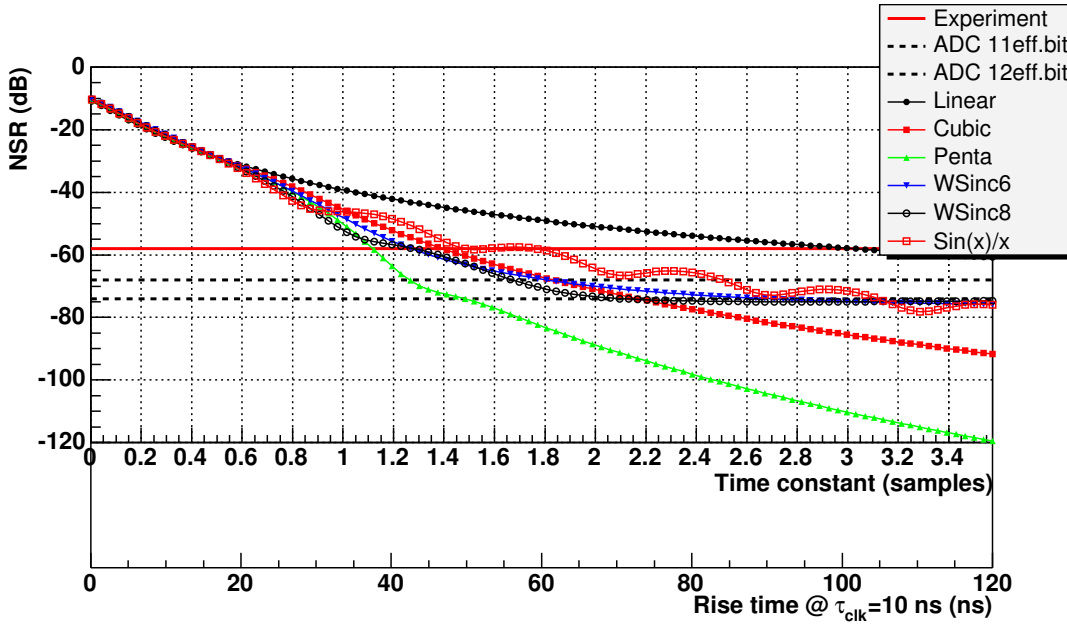


Figure 3.19: Interpolation error (estimated using Eq. 3.18) for various interpolation kernels using the non-bandlimited function of Fig. 3.18. See text for details.

described in §4.3). The goal is to obtain an interpolation noise lower than the experimental SNR in the risetime interval observed in the experimental test (50–70 ns).

It is evident from the figure that (in the risetime region of interest) a significant performance difference exists between the linear interpolation and the other interpolation kernels. In particular, the interpolation noise arising from the linear interpolation does not meet the requirement of being lower than the experimentally observed noise. It has also to be noted that, apart from the linear kernel, the performances of all the used kernels in Fig. 3.19 are very close to each other and satisfy the NSR requirement. In these operating conditions, the interpolation of choice in an on-line signal-processing system would be the cubic one, due to its short length (4 samples $S[k]$ are required to produce $S(t)$) and its simple analytical form, as opposed to the windowed sinc kernels. For an example of application that uses the analytical formulation available for this kernel see §3.4.2.

It is interesting to note that the performances of the infinite kernel $\text{sinc}(x)$ (and also of the windowed sinc ones) are far from perfect in Fig. 3.19, as compared to the results of Fig. 3.16. This result is not in contradiction with the sampling theorem, because the input signal $S(t)$ used in Fig. 3.19 is non-bandlimited (i.e. f_N cannot be

defined). Strictly speaking the sampling theorem cannot be applied in this case, and thus a perfect reconstruction of the signal cannot be mathematically achieved using $\text{sinc}(x)$. The sinc -derived interpolations force the reconstructed signal to have no components above Nyquist (or very small), thus deviating from the original signal behaviour (non-bandlimited). This can explain the result of slightly better performances using polynomial interpolations (with significant over Nyquist components, see Fig. 3.14) instead of the sinc -derived ones.

From the presented discussion of Eq. 3.18 it is possible to recognize that the choice of a proper digital data-interpolation procedure is a compromise between the needed performances (low interpolation-noise) and needed processing time (a more complex kernel requires more processing power). This choice is thus strongly related to the specific experimental noise and detector type, and this point must be carefully addressed in each experimental test, although, from Fig. 3.19, the cubic interpolation can be regarded as a good first choice for a general purpose on-line analysis.

In the following discussions and in the experimental results presented in Chap. 4 a cubic interpolation has been used, unless otherwise stated.

3.4.2 ADC parameters influencing timing resolution

In order to take into account the main ADC parameters influencing the timing resolution (beyond the choice of the interpolation) a specific digital timing algorithm will be considered (digital Constant Fraction Discriminator, dCFD, presented also in [5]), although the main obtained results are valid and can be extended to other timing algorithms.

The dCFD algorithm is meant to define the instant t_{dCFD} at which the signal reaches a predetermined fraction f of its full amplitude. A simple estimate of the time-mark resolution achievable with this approach can be given in the basic hypothesis that the time needed for the signal to pass from its zero value to full amplitude (in practice the 10%–90% risetime of the signal, briefly risetime t_r in the following) contains few sampling periods τ_{clk} . The case of a charge preamplifier input signal (see Fig. 3.5) will be explicitly considered.

The dCFD algorithm proceeds as follows (see Fig. 3.5):

1. Determine the asymptotic amplitude A of the signal, for example with a simple average of the samples at time $T \gg t_r$, after a baseline subtraction (§3.3.2).
2. Find the two consecutive samples with amplitudes α_1 and α_2 such

that $\alpha_1 < f \cdot A < \alpha_2$.

3. Obtain t_{dCFD} with an interpolation between (t_1, α_1) and (t_2, α_2) (note: $t_2 - t_1 = \tau_{\text{clk}}$).

Following this procedure, the contribution to the time resolution due to this approach (i.e. the error σ_{dCFD} on t_{dCFD}) can be estimated as:

$$\begin{aligned}\sigma_{\text{dCFD}} &\leq \sigma_{e+q} \left[\left| \frac{dS}{dt} \right|_{t_{\text{dCFD}}} \right]^{-1} \\ \sigma_{e+q}^2 &= \sigma_e^2 + \frac{R^2}{12 \cdot 4^{\text{ENOB}}}\end{aligned}\quad (3.19)$$

where σ_e^2 is the variance associated with the electronic noise of the preamplifier. As in §2.4.3, the quantization error has been considered using the ADC effective number of bits, and neglecting the contribution from the “physical” number of bits. The error on A has been neglected, because it can be sufficiently reduced by using a proper algorithm (for example averaging over a large number of samples), as well as the error on τ_{clk} (this error amounts to less than few ps with a proper electronic design).

The equality sign in Eq. 3.19 holds in the limiting case of a value $f \cdot A$ coinciding with one of the two samples or when the two amplitude determinations α_1 and α_2 are fully correlated; in the opposite case of total independence of errors, the minimum value of the left member is obtained when $f \cdot A = (\alpha_1 + \alpha_2) / 2$.

It is interesting to compare Eq. 3.19 with the nominal resolution attainable with a state of the art analog timing device, namely with an analog CFD [23] treatment of the signal (assuming the same noise bandwidth). The analog CFD resolution is given by an expression identical to Eq. 3.19, except for an equal sign, for the absence of the quantization error and for an additional factor $\sqrt{1 + f^2}$ coming from the signal treatment performed in the CFD electronic module. It is worth stressing that, if the quantization error is significantly lower than the electronic noise, i.e. if the effective number of bits is sufficiently high to keep the electronic noise of the signal as the dominant effect in the amplitude determination, a dCFD time resolution better or equal to that attainable with an analog CFD module can be achieved.

This result actually means that the timing resolution can be much smaller than the sampling period τ_{clk} of the converter, the key issue for dCFD resolution being the number of effective bits necessary to confine the quantization error below the electronic noise of the signal. The sampling period τ_{clk} must be sufficiently short to allow the

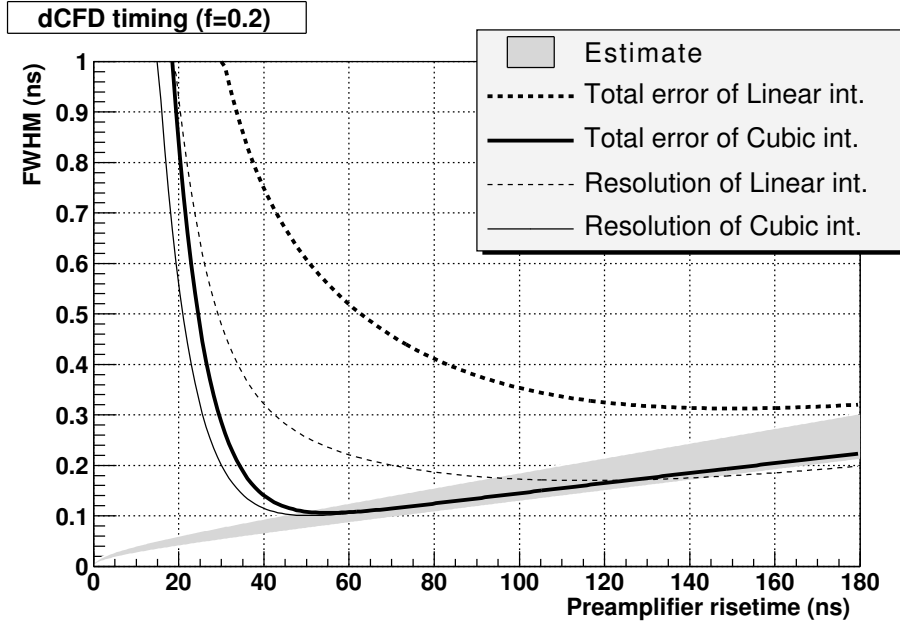


Figure 3.20: Total error on digital Constant Fraction timing ($f = 0.2$) as a function of the preamplifier risetime, obtained with a 12 bit resolution 100 MSamples/s digitizer, using linear interpolation (thick dashed line) and cubic interpolation (thick full line).

presence of some samples during the risetime of the signal.

In order to estimate the overall performances quantitatively, a simulation has been implemented and its results presented as a function of the risetime of the preamplifier (assuming a fixed shape input signal). While usually in PSA applications (some examples presented in Chap. 4) two or more fraction values are used to estimate the risetime of the signal, the simulations have been run with a representative value $f = 0.2$. A realistic preamplifier output has been considered, whereas the electronic noise at the preamplifier output has been assumed to have the same amplitude and spectral density that have been measured in an experimental test (see §4.3). The electronic noise has been changed following the preamplifier risetime t_r , namely the associated full variance increases with the transmitted bandwidth as $\sigma_e^2 \propto 1/t_r$. The digitizer has been assumed to have a 12 bit resolution (10.8 effective) and sampling rate of 100 MSamples/s, with a sharp antialiasing filter cutting at the frequency of 50 MHz.

The results are reported in Fig. 3.20. The shaded region represents the limits determined by Eq. 3.19 for $f = 0.2$ and a signal amplitude of half range ($A = 0.5R$). The thick dashed line represents the absolute

error (systematic and statistical) with respect to the true value once t_{dCFD} is determined with a linear interpolation. Apart from the expected rapid increase of the error at shorter risetimes, due to the insufficient number of interpolating points, a significant increase of the error with respect to the estimate of Eq. 3.19 is apparent, even in regions where lacking of interpolating samples can be excluded.

A cubic interpolation procedure (as discussed in §3.4.1) has thus been tested. An application to the present case, suitable for on-line signal processing, proceeds as follows (using the adimensional time variable $x = \text{time}/\tau_{clk}$):

- A time mark $x_{dCFD,\text{linear}}$ is obtained with the procedure previously outlined
- Four adjacent samples x_1, x_2, x_3 and x_4 are chosen, with the condition $x_2 < x_{dCFD,\text{linear}} < x_3$, and the unique third order polynomial $y(x - x_2)$ through them is computed.
- The time x_{dCFD} is obtained solving the equation $y(x - x_2) = f \cdot A$. Numerically this can be done using a successive approximation method (for example the Newton's one) with $x_{dCFD,\text{linear}}$ as initial guess. It was verified that, with realistic signals, the iterative solution of this equation converges very fast and thus in many cases the iterative loop can be replaced with a single correction, thus coinciding with a first order approximation of $y(x - x_2)$ around the point $x_{dCFD,\text{linear}}$ (the next approximation step typically introduces a correction smaller than $10 - 20$ ps).

The presented method is well suited for on-line processing of data with DSPs, because the computation of the correction involves about 15 multiply-accumulate (MAC) operations to obtain the coefficients of the polynomial, and 10 – 20 additional operations to obtain the desired correction.

Much of the simplicity of the method derives from the analytical expression available for the cubic interpolation kernel. The use of, for example, a sinc-derived kernel would require a numerical tabulation, a numerical convolution and a binary search to obtain a similar result.

The thick full line in Fig. 3.20 represents the results obtained by performing the described cubic interpolation. The improvement with respect to the first-order linear interpolation is apparent and the data fall in the shaded region, as expected having significantly reduced the additional contribution coming from the interpolation noise (discussed in §3.4.1 and not included in Eq. 3.19).

The quantities reported in Fig. 3.20 and already discussed refer to the total absolute error with respect to the true value. When the

timing information is used for discrimination purposes (like for PSA, see Chap. 4) only the fluctuations with respect to the mean observed value are of interest. The thin full and dashed curves in Fig. 3.20 represent indeed these resolutions (for $f = 0.2$) for cubic and linear interpolations, respectively. It has been verified that, while the details of the basic signal shape may influence the behaviour of the curves in the region of the steep increase of the total absolute error towards short risetimes, the conclusions that can be drawn from Fig. 3.20 about the quality of dCFD timing with a 100 MSamples/s-12 bit digitizer are quite general.

It is worth noting that the predicted timing resolution for this AD converter having $\tau_{\text{clk}}=10$ ns is ~ 100 ps FWHM, two orders of magnitude smaller than the sampling period. This remarkable result has been experimentally confirmed, see §4.3.

To better pin down the digitizer characteristics which indeed determine the timing quality attainable with digital Constant Fraction Discrimination, further simulations similar to those presented in Fig. 3.20 have been run for digitizers with different characteristics. The total absolute time mark errors are shown in Fig. 3.21, together with the results simulated for an ideal analog CFD timing. The considered digitizers, apart from the one described in §3.1 (100 MSamples/s-10.8 effective bit), are a 100 MSamples/s-12 eff. bit, 1 GSample/s-8 eff. bit, 2 GSamples/s-8 eff. bit and a 400 MSamples/s-12 eff. bit converter. In the simulation the signals are processed by the digitizers, each having a perfect antialiasing filter cutting at the corresponding Nyquist frequency. The risetime of the preamplifier, as well as the corresponding noise, has been varied as already discussed. Figure 3.21 confirms that, apart from the very fast risetime region, the key feature for determining the timing quality is the digitizer number of effective bits. It is worth noting that both the 12-bit digitizers give timing performances equivalent to the standard analog CFD timing, while for the faster ADCs the increased sampling rate cannot compensate for the poorer bit resolution. Finally, for the 100 MSamples/s-12 bit digitizer the dotted line reports the contribution to the absolute error due to the quantization effects (including effective bits) and actually this represents the ultimate resolution attainable with this converter in the non-realistic hypothesis of a noiseless preamplifier output.

In the special case of very fast AD converters a standard oversampling technique [47] may be applied to increase the overall bit resolution: the signal is sampled by the ADC at a much higher rate f_s than the required Nyquist frequency f_N . Averaging over the collected data allows an increase of the resolution of the system by a factor $\sqrt{f_s/(2f_N)}$. For example, the oversampling of a signal with an 8 ef-

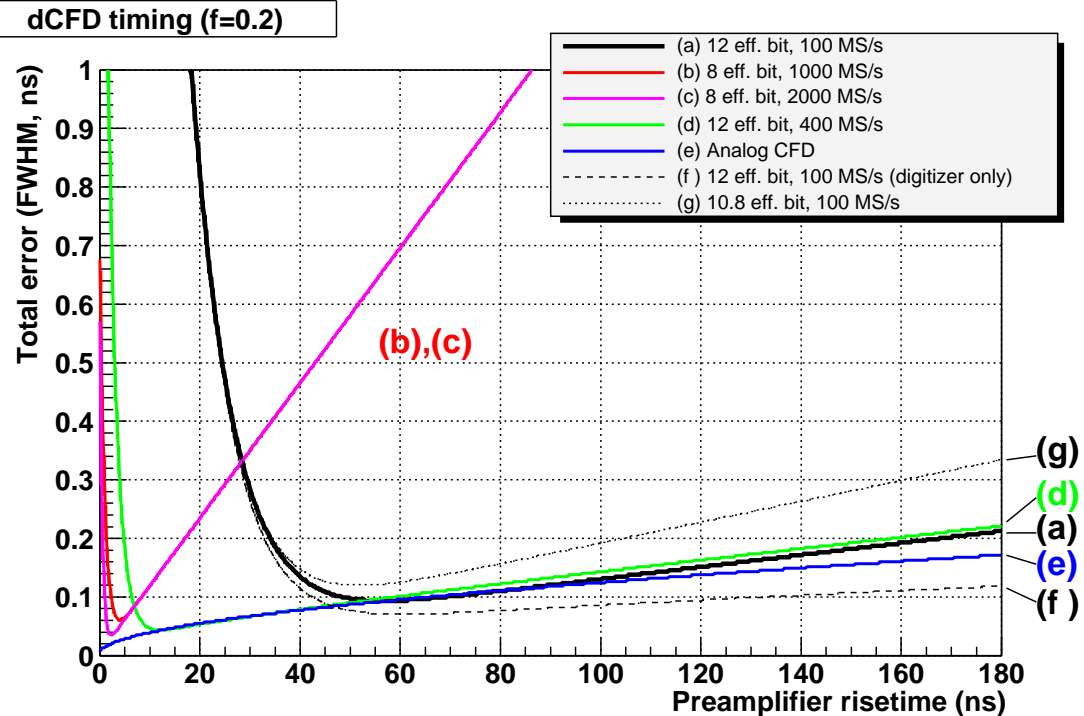


Figure 3.21: Total error on digital Constant Fraction timing ($f = 0.2$) performed by various digital sampling systems (continuous lines labeled from a through d). Data corresponding to a standard analog CFD signal treatment are also shown (continuous line e). For one of the digitizers (100 MSamples/s-12 bit) the contribution due to digitization only is separately presented (dashed line f). The dotted curve g refers to the digitizer of §3.1.

fective bit, 2 GSamples/s digitizer down to 100 MSamples/s gives an improvement by a factor ~ 4.5 , i.e. of about 2 bits: the final effective resolution of about 10 bit is still worse than a “true” 100 MSamples/s-12 (and also 10.8) effective bit converter. Moreover it has also to be noted that oversampling requires a *white* input noise for proper effective operation (otherwise the bit improvement is even smaller due to correlation between samples).

The presented simulated results of the dCFD algorithm has been limited to a fixed value of signal amplitude $A = 0.5R$. While the time resolution obviously scales as $\sigma_{\text{dCFD}} \propto 1/A$ (see Eq. 3.19), the behaviour of the centroid of the estimated time distribution as a function of A , i.e. the *time walk*, has been studied by means of the same simulations previously discussed. For the case of the experimentally used converter (100 MSamples/s-10.8 eff. bit) the results are reported in

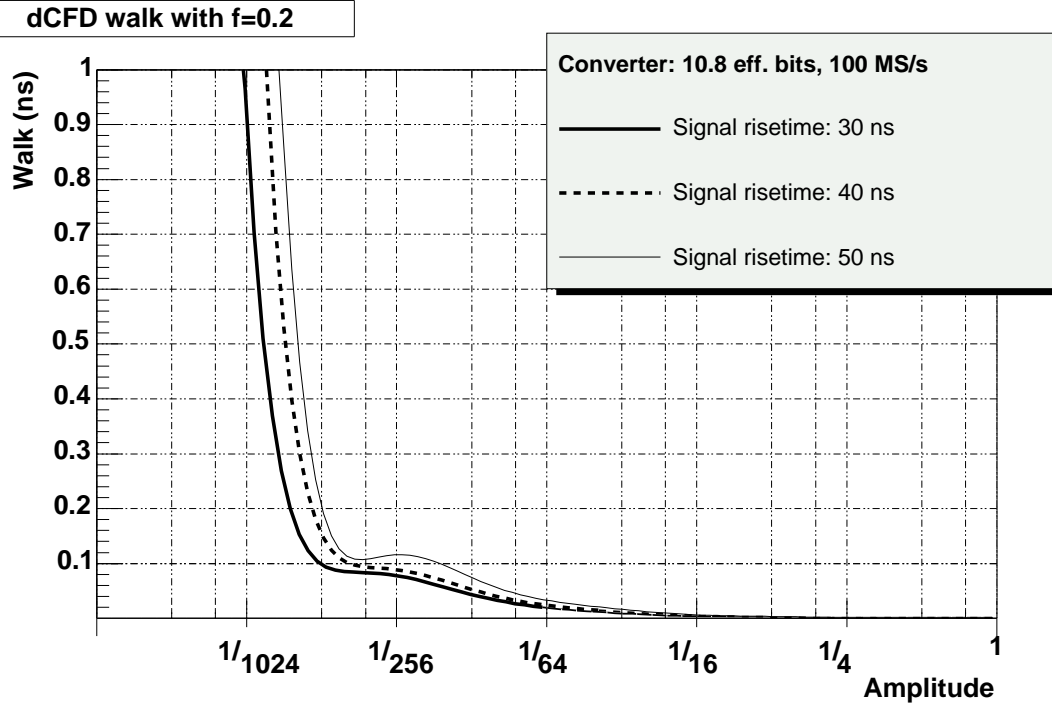


Figure 3.22: dCFD walk for a 100 MSamples/s-10.8 eff. bit converter and fraction $f = 0.2$ as a function of normalized signal amplitude A (log scale). The three curves correspond to different risetimes (10% – 90%) of the input 10.8 eff. bit converter. For this converter the signal risetime value $t_r = 50$ ns corresponds roughly to the minimum of the curve (g) in Fig. 3.20.

Fig. 3.22. The total time walk of the system comes out to be less than 120 ps for a dynamic range of 250: this value compares well with the performances of standard analog CFD systems. Very similar results have been obtained using a linear interpolation.

3.4.3 Digital implementation of ArcCFD timing

In the previous section a discussion of the general properties of AD converters influencing the digital timing resolution has been presented, using the dCFD as an example of algorithm for time mark extraction from the acquired samples.

The dCFD performs in a very different way with respect to analog CFD timing (the sum between the signal and a delayed scaled copy of itself is not needed), and thus, if the quantization noise is negligible, it can achieve better performances due to reduced noise (a factor

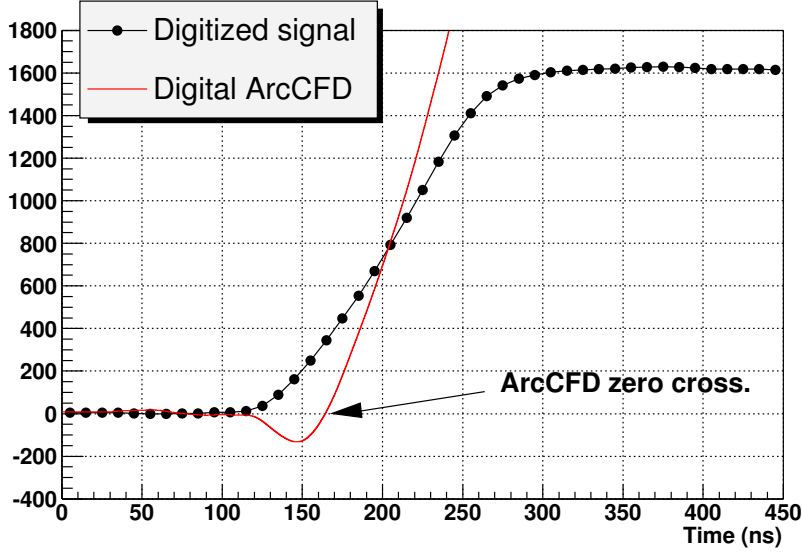


Figure 3.23: Example of digital ArcCFD timing. Starting from the digitized samples the digital equivalent of an ArcCFD signal is used for timing determination with a cubic interpolation of samples.

of $\sqrt{1 + f^2}$). On the other side, any error in the determination of the asymptotic amplitude A reflects into a worsening of the resolution, and this effect is very important when a simple generalization of the dCFD is applied to signals without an asymptotic amplitude (as for example scintillator signals with a phototube readout), where the reference amplitude A is determined for example using the absolute maximum of the signal. Moreover, both the analog CFD and the dCFD exhibit a dependence of the obtained time mark on the signal shape. Whereas this property is useful for PSA applications, it should be avoided as much as possible for coincidence or time-of-flight measurements.

The solution to this problem commonly used in analog electronics is the use of a Amplitude and Risetime Compensated CFD (ArcCFD, see §1.2.8). It is possible to employ the very same operations performed by an analog ArcCFD module on the digital samples, thus building a digital ArcCFD, or “dArcCFD”. An experimental example is shown in Fig. 3.23.

The first step of the computation is a time shift δ of the original sequence $S[k]$. For the case of a fractional delay (i.e. when δ is not a multiple of τ_{clk}) an interpolation of the signal can be used to reconstruct the signal $S_\delta[k] = S(k\tau_{\text{clk}} - \delta)$. The obtained sequence $S_\delta[k]$ is then multiplied for the desired fraction f and subtracted from the

original signal. The result of this operation is presented in Fig. 3.23 (the final signal is shown as continuous for better presentation). Using a proper interpolation the zero-crossing of the final signal can be extracted and used as time reference.

This method is thus the exact digital equivalent of an analog Arc-CFD timing. An example of application and performances is presented in §4.6.

3.4.4 Coincidence and time-of-flight measurements

In many Nuclear-Physics experiments a measurement of the time difference between the arrival of the detected particles in two (or more) detectors is often needed. This information can be used for many physical purposes like characterization of the event or the measurement of the time of flight of the particle (that can be used for a kinematical reconstruction of the event and/or for particle identification).

Thus a method for synchronizing many acquisition channels among each other and/or to an external time reference is needed. The common approach employed in analog systems is the use of Time-to-Analog Converters (TACs) to measure the time difference between the start of the current signal, obtained for example with a CFD module, and a STOP signal common to all modules.¹³

A possible approach for the synchronization of many digital sampling channels is the distribution of a high-frequency timestamped clock information to all the converters and DSP processors (preferably running at the same sampling speed with a synchronized clock). Each clock cycle is labeled with a unique identifier thus implementing the digital equivalent of an “absolute” time of the experiment. At any moment each DSP can obtain this absolute time information, thus achieving the desired synchronization. Many practical difficulties (relative delays between channels, offsets due to different cable lengths, ...) make this approach very challenging from the electronics point of view.

A different approach has been proposed in [3, 5] and it is shown in Fig. 3.24; some signals collected with this method are shown in Fig. 3.25.

The main purpose of the system is to mix a common analog signal to be used as a time reference with each detector output. The general trigger of the experiment, after a delay (about 7 μs in Fig. 3.25),

¹³ This experimental configuration is referred to as “common STOP” mode. Another configuration, where a START signal is common to all modules and each CFD gives a STOP signal, is obviously called “common START” mode.

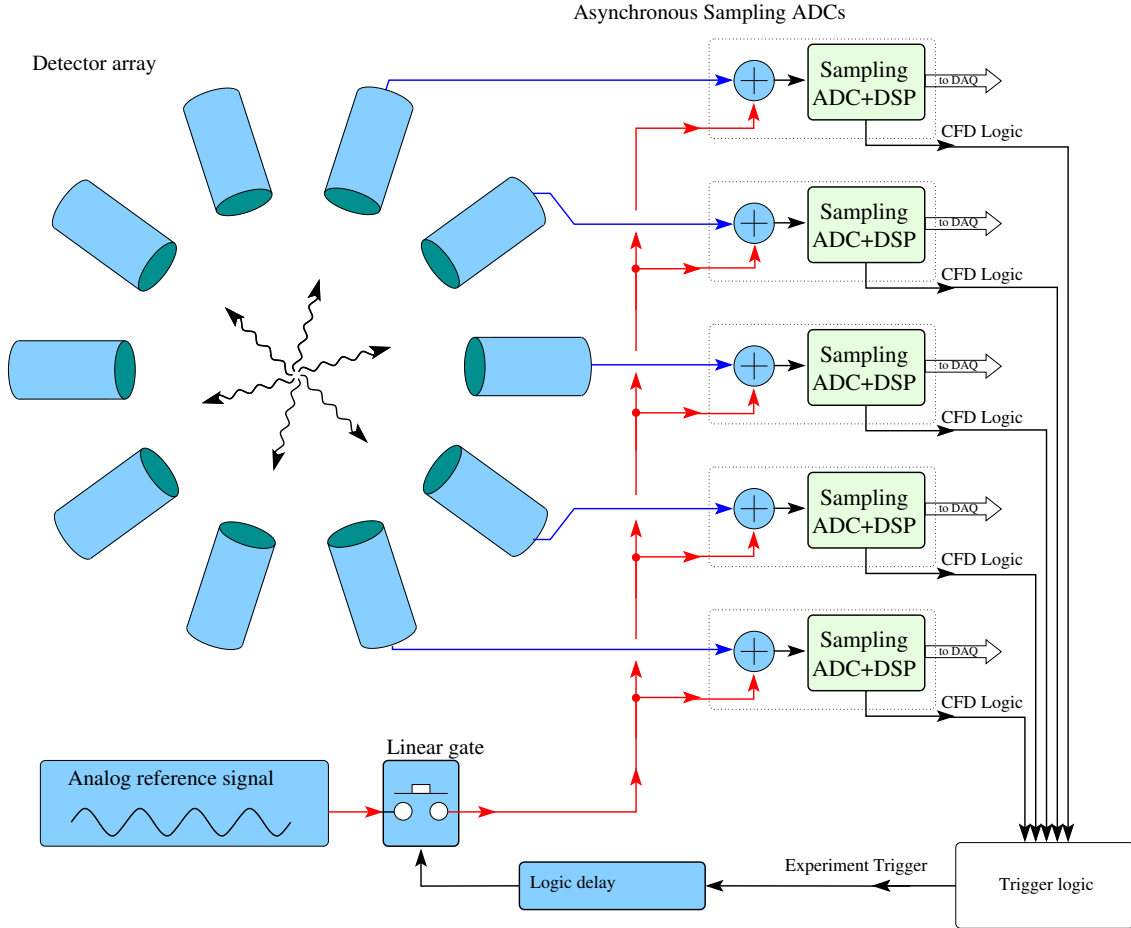


Figure 3.24: Possible electronic chain to employ the analog signal mixing method proposed in the text for time-of-flight or coincidence measurements. A common analog signal is used as timing reference.

closes a linear gate, thus inserting into each digital acquisition channel the time reference signal (for example a high-quality periodic signal with an accurately known frequency). Each AD converter can be run from an independent clock source. The use of AD converters with different sampling frequencies is also possible.

With this configuration, each sample sequence $S[k]$ can be divided into two parts (see Fig. 3.25): a first one where only the unperturbed detector signal is present, and a second one where the time reference signal is present (possibly superimposed on the detector-signal tail). The digital signal processing of the first part of $S[k]$ proceeds with the standard algorithms for the used detector (energy, pulse shape, ...). The DSP software can then separate and analyze the second por-

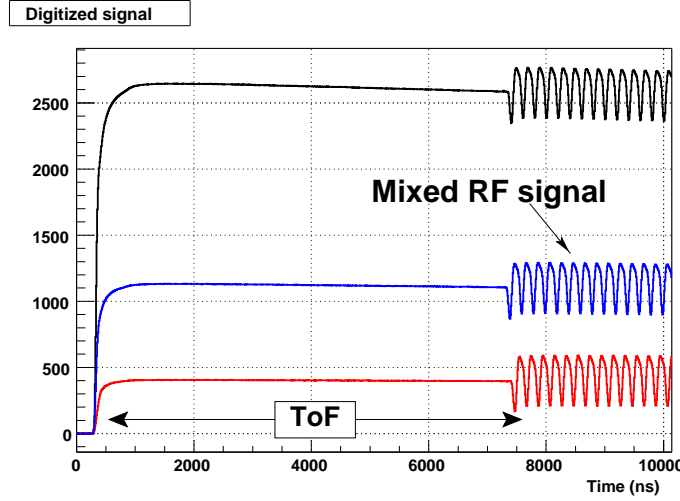


Figure 3.25: Experimental signals collected using an electronic chain like the one in Fig. 3.24. The full time range used is 10 μ s.

tion of $S[k]$, and extract a time reference information. For example, if a periodic reference signal is used as in Fig. 3.25, several “zero-crossing” determinations can be computed and averaged and thus a high-precision time offset can be obtained. For example, in [5] a resolution of about ~ 50 ps has been obtained.

It has to be noted that, depending on the particular electronics used in the linear gate, the first part of the reference signal may be affected by some distortion: this systematic effect can be taken into account by simply discarding the first few zero-crossings of the reference signal.

When this method is used with detector signals having a long tail (as the charge-preamplifier output shown in Fig. 3.25) the detector signal response must be removed before the zero-crossing computation. A simple solution is to compute the sequence $R[k]$ obtained from the original signal $S[k]$ using a digital filter (see §2.4.4) of the form:

$$R[k] = S[k] - \alpha S[k - 1] \quad (3.20)$$

where $\alpha = \exp\left(-\frac{\tau_{\text{clk}}}{\tau_{\text{pre}}}\right)$

where τ_{pre} is the preamplifier decay time and τ_{clk} is the AD converter sampling time. Practically Eq. 3.20 represents a digital deconvolution of the exponential decay of the charge preamplifier output.¹⁴ For the

¹⁴ In this case the opposite operation (i.e. removing the reference signal while keeping the detector one) can be performed, if needed, using the digital equivalent of an analog notch filter [36] tuned to the reference-signal frequency.

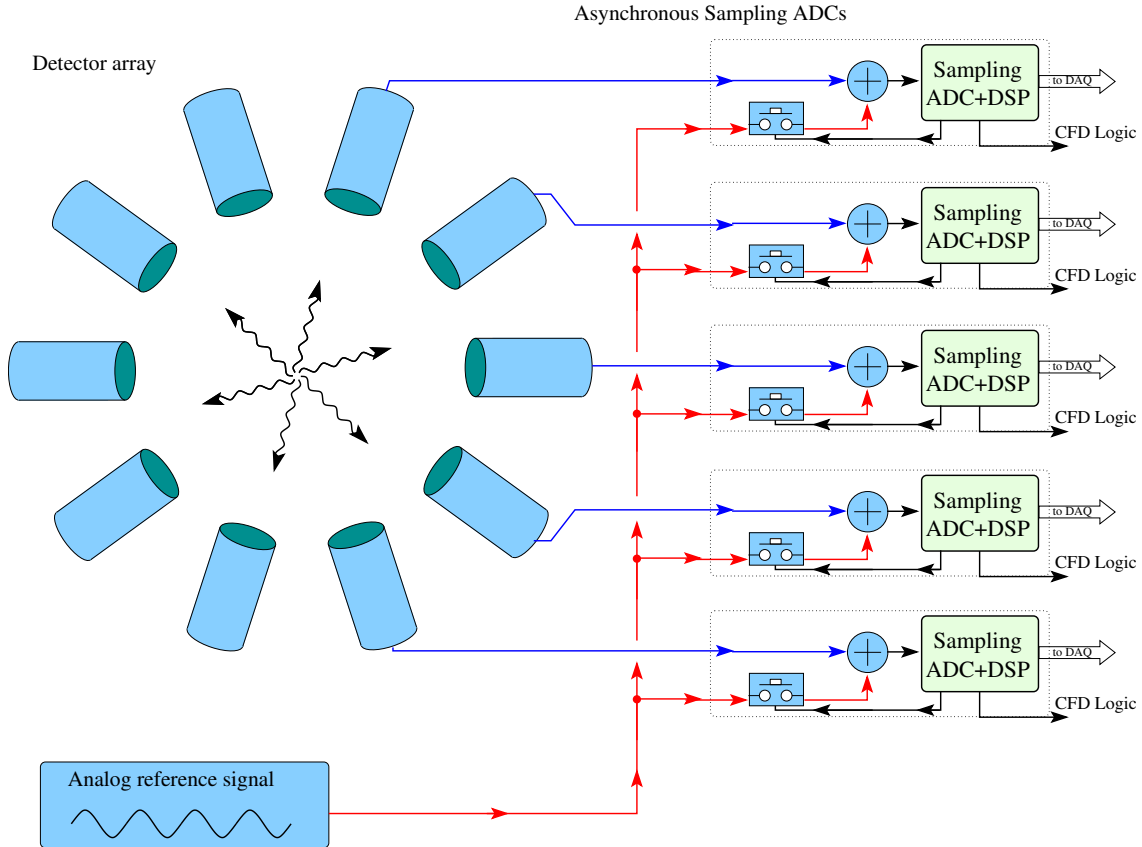


Figure 3.26: Improved electronic chain for the analog signal mixing method. See text for details.

common case of $\tau_{\text{pre}} \gg \tau_{\text{clk}}$ Eq. 3.20 reduces to a simple digital derivative of the input signal $S[k]$ (apart from a multiplication factor).

The obtained time mark is accurate apart from the ambiguity of a multiple of the period of the used periodic signal: for example, using a 5 MHz reference frequency as in Fig. 3.25, an uncertainty of an integer multiple of 200 ns will be present (this value is not critical, a different choice of the reference-signal frequency depending on the particular application is of course feasible). These ambiguities can be easily removed on the basis of the physics involved.

A drawback of the electronic chain presented in Fig. 3.24 is the added noise to the AD conversion due to the presence of the reference signal. In particular, the noise coming from the reference signal lines (possibly due to pick-up or interferences in the connections between the linear gate and the ADCs) is always added to the ADC input line. This increases the equivalent noise of the AD conversion and thus ultimately lowers the available effective number of bits of the system.

for the analysis of the detector output. This undesirable behaviour can be avoided using the improved electronic of Fig. 3.26 (the modular DSP system described in §3.2 has already been designed with the needed features for this application).

The unique linear gate of Fig. 3.24 is replaced in Fig. 3.26 with many linear gates, one for each digital acquisition channel. Each gate is normally in an open position, such that no mixing occurs with the detector signal, thus preventing any worsening of the noise properties of each ADC system. When a detector signal arrives, it is thus sampled with no added noise contribution from the reference signal. The software running on the DSP processor detects the presence of a detector signal and takes care of closing the gate after the desired delay time, thus achieving the needed mixing.

This configuration does not use the general experiment trigger for controlling the signal mixing, and the obtained results are equivalent to those obtained using the system in Fig. 3.24, possibly apart from an integer multiple of the reference signal period. Moreover the signal mixing procedure (that occurs only in the second part of the sampling) does not degrade the noise properties of each digital acquisition channel, thus preserving the achievable performances for energy or timing measurements.

This solution is characterized by a much simpler electronic chain with respect to the timestamped clock approach, (no delay or clock-skew critical parts are needed). No clock synchronization is needed between the used AD converters, that are also allowed to operate at different sampling speeds with no change in the overall system. It is also possible to replace some ADCs (for example with faster ones during an experiment upgrade) with no additional change in the needed hardware and software. The time reference signal can be obtained using a high quality oscillator or the radio frequency signal of the used accelerator machine. Due to its relatively low frequency and high amplitude, feeding this signal into many modules is straightforward. Conversely, the timestamped clock approach is able to withstand a much higher counting rate than the mixing one (with the chain of Fig. 3.26 no event must occur during the mixing time) and finds a simpler application in trigger-less systems.

In §4.4 an example of experimental application of this method is shown, whereas a simple extension of it is described in §4.8.

3.5 Lookup table for on-line signal fitting

Digital systems can be used to build signal-processing modules with

similar or improved characteristics with respect to standard analog methods. It is also possible to apply algorithms that cannot be implemented by analog means, as for example the fit of the signal shape with a known function, describing it as a function of impinging particle charge, mass and energy. At least in principle, this approach could lead to an improved particle-identification resolution with respect to other more conventional methods.

The drawback of this kind of computations is the huge amount of processing power needed, because the signal shape can often be properly described only by a function with a non-linear dependence on the to-be-fitted parameters.

A special case where the signal can be decomposed in a linear combination of three (or more) signals has been studied in [1, 2] and the results will be described in §4.11.

Briefly, the detector output $S[k]$ can be schematized as follows:

$$S[k] = \alpha f_A[k] + \beta f_B[k] + \gamma f_C[k] \quad (3.21)$$

where $f_A[k]$, $f_B[k]$ and $f_C[k]$ are tabulated functions characteristic of this detector (possibly different for each detector) and α , β and γ are the parameters to be fitted, related to the energy loss of the particle in different detector sections.

Once the three functions $f_A[k]$, $f_B[k]$ and $f_C[k]$ have been off-line tabulated and stored in a lookup table (hence the name of the method), the on-line computation reduces to the minimization of:

$$\chi^2 = \sum_k \left(\alpha f_A[k] + \beta f_B[k] + \gamma f_C[k] - S[k] \right)^2 \quad (3.22)$$

This leads to a linear system that can be easily solved and efficiently coded for on-line applications (more details in [2]).

The performances of this method (that cannot be implemented by analog means) are discussed in §4.11.

3.6 Software for off-line analysis

All the algorithms proposed in the previous sections have been developed for fast on-line analysis but tested with an off-line analysis of the data collected using the prototype digitizer described in §3.1.

The analysis has been carried out using the ROOT [48] data analysis framework running on Linux machines. ROOT is a C++ environment, mainly developed for high-energy LHC experiments, targeted at large scientific data collection and analysis.

Some C++ classes have been written in order to add signal processing capabilities to the framework. Apart from “service” classes, as for

example binary read of data file from disk or computation of nuclear energy losses, the relevant developed classes are (the full developed library required about 10,000 lines of code):

Signal class

This class holds a sampled waveform $S[k]$. It has a variable length and a variable τ_{clk} , and it uses a public interface based on “physical” units (i.e. the time is expressed in ns instead of samples). This makes it possible to write programs that are almost sampling-frequency independent, thus focusing more on the processing than on the indexing. An extensive overload of all the common operators $+$, $-$, $*$, $=$, \dots , have been performed in order to have a simple representation of all the common signal processing operations (addition between two signals, convolution, copy, \dots). All of the proposed algorithms (and their variants) have been implemented as methods of this class.

Digital-filter class

This class holds the complete information needed for the description of a digital filter. It has a variable number of poles and zeros and uses a public interface based on “physical” units, for easy integration with the signal class. Many methods exist for building various filter types as well as combining two or more of them into one.

Digital-filter fitter class

This class performs a complete digital filter fit as described in §3.3.5.

All the results presented in this chapter and in the following have been obtained using these classes inside the ROOT framework.

Chapter 4

Experimental tests with various detectors

The hardware and the software proposed and discussed in Chap. 3 have been experimentally tested over many detector types, in order to better understand the properties of the algorithms and the factors limiting the achievable performances (electronic or detector-related). The tests have been also performed to check whether a digital sampling system can be used for effective replacement of the standard analog measurement techniques.

The experimental tests have been performed using the digital sampling prototype discussed in §3.1. This system has no on-line signal-processing capabilities and thus all the results shown in this chapter have been obtained with off-line analyses. Although all the algorithms discussed in Chap. 3 have been off-line applied on the collected data, they are meant to be simple and fast enough to be used for on-line applications with a DSP-based system, while providing the needed performance level.

With the exception of few cases, a systematic study of the optimal choice of the various digital processing parameters (shaping time, dCFD fraction, ...) to obtain the best performance has not been carried out. This study is of course needed when one or more of these detector digital-sampling configurations are used in a real experiment.

Part of the experimental data has been collected during a beam test at Laboratori Nazionali di Legnaro (LNL) in December 2002 using the $^{16}\text{O} + ^{116}\text{Sn}$ reaction at a beam energy of 250 MeV (referred to as “LNL test” in the following). Besides, several tests with small radioactive sources have been performed in our laboratory.

In the next future, more experiments are planned, aiming at testing the capabilities of the detector-digitizer system over a wider range of charge, mass and energy of the detected particles.

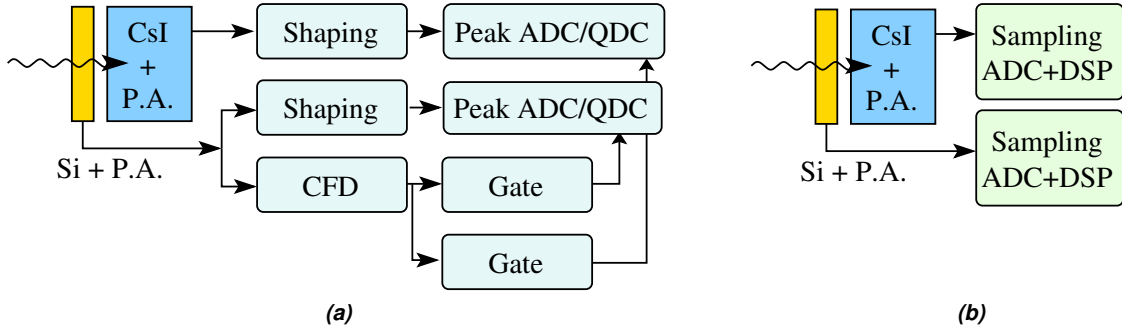


Figure 4.1: Typical electronic chains for ΔE - E measurements using silicon and CsI detectors with preamplifier (P.A.) readout. (a) analog version, (b) digital version.

4.1 Identification using ΔE - E Si-CsI

The ΔE - E method is a common detector configuration used for charged particle detection, based on the dependence of the energy deposited by a charged particle on its charge and mass. A typical system is shown in Fig. 4.1. It is possible to measure the total energy and to achieve identification for particles that punch through the ΔE detector (usually a silicon detector) and are stopped in the E detector (usually a silicon or CsI detector). Due to the dependence of energy loss on particle type and energy (see §1.2.1) particle identification can be achieved using a ΔE (silicon) versus E (CsI) correlation plot.

The lower identification threshold is equal to the punch through energy in the ΔE detector, whereas the identification capabilities are dominated by the energy resolution and thickness uniformity of the ΔE detector (the E detector plays a minor role).

For these reasons, the choice and the performances of the first detector are critical. A common solution, for experiments with beam energies of the order of 20–40 AMeV, is the use of a 300 μm thick ($\lesssim 1\%$ thickness uniformity) Si detector coupled to a high-resolution electronic chain. A typical analog electronic chain is shown in Fig. 4.1(a).

The digital equivalent of that electronic chain is shown in Fig. 4.1(b): both preamplifier outputs are directly coupled to two digital sampling systems (possibly using the same trigger). It is possible to appreciate the increased simplicity of the digital electronic chain with respect to its analog counterpart.

A silicon and a CsI detectors of the GARFIELD [40] apparatus have been used in the “LNL test”. The silicon detector has a $\sim 2 \text{ cm}^2$ active area and 300 μm thickness. The size of the CsI detector (having

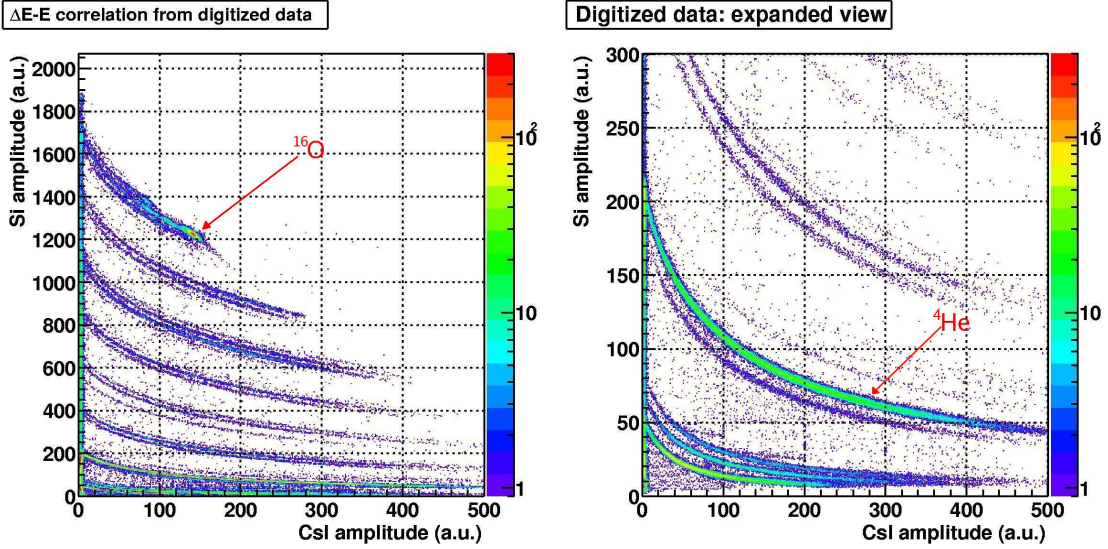


Figure 4.2: Left: Experimentally obtained results with a ΔE - E Si-CsI detector using a digital sampling system. Right: expanded view of the same dataset. A good isotopic resolution is clearly achieved for all the detected nuclei. Both pictures have been obtained using only one AD converter for the ΔE detector.

a photodiode readout) is about 30 cm³. A single AD converter has been used for the acquisition of the silicon signals, thus covering with a single electronic channel the whole dynamic range of the ΔE detector.

The collected signals from both detectors have been processed with a baseline subtraction (§3.3.2) followed by a digital semigaussian shaping (§3.3.3) with a 2 μ s shaping constant. The obtained results are shown in Fig. 4.2, where the lines corresponding to ¹⁶O and ⁴He have been highlighted. It is possible to see that full charge and mass identification has been achieved for all the detected particles. The choice of the shaping time is not critical as results of the same quality of Fig. 4.2 have been also obtained with different settings. Moreover, very similar performances have been also achieved using much simpler algorithms (for example signal integration, §3.3.4).

It has to be noted that the vertical spacing between two isotopic lines (or the vertical width of each line) is about 20 using the silicon arbitrary units of Fig. 4.2, when the full range is less than 2000. Thus the dynamic range needed in this test to achieve full isotopic identification is of the order of 100–200, and this requirement is easily fulfilled by the used sampling AD converters (having 12 bit, 10.8 effective). The limiting factor for the particle-identification resolution

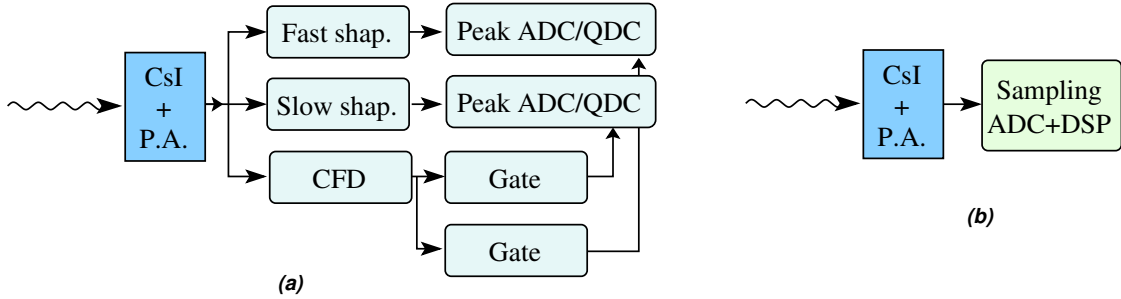


Figure 4.3: Typical electronic chains for pulse-shape measurements using a CsI detector with preamplifier (P.A.) readout, (a) analog version, (b) digital version.

can then be traced back in the detector properties (mainly doping homogeneity, thickness uniformity and energy resolution).

4.2 Pulse shape using CsI(Tl)

It is well known from the literature (for example [49] and references therein) that light output from a CsI(Tl) scintillator can be described as a signal with two components which are characterized by quite different decay times (about 700 ns and 2 μ s).¹ The relative amplitude of these components depends on the charge and on the mass of the incoming particle (that have also a slight influence on the decay time). The total light output is related to the energy of the incoming particle with a non-linear law that depends also on the charge and on the mass of the incoming particle [44].

For these (and other) reasons, CsI(Tl) scintillators are often used for particle identification purposes using a proper signal-processing chain. A typical analog setup is shown in Fig. 4.3(a).

The signal coming from the detector output (usually a photodiode with charge-preamplifier readout or a phototube is used) is split and sent to two shaping modules having different shaping times (for example about 700–1000 ns and 2–3 μ s). The two shaped outputs are then measured by two Peak-sensing ADCs or QDCs controlled by a gate-generator module. The two final converted values will both contain the information coming from the two CsI components with different weights (due to the different shaping times). This allows the extraction of the desired particle identification. Due to the different

¹The possibility of a third component with a decay time of the order of $\sim 7 \mu$ s is also investigated in the literature, see [49].

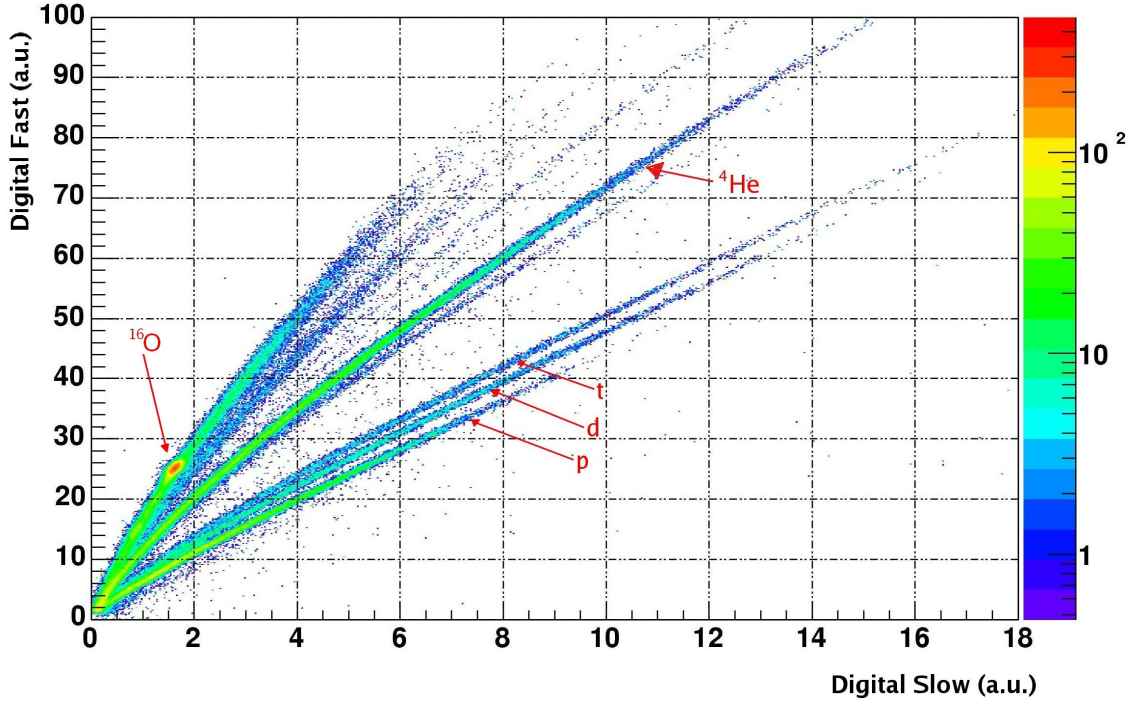


Figure 4.4: Experimentally obtained results with a CsI(Tl) detector and a digital sampling system. A good isotopic resolution is clearly achieved for particles with $Z \lesssim 3$.

shaping times, the method is also known as “fast-slow pulse shaping” analysis.

It is possible to obtain the same results applying a digital signal-processing system, as shown in Fig. 4.3(b). It is interesting to note the simplicity of the digital CsI processing system with respect to its analog counterpart.

The CsI detector is the same used for the $\Delta E-E$ experiment discussed in §4.1.

The signals, collected during the already mentioned “LNL test” from the scintillator, have been processed with a baseline subtraction (§3.3.2) followed by two different digital semigaussian shaping filters (§3.3.3) with 700 ns and 2 μ s time constants. The maxima of the two shaped signals are extracted and a correlation plot between the two is built. In the final implementation to be used for the GARFIELD digital upgrade, the slow filter will be realized with the digital equivalent of a standard spectroscopy amplifier described in §3.3.5. This allows the use of the calibration work already done using the analog system (as discussed in §3.3.5).

The digital sampling method allows also the use of different analysis methods for particle identification, as the lookup table method described in §3.5. As shown in §4.11, this method has been applied to a similar detector that uses CsI(Tl) as active element for particle identification.

The obtained results with digital shaping are shown in Fig. 4.4. A clear isotopic identification is possible for particles with $Z \lesssim 3$ (in Fig. 4.4 the lines corresponding to H isotopes and to ${}^4\text{He}$ have been highlighted), whereas for $Z > 3$ (nuclei with Z up to 8 were present in this test) only a marginal charge resolution is available.

These results compare well with those attainable with the state of the art processing using analog electronics, as for example [50]

An identification line in Fig. 4.4 has a vertical width of few units (using the Digital Fast arbitrary units of Fig. 4.4), whereas the full range is around 100. This translates into a needed dynamic range capability for the used electronics of the order of 100–200, and this requirement is easily fulfilled by the sampling AD converters used (having 12 bit, 10.8 effective). It is then possible to recognize the characteristics of the detector as the limiting factors of the achievable particle identification resolution.

4.3 Pulse shape in silicon

It is well known (see for instance [51]) that once a charged particle is stopped inside a silicon detector the shape of its output signal contains information about the type of the detected particle; moreover the rear side injection technique [52, 53] increases the dependence of the shape of the signal on the charge (and even the mass) of the impinging particle, because the effects on the pulse shape due to the high ionization density are enhanced in the lower-field regions probed by stopped particles (see also Chap. 5).

Therefore, the use of PSA techniques in the ΔE detector of a standard ΔE -E silicon telescope allows the identification of particles that are fully stopped in the ΔE detector, thus considerably lowering the thresholds of the system. This application requires a good resolution in both energy and time domains, as well as a good doping uniformity of the chosen detector [54].

In Fig. 4.5(a) a typical analog chain for pulse shape analysis in a reverse mounted silicon detector is shown. The signal coming from the detector (a charge preamplifier output is commonly used) is split and sent to a shaping filter and Peak sensing ADC for a high-resolution energy measurement. A quantity related to the risetime of the signal

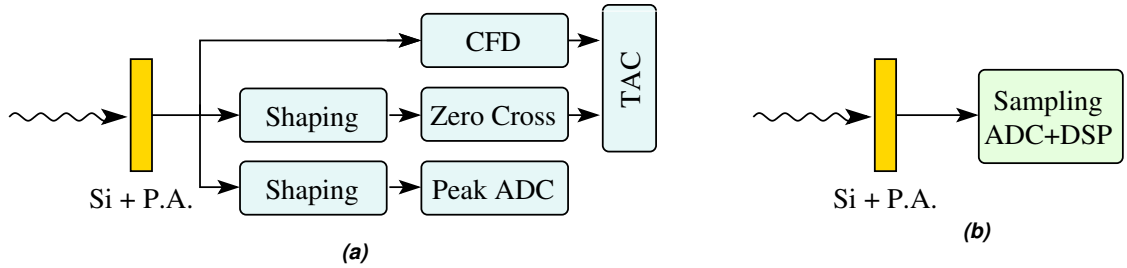


Figure 4.5: Typical electronic chains for pulse shape analysis using a reverse mounted silicon detector. (a) analog version, (b) digital version.

is obtained using a CFD, a zero-crossing module, and a Time to Amplitude (TAC) converter. Building a correlation plot between the measured energy and the measured risetime the desired identification can be achieved. An alternative way to measure the signal risetime can be obtained using two CFD or threshold modules with different settings [55].

In Fig. 4.5(b) the equivalent digital signal-processing chain is shown. The simplicity with respect to its analog counterpart is remarkable: this is mainly due to the possibility of extracting both high-resolution energy and high-resolution timing measurements using a single AD converter with low noise, i.e. high effective number of bits.

The performances of the digital sampling system have been experimentally checked during the “LNL test”, where a $300 \mu\text{m}$ Neutron Transmutation Doped (NTD) silicon detector has been placed inside a scattering chamber (about 1 m from target, $\theta \simeq 11^\circ$) in the reverse field configuration. The total active area used is $\approx 500 \text{ mm}^2$.

As far as the energy information is concerned, the acquired signals have been processed with a baseline subtraction (§3.3.2) followed by a digital semigaussian shaping (§3.3.3) with a $2 \mu\text{s}$ time constant. The risetime information has been obtained as the difference between a digital zero-crossing time (dZC) and a digital CFD (dCFD, described in §3.4.2) with $f = 0.2$. The digital zero-crossing time has been obtained using the digital equivalent of a 100 ns delay-line shaping [14] and extracting the zero-crossing value with a cubic interpolation of samples (see §3.4.1).

In Fig. 4.6 the overall pulse-shape correlation is shown: on the vertical axis the amplitude of the digitally shaped signal is reported whereas on the horizontal axis the difference between the digital zero-crossing time dZC and the digital constant fraction dCFD time mark is shown.

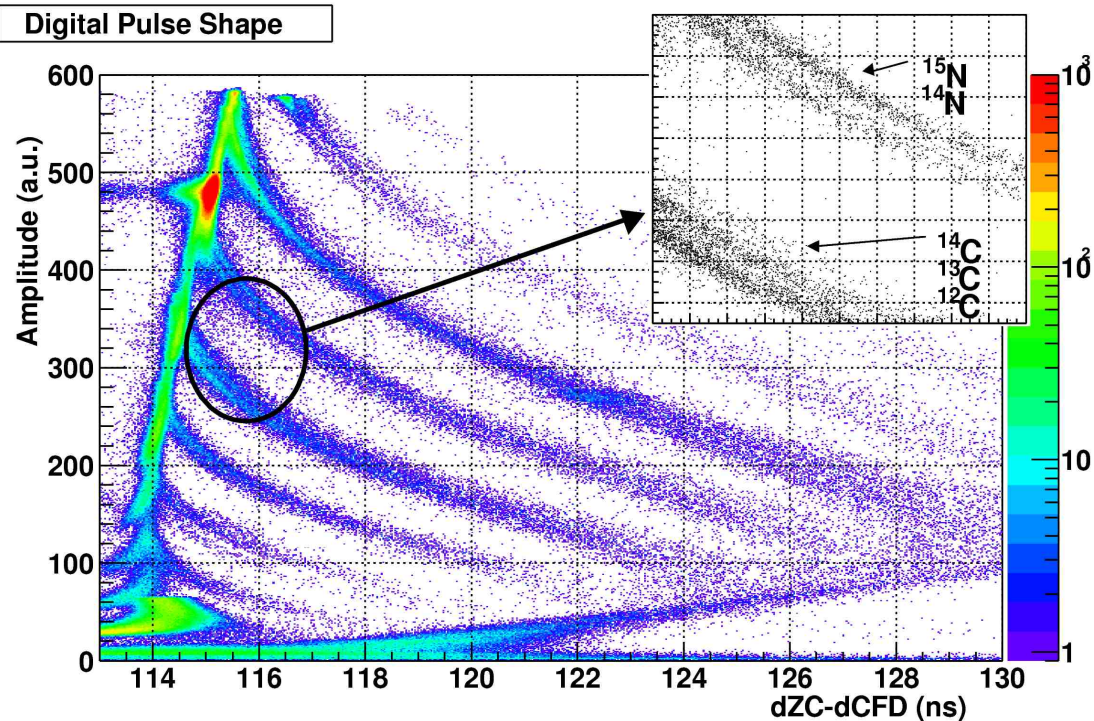


Figure 4.6: Digitally determined Amplitude versus dZC-dCFD time correlation: a full charge identification is apparent. In the inset: detail of the isotope separation of carbon and nitrogen. Data have been obtained with the electronic chain of Fig. 4.5(b).

It is clearly seen that the system is able to discriminate between different particles with full charge resolution (a more detailed discussion is presented in Chap. 5). The expanded view makes it possible to appreciate also the existence of a somewhat marginal mass resolution. The energy resolution (electronic contribution and counting rate effects) on the vertical axis was measured to be about 100 keV, estimated by means of a calibrated charge injected into the preamplifier during the measurements. Similar values have been obtained using different digital shaping times. The counting rate was about 10 kHz.

For a fixed particle energy and type, the silicon signal is characterized by a constant pulse shape (apart from residual effects as discussed in the following). This makes it possible to perform an experimental test of the digital timing performances, for example using the risetime distribution of elastically scattered events (for which both energy and particle type are constant and known). The obtained timing results are shown in Fig. 4.7. The difference between the digital zero-crossing

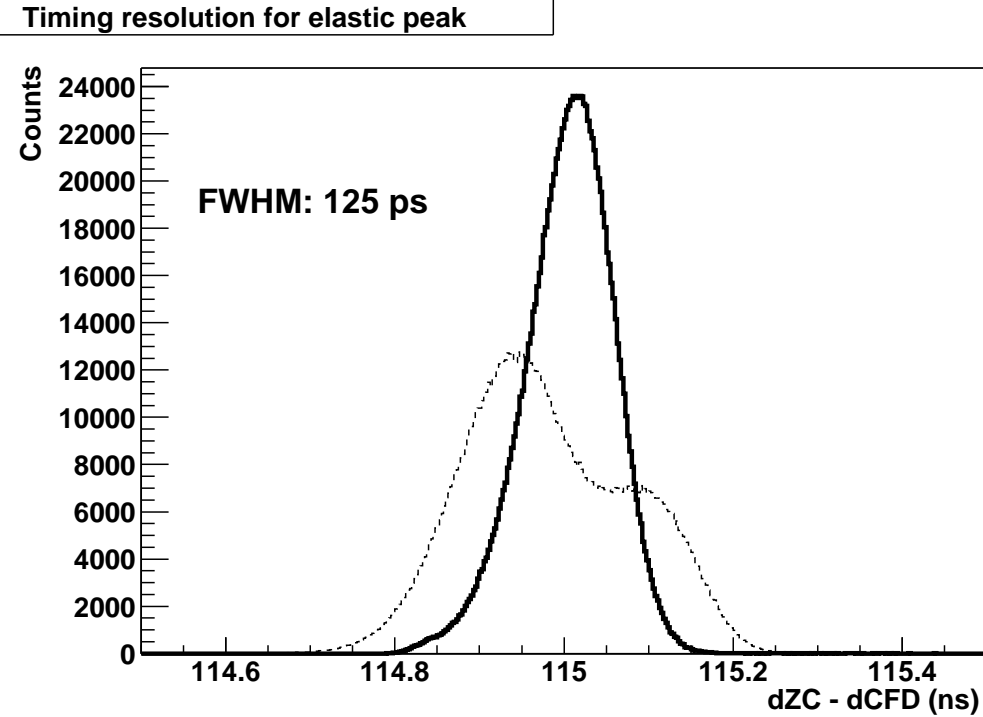


Figure 4.7: Full line: $dZC - dCFD$ time spectrum (see text) for the elastic peak as obtained with the digital sampling system as in Fig. 4.5(b) and cubic interpolation. Dashed line: the same quantity obtained using linear interpolation: note the strongly non-gaussian shape of the peak and the worse resolution.

time dZC and the digital constant fraction $dCFD$ time mark for elastic events is shown. At the used bombarding energy of 250 MeV the elastically scattered ^{16}O particles are not stopped in the silicon detector. The FWHM of the elastic peak is 125 ps. In Fig. 4.7 the timing spectrum obtained for the same events with a linear interpolation is also shown. As discussed in §3.4.1 and §3.4.2 the interpolation noise for the linear kernel gives an important contribution to the achievable resolution. These data are in agreement with the results of the realistic simulation presented in Fig. 3.21 (and in ref. [5], Fig. 6), given the experimental risetime $t_r \approx 60$ ns, and taking into account that the $dCFD$ and dZC are not independent quantities.

In order to test whether the identification performances in the low-energy portion of Fig. 4.6 are limited by the digital sampling system or by the used detector, an experimental test of silicon homogeneity has been carried out using the proton burst system described in [56].

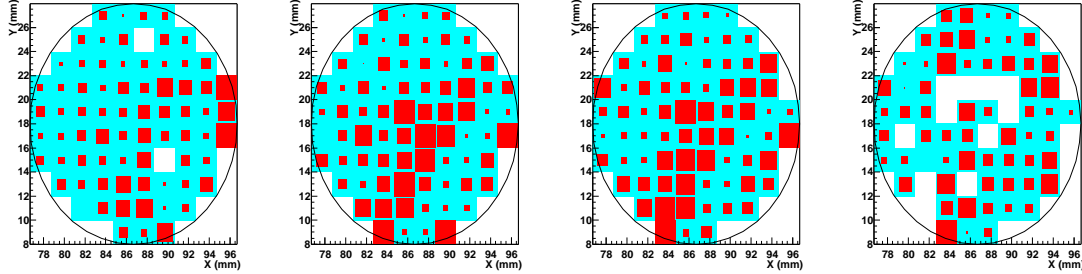


Figure 4.8: Risetime of a silicon detector as a function of position for 4 different energies. The size of the boxes is proportional to the observed mean risetime in that point. White boxes inside the circle refers to missing data.

The silicon detector has been irradiated with a collimated bunch of protons. Using a moving support it is possible to scan the surface of the detector and to analyze its response as a function of position. The digital acquisition chain in Fig. 4.5(b) has been used.

The results are reported in Fig. 4.8 where the risetime distribution as a function of position is presented for different proton energies (the detector has a circular shape with a diameter of ~ 30 mm). The size of each box in Fig. 4.8 is proportional to the observed mean risetime. Regions of slow (i.e. large) risetimes are clearly visible near the center of the detector and on one edge, and they are present with the same characteristics in all the tested beam energies. The observed fluctuation is of the order of 5–15% of the nominal risetime.

This effect is more important for short-range highly ionizing particles as those in the right side of Fig. 4.6, which explore only low electric-field regions. These results can be extrapolated back to the data in Fig. 4.6, giving an estimate for an additional contribution to the identification resolution for low-energy particles of about 0.5–2 ns. This effect is not negligible, due to the high timing resolution needed for isotopic identification (see also the inset of Fig. 4.6).

It is then possible to conclude that, probably due to non-homogeneities of the silicon doping, the signal risetime of the used detector exhibits a dependence on position, finally lowering the achievable identification performances. The foreseen tests using heavier beams will be also useful to better understand the effect of silicon homogeneity on the identification properties of the system.

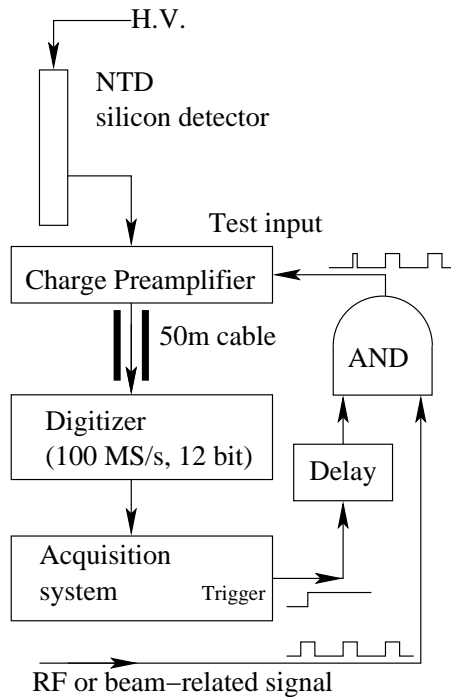


Figure 4.9: Electronic chain used to perform the digital time-of-flight test described in the text.

4.4 Time of flight using silicon

time of flight In §3.4.4 an original method for time-of-flight or coincidence measurements using digital sampling techniques has been presented. An experimental test has been carried out in order to test its feasibility, using the prototype digitizer (without onboard DSP) described in §3.1. Because no signal-mixing electronics is available on that prototype a direct application of the method as depicted in Fig. 3.26 is not possible. A slightly different electronic chain, feasible for application to few channels only, has thus been implemented as shown in Fig. 4.9. This configuration is in practice equivalent to the one in Fig. 3.24 except for the injection of the periodic reference signal into the test input of the silicon preamplifier, instead of using a dedicated input line on the digitizer. The reference signal used is the periodic radio-frequency (RF) coming from the ALPI accelerator of the Laboratori Nazionali di Legnaro (LNL) where the “LNL test” has been carried out.

The RF signal has a fixed phase relationship with the arrival time of the beam on the target, thus a measurement of the time difference between the silicon-signal start time and the next RF zero-crossing

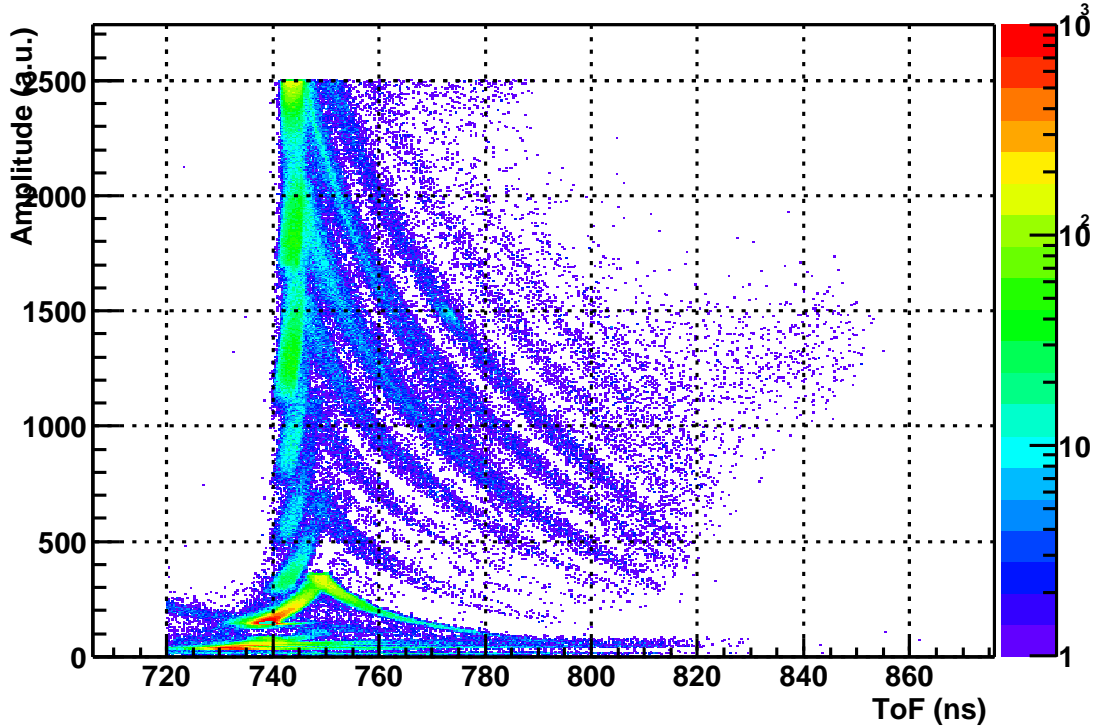


Figure 4.10: Digital energy versus time-of-flight correlation obtained with a reverse mount silicon detector. The intrinsic beam timing resolution (measured by other means) was about 1.5 ns.

(see Fig. 3.25) is a direct determination of the particle time of flight (apart for a fixed offset). An energy versus time-of-flight correlation should show the formation of “lines” corresponding to the different particle masses (hence the name of mass lines).

The silicon detector used has been mounted in a reverse field configuration (see §4.3 and Chap. 5). Using this configuration a dependence of the silicon start time on the particle charge is expected, as long as the used time mark (a dCFD has been used) is not completely insensitive to the different signal shapes.

In Fig. 4.10 the experimentally obtained digital energy versus time of flight (plus a constant time offset) correlation is shown. The intrinsic beam timing resolution was about 1.5 ns, as measured with a fast plastic scintillator and standard fast analog electronics.

The expected timing resolution of the digital sampling system, using the estimates and the simulations of §3.4 and §3.4.4, is about $\sim 100\text{--}150$ ps FWHM. Due to the much poorer beam resolution the

experiment is not a significant test of the digital timing properties. A correlation very similar to Fig. 4.10 has been also obtained using standard analog electronics.

Apart from the poor timing resolution, Fig. 4.10 shows the presence of charge lines – 8–9 lines can be identified in the figure – instead of mass lines – about 16–20 lines would be expected as in standard energy versus time-of-flight correlations. This deviation from the expected behaviour can be connected to a residual dependence of the dCFD time mark on the signal shape (as anticipated). This charge dependence is larger than the expected mass dependence thus giving rise to charge lines instead of mass ones.

This effect can be greatly reduced by using a dArcCFD (§3.4.3) timing. Possibly due to the poor beam resolution, the resulting correlation (not shown) does not exhibit any charge or mass lines, although the obtained time-of-flight spread (i.e. the difference between the minimum and the maximum time of flight seen in Fig. 4.10) is reduced and becomes much closer to the theoretical time of flight (without any pulse shape dependence). More tests using a beam characterized by good timing properties are planned.

4.5 Energy measurement using germanium

In order to test the energy resolution properties of a digital sampling system, an experimental test with a large-volume (30% efficiency) coaxial germanium detector has been carried out, using a ^{60}Co source placed near the detector. The preamplifier output of the detector is directly coupled to the prototype digitizing system of [1, 2] using a delay line of about 1 μs length. This simple configuration allows the application of the digital shaping algorithms described in §3.3 with a baseline time $T_{\text{BL}} = 1 \mu\text{s}$.

In Fig. 4.11 the obtained energy spectrum using the digital sampling method is presented. The full range of the AD converter in this configuration is about 2.5 MeV. The achieved resolution on the 1.332 MeV line is 2.2 keV FWHM, where the resolution on an injected pulser signal is 1.4 keV FWHM.

From independent measurements the maximum electronic resolution (after subtraction of the intrinsic detector noise) for this detector-preamplifier system is known to be $\sigma_{\text{sha,opt}}^2 = 0.7 \text{ keV}$. It is thus possible to use Eq. 3.6 (discussed in §3.3.3) to verify the noise properties of the digital system. The measured effective number of bits of the used converted has been considered (ENOBI=10.8).

In Fig. 4.12 the result of the comparison is reported. The expected

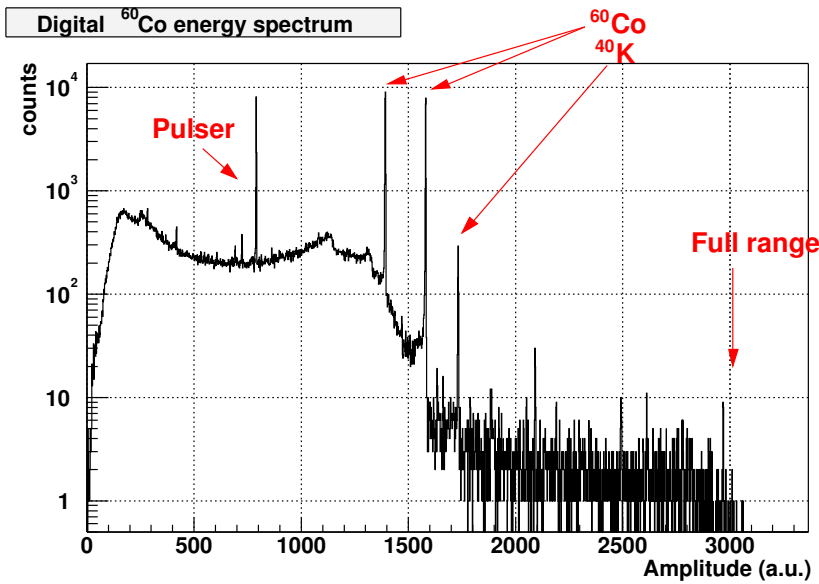


Figure 4.11: Energy spectrum obtained with a large-volume germanium detector with digital signal processing.

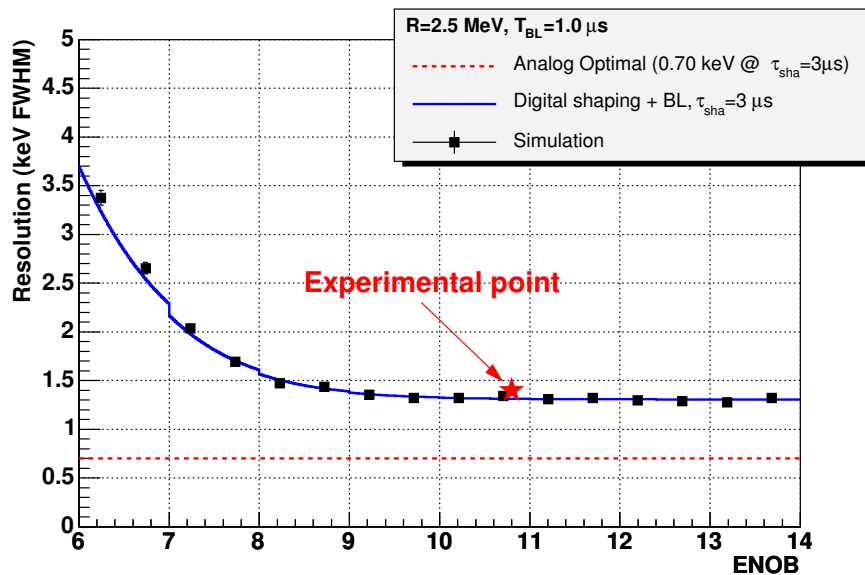


Figure 4.12: Same as Fig. 3.8, but including into the simulation and into the computations an experimental configuration similar to the one used in Fig. 4.11. The \star point refers to an experimental measurement.

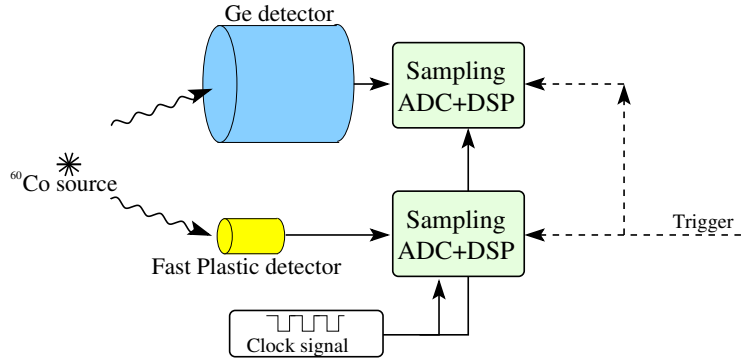


Figure 4.13: Electronic chain used to perform the timing resolution test using a germanium detector. The two ADCs use the same clock source and the same trigger.

resolution has been plotted as in Fig. 3.8, but using the experimentally observed values for the baseline time T_{BL} , the ADC range R , the preamplifier and detector noise, the ADC effective number of bits.

The experimentally obtained resolution for the pulser signal (i.e. the overall electronic noise) using the digital shaping system is shown as \star . A good agreement with the calculation of Eq. 3.6 is present, although the availability of a single measurement point does not allow a stringent comparison.

4.6 Timing using germanium

The electric field inside a large-volume closed-end coaxial germanium detector is not constant and thus many signal shapes correspond to a fixed γ energy, depending on the interaction point. In a coincidence measurement between two or more germanium detectors a timing algorithm insensitive to the different shapes is needed in order to achieve a good timing quality.

The achieved timing resolution using standard state-of-the-art analog electronics with the large (30% efficiency) coaxial germanium detector used in our tests is about 3.2 ns FWHM @ 1.332 MeV, in agreement with the manufacturer specifications [57].

An experimental test has been carried out using the electronic chain of Fig. 4.13. The two cascaded γ rays coming from the decay of a ^{60}Co source are measured in coincidence using a fast plastic scintillator and a germanium detector. As discussed in §1.2 the intrinsic timing properties of the Fast Plastic Scintillator (~ 300 ps FWHM using digital sampling methods, see §4.9) are far superior to the germanium ones,

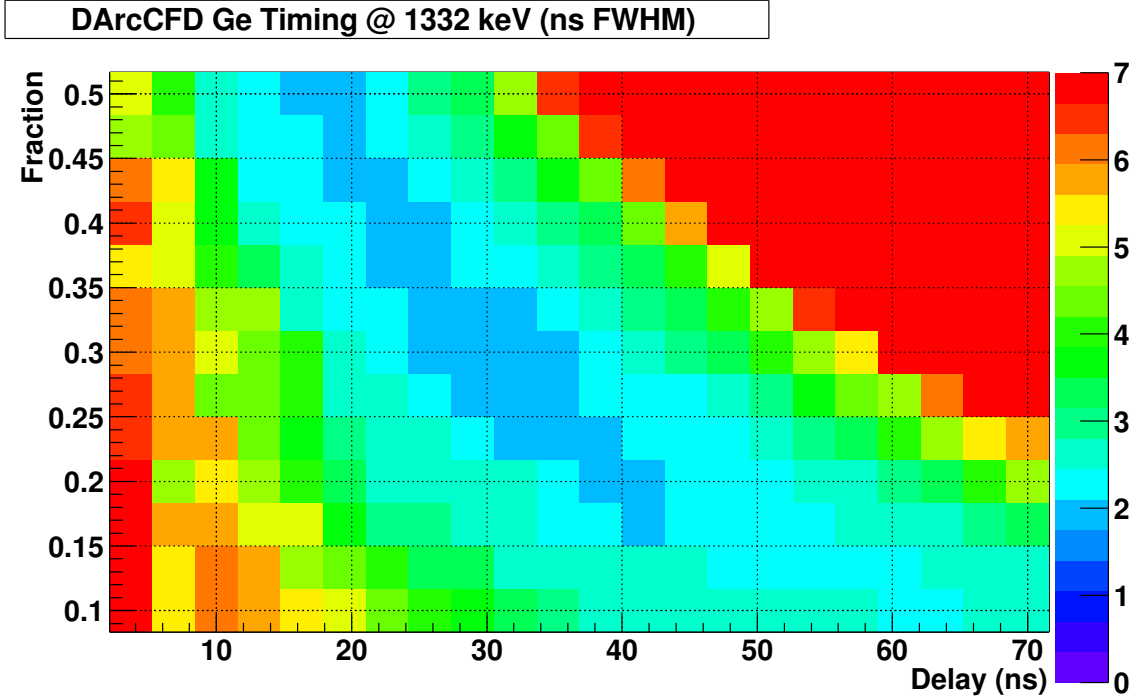


Figure 4.14: Resolution of dArcCFD timing as a function of the delay δ and of the fraction f .

and thus the output from the scintillator can be used as reference for determining the timing properties of the germanium detector.

Two sampling AD converters are used, controlled by the same clock and the same trigger: with this configuration a time synchronization between the two channels is trivial, because there is a sample-by-sample time correspondence between the two acquired waveforms. Note that this electronic setup is very effective and easily to implement only when few digital channels are involved (two in this test), but it would be unfeasible for applications having many acquisition channels (see §3.4.4).

The dArcCFD algorithm discussed in §3.4.3 has been used for processing the germanium signals.² This algorithm (as its analog counterpart) is characterized by two parameters, namely the delay δ and the fraction f . In Fig. 4.14 the obtained timing resolution as a function of δ and f is shown: it is possible to see that a “valley” of values giving a similar resolution near to the optimal one is present. The best timing resolution is achieved using $\delta=30$ ns and $f=0.3$.

The obtained digital resolution for the 1.332 MeV line is 1.9 ns

²For the signal processing of the fast plastic signals see §4.9.

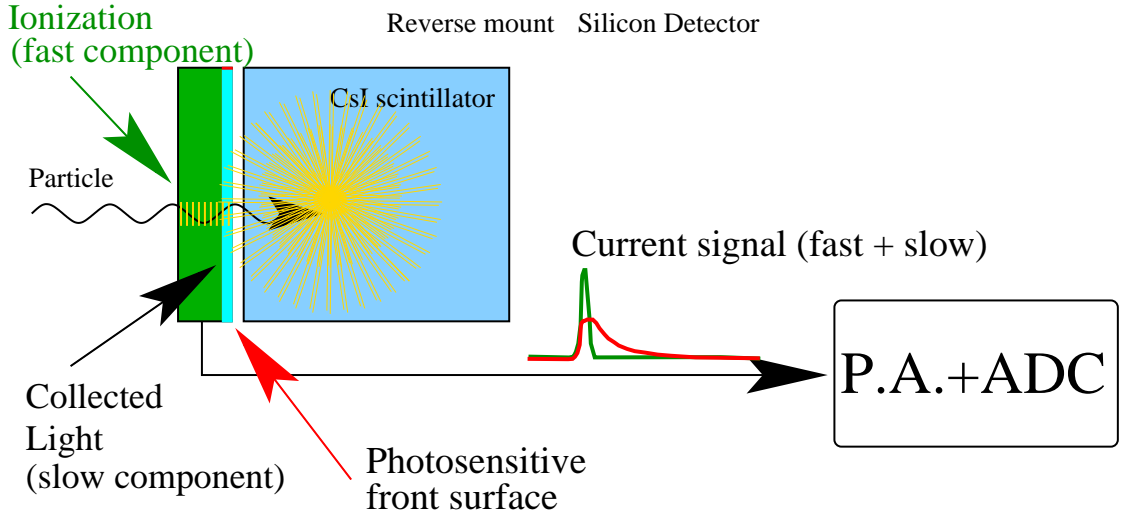


Figure 4.15: Principle of operation of a single-chip telescope detector as proposed in [58]. The silicon acts as a photodiode for the CsI(Tl) scintillator and thus only one acquisition channel is required for a full pulse shape analysis.

FWHM, to be compared with its analog counterpart of 3.2 ns FWHM.

The superior performances of the digital sampling system can be traced back to the zero-crossing algorithm used: the cubic interpolation method employed (§3.4.1) uses four samples for the determination of the zero-crossing, so that the whole information available ~ 20 ns before and after the zero-crossing is used. On the contrary, the wide band analog system uses only the information near to the zero-crossing, and thus it is more sensitive to high-frequency noise, finally worsening the achievable resolution.

The presented result has been restricted to a very small dynamic range (few keV near the 1.332 MeV line). More tests are planned in order to check the performance of the system (both hardware and software) over a wider dynamic range.

4.7 Pulse shape in single-chip telescope

In [58] a composite detector made of a silicon and a CsI(Tl) scintillator was proposed, the single-chip telescope (SCT). Its principle of operation is shown in Fig. 4.15.

The telescope is built using a silicon and a CsI(Tl) (similar to the ΔE - E application discussed in §4.1), with the silicon mounted

in a reverse field configuration (like in §4.3). The silicon detector is required to have a photosensitive “front” surface (i.e. the side facing the CsI).

Low-energy particles are stopped in the silicon detector, and they can be identified using exactly the method described in §4.3. More energetic particles undergo an energy loss in the silicon detector (“ionization” or fast component) and are stopped in the CsI, where light is produced (slow component). Due to its photosensitive front surface the silicon detector acts as a photodiode and collects the light coming from the scintillator. The final result is a single output signal that is composed of two components, a fast one due to the particle energy loss in silicon and a slow one due to scintillation in CsI. From the experimental point of view, this detector is characterized by being compact, by requiring only one acquisition channel and by good resolution capabilities due to the use of a silicon detector. It is thus an attractive device that can be used for example as ancillary detector for light charged particle detection in large experiments.

This detector has been proposed and tested in [58] using an analog electronic chain similar to the one in Fig. 4.3(a).

A digital acquisition of this detector can be carried out with an electronic chain like Fig. 4.3(b), i.e. by simply connecting the detector output to the sampling AD system. For particles that are stopped in the silicon detector no slow CsI component is present, and thus the same digital analysis of §4.3 can be carried out, achieving the same identification performances of Fig. 4.6. For particles stopped in CsI a fast-slow pulse shaping analysis similar to what discussed in §4.2 can be performed. The signals have been processed with a baseline subtraction (§3.3.2) followed by two different digital semigaussian shaping filters (§3.3.3) with 700 ns and 2 μ s time constants. The signal processing method used is thus very similar to the one used for fast-slow pulse shaping identification in CsI (§4.2).

The obtained results are shown in Fig. 4.16(left), whereas in Fig. 4.16(right) an expanded view of the same dataset is shown to better appreciate the isotopic resolution for low- Z particles. A single AD converter has been used for the acquisition of the SCT signals, thus covering with a single electronic channel the whole dynamic range of the detector.

Full charge resolution is present for all the particles that were available in the “LNL test”, whereas isotopic identification is available up to $Z \lesssim 7$.

The vertical separation between two isotope identification lines in Fig. 4.16 amounts to few Fast-Component units (using the arbitrary units of the figure), whereas the full range is about 600. The resulting

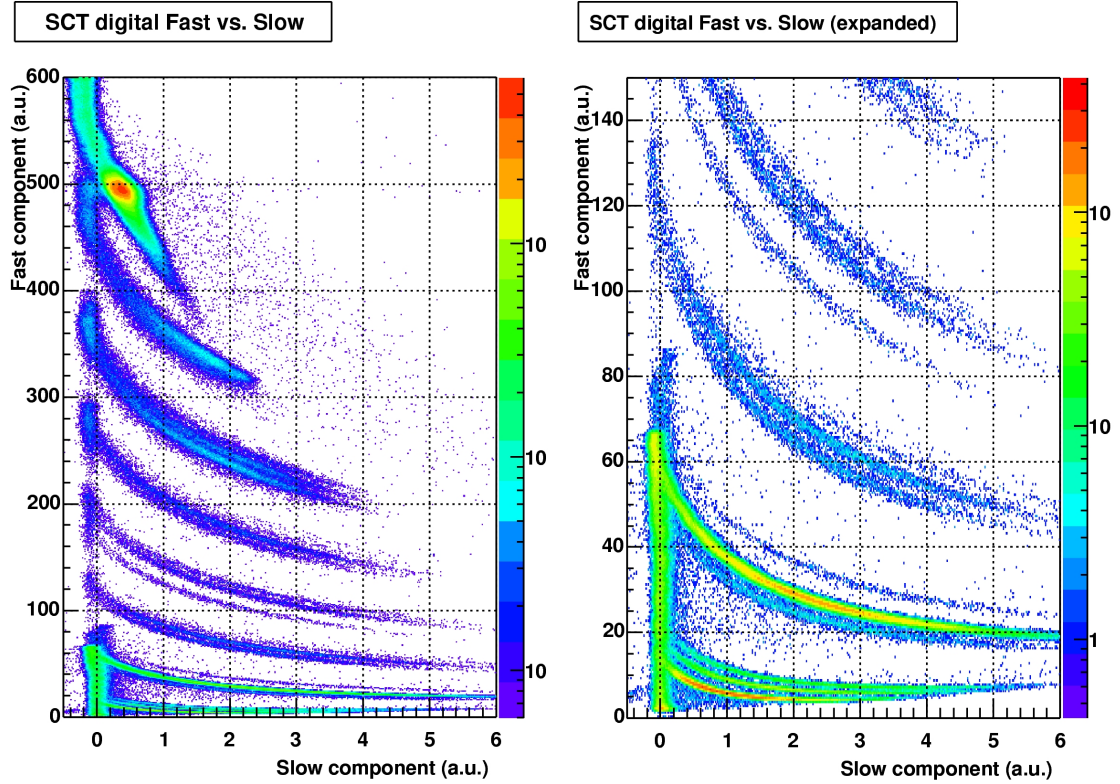


Figure 4.16: Identification plots obtained with digital signal processing of a single-chip telescope detector. Left: fast versus slow correlation, Right: expanded view. A single AD converter has been used to extract the whole dataset.

dynamic range requirement of the detector for isotopic identification is about 100–300, that is easily met given the AD converters used. The noise contribution due to the AD converter is negligible with respect to the detector noise and thus it is possible to conclude that the identification performances in this application are mainly limited by the detector characteristics.

4.8 Position using gas PSPPACs

As described in §1.2, gas detectors are used in various experiments, especially when the coverage of large surfaces is needed. An experimental applicability test of digital sampling techniques to a Position Sensitive Parallel Plate Avalanche Counter (PSPPAC, used in the ex-

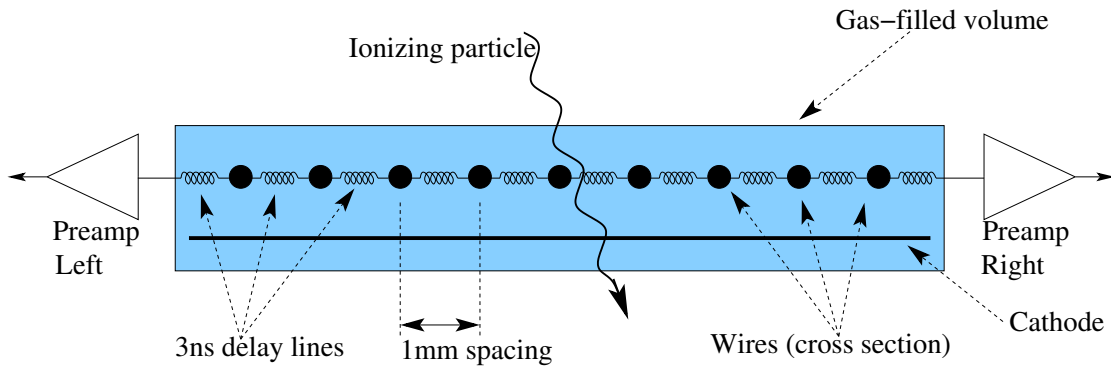


Figure 4.17: Principle of operation of a PSPPAC detector. The current pulse generated on the wires by the primary ionization is delayed before being amplified, so that the time difference between the left and the right pulses is related to the position of the initial interaction.

periment FIASCO [15]) has been performed; a schematic view of the detector principle of operation is shown in Fig. 4.17.

The detector is built using a number of parallel wires that are stretched inside a volume filled with low-pressure heptane gas, creating a planar grid. A bias voltage is applied between the wires and the cathode plane, which is usually made of a thin conductive foil. The ionization track due to a charged particle creates a number of electron-ion pairs and a current signal is induced on the detector wires (see §1.2.3). Due to the geometrical structure of the electric field, the signal is practically collected only by the two closest wires to the particle track, so that the position information is retained in the charge collection process. Each wire is electrically connected to its neighbours using a small-size delay line (3 ns long in Fig. 4.17) and the two ends of the chain (left and right in the figure) are connected to fast preamplifiers. Typical signal durations are of the order of few ns. Once the signal is collected it splits into two almost equal parts that travel in opposite directions until the preamplifiers are reached. Depending on the initial position a different number of delay lines is encountered so that the time difference between the two final pulses is a direct measure of the initial position of the incoming radiation. In order to achieve 2-dimensional position sensitivity, a second grid of wires is placed with a wire direction perpendicular to the first one, and using an identical electronic readout. The final achievable position resolution of this detector type is thus of the order of the wire spacing, that is 1 mm in Fig. 4.17.

The analog electronic chain used to process the four signals (two

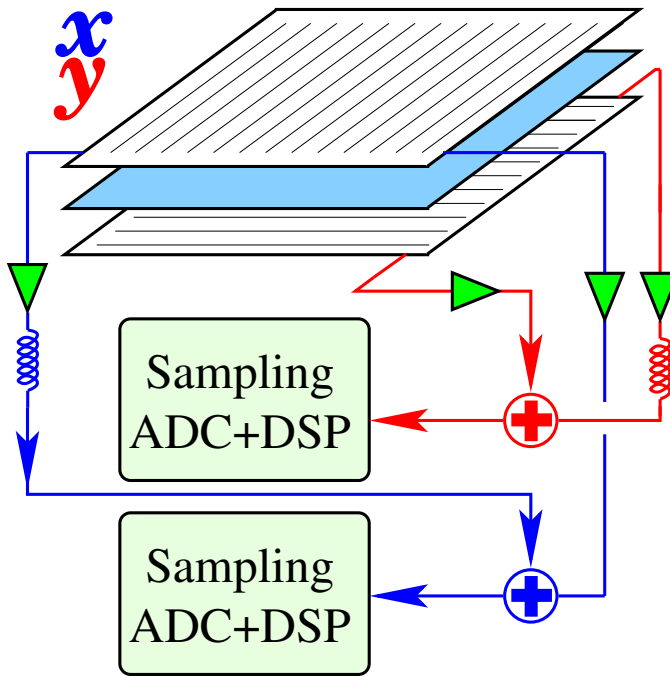


Figure 4.18: Digital setup used for the digitization of a PSPPAC as in Fig. 4.17. See text for details.

along the “*x*” and two for the “*y*” direction) consists usually of four Constant Fraction modules (one for each signal) that are connected to two Time to Amplitude converters.

In Fig. 4.18 a digital setup used for the acquisition of these detectors is shown. Two digitizers are used, one for each direction (*x* or *y*) of the detector; for each direction one of the two signals (for example the “left” one) is directly fed into the digitizer. The second preamplifier output (here the “right” one) is delayed for an amount of time longer than the maximum expected delay between the two signals and analogically summed to the first one. With this configuration the typical converted sequence $S[k]$ of each AD converter consists of two pulses (the “left” and the “right” one for the considered direction) separated by a time amount that is much greater than each pulse width. The time difference between these two pulses, apart from a known constant value (i.e. the delay introduced for the second line), gives the desired position information. With this configuration no synchronization is needed between the various ADCs, because a single converter is used to extract all the relevant information from a given direction of the detector (*x* or *y*), thus providing a very straightforward implementation of the measurement.

It is possible to extract the time difference between the two pulses

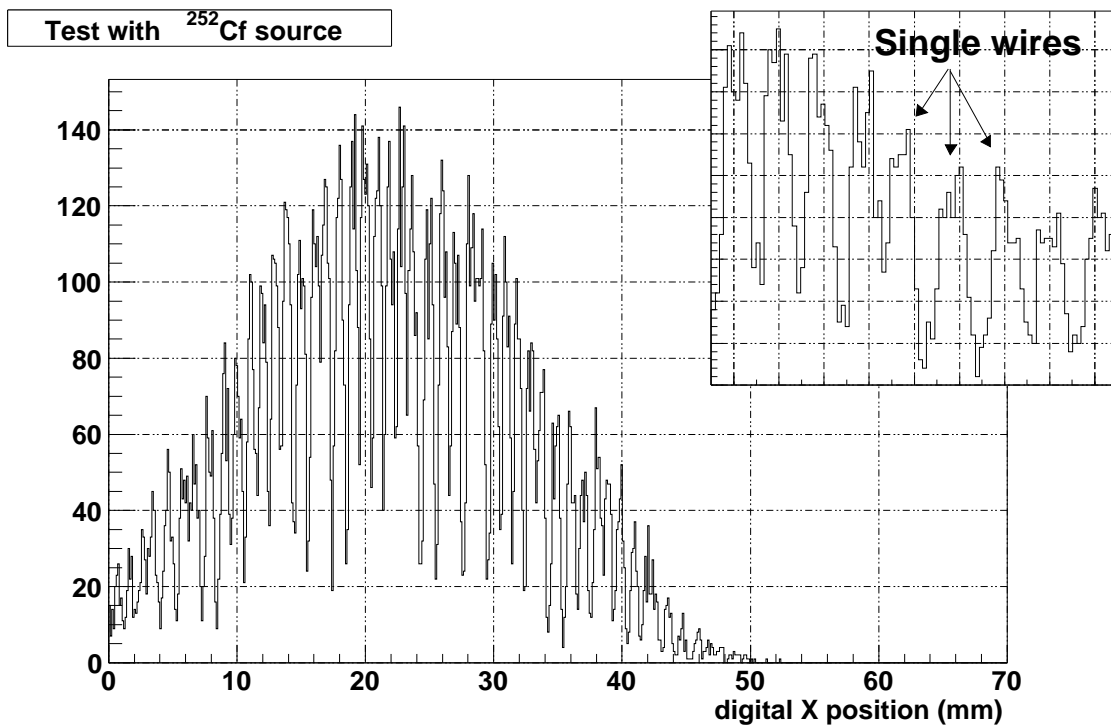


Figure 4.19: Results obtained using an uncollimated ^{252}Cf source with a digital sampling system. The single wire resolution obtained with the digital method is shown in the inset.

using a simple generalization of the dCFD algorithm presented in §3.4.2. An experimental test has been carried out using an uncollimated ^{252}Cf source and the relevant results are presented in Fig. 4.19. Only the x direction of the detector has been shown (similar results have been obtained for y).

It is possible to appreciate from the figure inset that a single wire resolution is achieved using the proposed digital approach, i.e. the position resolution is limited by the intrinsic detector properties, whereas the digital sampling approach gives a negligible contribution.

4.9 Timing using fast plastic scintillators

One of the most performing detection systems to be used in coincidence timing measurements is obtained using fast plastic scintillator (see also §1.2.2). The light emission following a particle detection is characterized by being of very short duration (in some cases less than

~ 2 ns decay time), thus allowing coincidence measurements with a very high-resolution (an ultimate timing resolution of about 10–30 ps can be reached with special care). Fast plastic scintillators are often used in applications where a precise timing reference is needed regardless of the amplitude information (these excellent timing properties come at the expense of a modest light emission efficiency and thus poor energy resolution).

A standard analog method for processing the output of these detectors is the use of a Constant Fraction module (CFD, see §1.2.8). An alternative method is the “first photoelectron timing” (FPET, [59, 60]), where a discriminator is used with a detection threshold low enough to be sensitive to a single photoelectron signal. This allows triggering on the first photoelectrons produced by the scintillator-phototube system that, as it can be theoretically shown, is characterized by very good timing properties. Several classic papers in the literature (for example [61, 62, 63, 64]) deal with the optimal choice of the experimental methods and parameters to achieve the highest-resolution timing measurements.

Given the very short duration of this detector output (few ns) with respect to the sampling period of the used AD converter (10 ns), much of the timing information encoded in the original signal is lost in the sampling process (due also to the analog antialiasing filter), so that a timing resolution comparable with the analog system is expected to be difficult to achieve. Although referring to a quite different case, this general trend is shown also in the simulation of Fig. 3.21, where the digital timing resolution of a 100 MSamples/s converter deteriorates rapidly for very fast signals.

An experimental test has been carried out in order to verify these assumptions and to compare the timing performance of the digital system with a standard analog one, using the electronic chain shown in Fig. 4.20. A ^{60}Co source is used and the time coincidence between the two cascaded γ rays is measured using two fast plastic detectors. The two photomultiplier outputs are directly connected to two digital acquisition channels, that have been synchronized using the same method discussed in §4.6 (we remind the reader that this setup is feasible only when few channel are involved). A simultaneous measurement using a standard analog electronic chain is performed using two CFD modules and a Time to Amplitude (TAC) converter.

The timing information has been extracted from the digitized sequences using a dCFD-like algorithm (§3.4.2), modified in order to use the absolute maximum of the signal instead of its (missing) “asymptotic amplitude”; both cubic and “penta” (§3.4.1) interpolation methods have been tested. A dArcCFD (§3.4.3) algorithm has also been

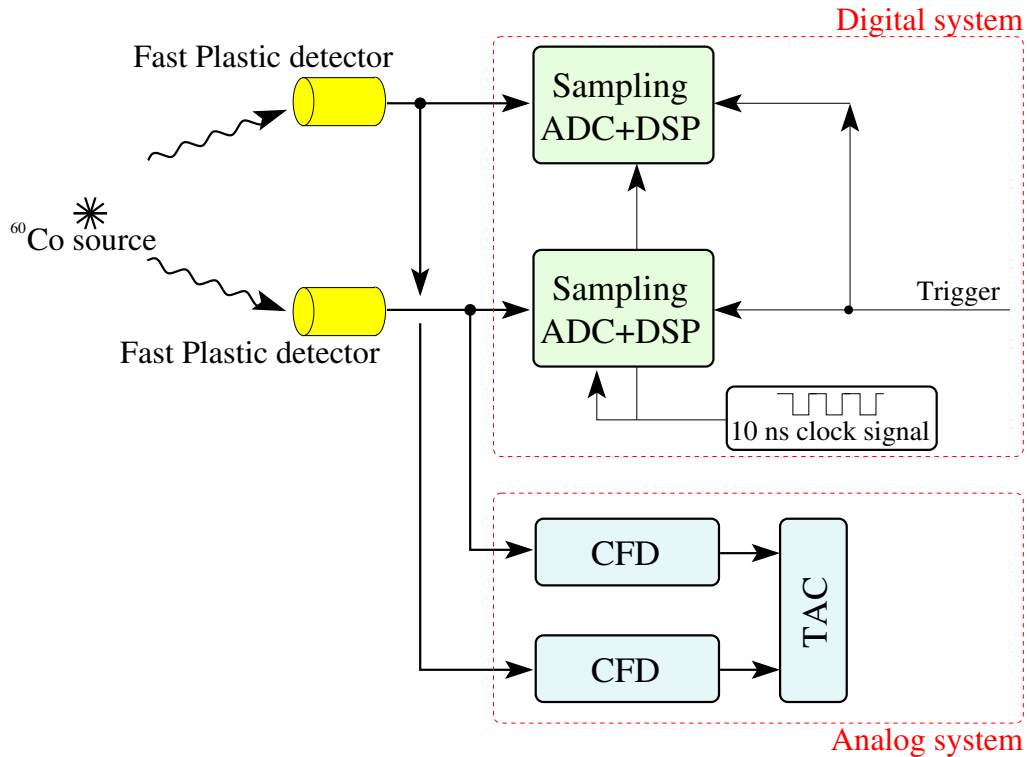


Figure 4.20: Electronic chain used to perform a coincidence timing resolution comparison between the digital system and its analog counterpart. The two ADCs are synchronized using the same clock source and the same trigger.

tested, providing almost the same results than the dCFD one.

The obtained results are shown in Fig. 4.21. As anticipated, the timing resolution achieved with the 10 ns digital sampling system (~ 400 ps FWHM) does not reach the same performance level of its analog counterpart (~ 200 ps FWHM). The fact that changing the digital timing algorithm and/or the interpolation procedure does not significantly influence the final results can be regarded as an evidence for the loss of useful information in the sampling process, that cannot be properly recovered with the used algorithms. For example the application of FPET-like methods is not possible, because the fast single photoelectron response is convoluted with the much slower anti-aliasing filter response, so that the fast timing information encoded in the original signal is lost.

The final digital resolution of 430 ps FWHM (i.e. the time difference between two dCFDs) is in fair agreement with the predictions of Fig. 3.21, taking into account that the impulse response of the used

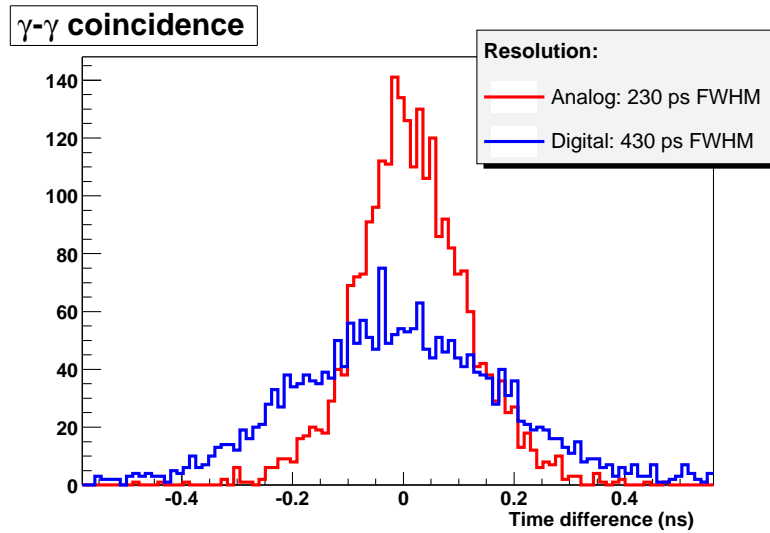


Figure 4.21: Comparison between the timing results obtained with analog and digital (with 10 ns sampling period) systems using fast plastic scintillators (about 2 ns decay time). See text for details.

antialiasing filter is characterized by a ~ 30 ns risetime.

4.10 Timing using NaI(Tl)

A similar test to the one described in the previous section has been performed using a NaI(Tl) scintillation detector. This scintillator is characterized by a large scintillation light output (although generally lower than CsI), with a decay time of the order of ~ 250 ns (faster than CsI). This material thus finds application where a compromise between good energy resolution and good timing properties is needed using a single scintillator.

An electronic chain similar to the one described in §4.9 (shown in Fig. 4.20) has been used, except for a standard $2'' \times 2''$ NaI(Tl) detector replacing one of the two plastic scintillators. With this configuration the timing properties of the slow scintillator can be simultaneously tested with both analog and digital means, using the output from the fast plastic scintillator as a reference time.

The preliminary obtained results are shown in Fig. 4.22. The achieved resolution (for $E > 600$ keV) with both signal processing methods is ~ 1.5 ns FWHM, with the analog chain giving a slightly better resolution.

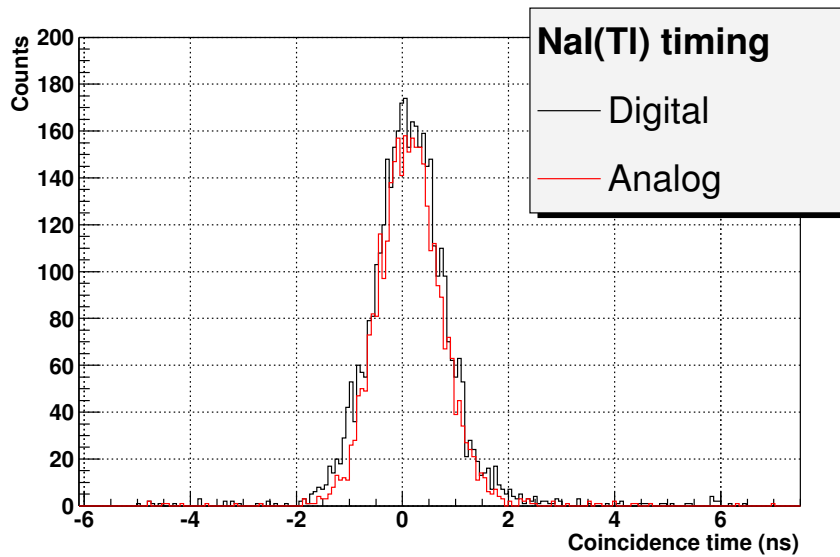


Figure 4.22: Results of a test performed using an electronic chain similar to Fig. 4.20, but using one NaI(Tl) detector.

Further work is in progress (mainly using simulations) in order to understand whether the observed timing resolution is dominated by the intrinsic detector properties (mainly photoelectron statistics) or by the used electronics. The possibility of applying First PhotoElectron Timing (FPET, see §4.9) methods is under study, although, due to the limited bandwidth of the used AD conversion system, these methods do not have a straightforward application when using digital signal processing techniques.

4.11 Pulse shape in phoswich detectors

The use of a stack of two different scintillation materials optically coupled to a single photomultiplier tube (PMT), known as phoswich detector (for implementations involving CsI(Tl), see [65, 66, 67]), is a standard method for light charged particle identification. In the FIASCO [15] experiment a non-standard three-layer phoswich configuration has been developed and used in order to extend the detection range up to $Z \simeq 20$. The used detector is shown in Fig. 4.23.

This configuration uses three different scintillators (BICRON BC404, BC444, and a CsI(Tl) crystal) coupled to a single PMT; the corresponding fluorescence decay times are equal to 1.8 ns, 180 ns and

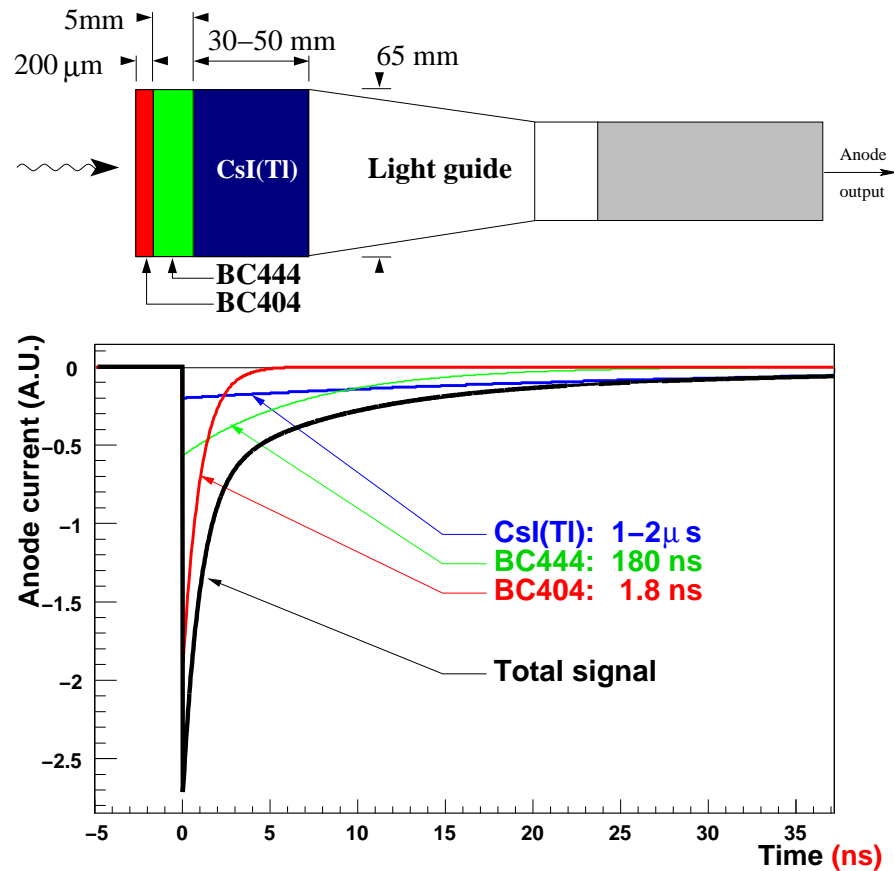


Figure 4.23: Geometrical characteristics of the phoswich detectors described in the text. A schematic representation of the detector output, that is made of three components, is also presented.

$\sim 2 \mu\text{s}$ respectively. Thus the anode output signal of this kind of detector results from the sum of three signals, their relative amplitudes being determined by the energy loss of the impinging particle in each scintillator. The shape of the current pulse then reflects the type of the detected particle and can be used for identification purposes.

The study of this detector type using digital sampling methods has been already presented in detail in [1, 2], and it is thus only briefly reviewed here.

The usual analog approach consists of an integration of the anode signal at different times, using standard charge integration modules (QDC): a proper choice of integration widths and delays with respect to the start of the current pulse (i.e. a Constant Fraction time-mark) permits to obtain three quantities (usually indicated as Gate A,

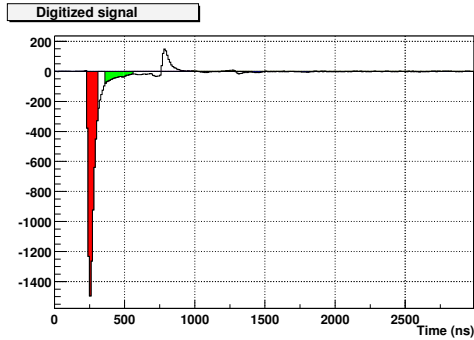


Figure 4.24: Digitized signal from a phoswich detector. This relatively fast signal corresponds to the detection of a heavy particle ($Z \sim 6$). The presence of an impedance mismatch is also apparent.

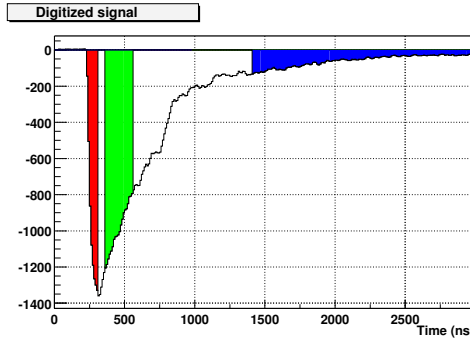


Figure 4.25: Digitized signal from the same detector of Fig. 4.24, but corresponding to a light charged particle ($Z \sim 1$). The same integration gates of Fig. 4.24 are also shown.

Gate B, Gate C) that are related to the energy loss of the particle in the three scintillators. Typically adopted values for the width W and the delay D of the three gates are: $W_A = 50$ ns, $D_A = 0$ ns, $W_B = 250$ ns, $D_B = 250$ ns, $W_C = 1000$ ns, $D_C = 1000$ ns.

This analog method has a very simple counterpart using digital signal processing techniques, i.e. the digital integration of the signal (see §3.3.4) at different times. The digital implementation is characterized by a much greater electronic simplicity (only one AD converter is needed) with respect to its analog counterpart (3 QDCs and 3 Gate and Delay Generators); more details can be found in [1].

As an example in Fig. 4.24 and Fig. 4.25 two digitized signals from the same detector are shown, together with a representation of the digital integration gates used. The pulse shape properties of the detector are evident.

From the correlations between the three gates (Gate A vs. Gate B, Gate B vs. Gate C) the desired identification can be achieved.

An alternative digital approach is the use of the lookup table method already presented in §3.5: this method allows the extraction of the phoswich signal information by taking into account the peculiarities of each detector. More details are discussed in [1, 2].

The achieved identification performances are shown in Fig. 4.26. It is possible to appreciate that the identification performances of the digital sampling systems (with both digital integration and Lookup

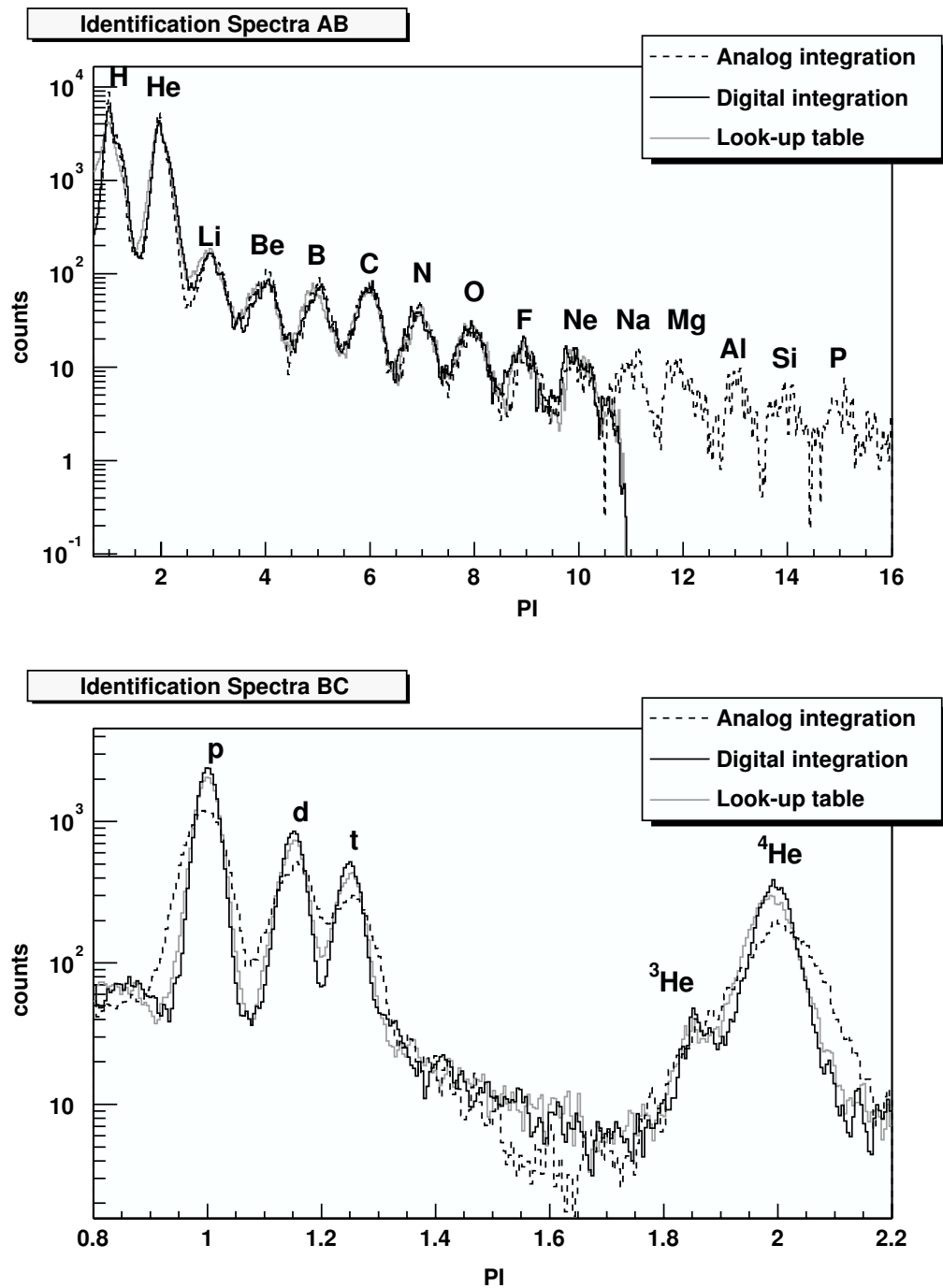


Figure 4.26: Identification spectra obtained by linearizing the correlations Gate A vs. Gate B and Gate B vs. Gate C for analog and digital integrations and Lookup Table methods.

table methods) are of about the same quality than the analog ones for the Gate A vs. Gate B results, whereas a significant improvement is achieved in the Gate B vs. Gate C identification spectra.

These results, taking also into account the much simpler digital electronic acquisition chain with respect to the analog one, make the digital approach method very appealing for replacing the analog system in applications to large experimental setups.

Chapter 5

Simulation of silicon current signals

In this chapter a detailed simulation of the current output from silicon detectors is presented. After a description of the main experimental results that motivate the study of these detectors and a brief review of solid-state detector properties, the proposed approach is presented. The numerical implementation chosen is thus described as well as its preliminary results. The discussion focuses on silicon detectors only, although it can be easily extended to other semiconductor materials as for example germanium.

The simulation of silicon detectors is an active research field also in other physics areas, for example in High-Energy Physics, mainly referring to silicon strip or pixel detectors. Similar methods with respect to the one proposed here are used, although, due to low specific ionization densities involved in such experiments, the Coulomb interaction between holes and electrons, which is the main and original feature of the approach presented in this chapter, is neglected.

5.1 Pulse shape in silicon detectors for HI experiments

As discussed in §1.2.4, silicon detectors are characterized by good energy resolution and timing properties, so that they are often used in charged particle detection systems (as the ones needed for the studies described in §1.1). A typical experimental configuration is the use of ΔE - E methods (discussed in §4.1) using a silicon as ΔE detector (with transmission mounting). With such a configuration the total energy of the incoming particle – if stopped in the E detector – can be obtained

from the sum of two measured energies (i.e. ΔE and E^1), whereas a high-resolution time of flight information (that is often needed) can be extracted from the silicon signal. By exploiting the dependence of energy loss on the particle type, charge and (possibly) mass identification can be obtained using a ΔE versus E correlation, as discussed in §4.1 (see also Fig. 4.2). This simple detector configuration is thus characterized by the ability of obtaining different quantities using only two detectors and a proper electronic setup, either employing analog electronics or digital sampling techniques. The particle identification threshold of this system, i.e. the lowest particle energy that allows an (isotopic) identification, is determined by the need of having a non-zero signal in the E detector. This means that low energy particles that are stopped in the silicon detector cannot be identified with this method.

Apart from using different detection configurations, a possible solution to this problem is to exploit the dependence of the current signal shape from the charge (and mass) of the detected particle (see §1.2.5, §4.1, [51]). In Fig. 5.1 a schematic view of the experimental arrangement is shown.

In the standard silicon mounting (top of Fig. 5.1, see also §5.2) particles enter the detector from the high electric-field side. Electrons and holes produced in the ionization wake are collected by the macroscopic electric field, and the collection time of the whole ionization column is related to the range of the particle by means of two principal mechanisms:

Ionization density

For a given total kinetic energy the specific ionization produced by a heavy charged particle (i.e. short range) is higher than the one produced by a light charged one (i.e. long range). The created space charge can be high enough to partly shield the macroscopic applied electric field, so that the required time to collect the charges becomes longer (this effect is known in literature as “plasma delay” or “plasma erosion time”). This effect is more important for low-range (high specific-ionization) particles and for low macroscopic electric-field regions.

Bragg-peak position

For a given total kinetic energy short-range particles have a Bragg peak (that is the area giving the greater contribution to the final

¹To be strictly correct the energy measured from the “ E ” detector is the residual energy of the particle and not its full energy, so that the term “ $\Delta E-E$ ” method is slightly misleading.

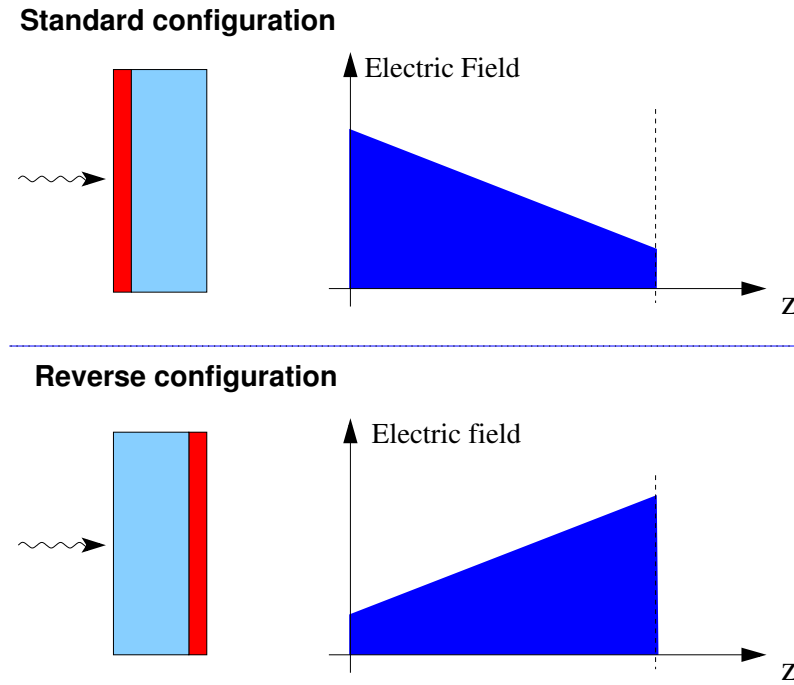


Figure 5.1: Top: standard silicon configuration with the high electric-field part of the detector facing incoming particles. Bottom: reverse mounting configuration, where particles enter the detector in the low-field part. See text for details.

current signal) localized in the high field region.

These two mechanisms have opposite influence on the final signal pulse shape, generally leading to compensation effects and thus finally reducing their effects on the detector pulse shape. Pulse shape analyses on front mounted silicon detectors are thus usually unfeasible, although some applications exists [55].

This compensation effect can be eliminated using the silicon detector in a reverse mounting configuration [52, 53] (bottom of Fig. 5.1). Particles are now entering from the low electric-field side of the detector so that both the aforementioned effects contribute to increase the pulse shape dependence on the particle type. It has to be noted that good energy and timing resolution are required for this kind of application, as well as a good uniformity of the chosen detector, see §4.3 and [54].

An original example of this application using digital sampling techniques has been described in §4.3 (see Fig. 4.6), whereas in Fig. 5.2 results obtained using analog methods with a small area detector are

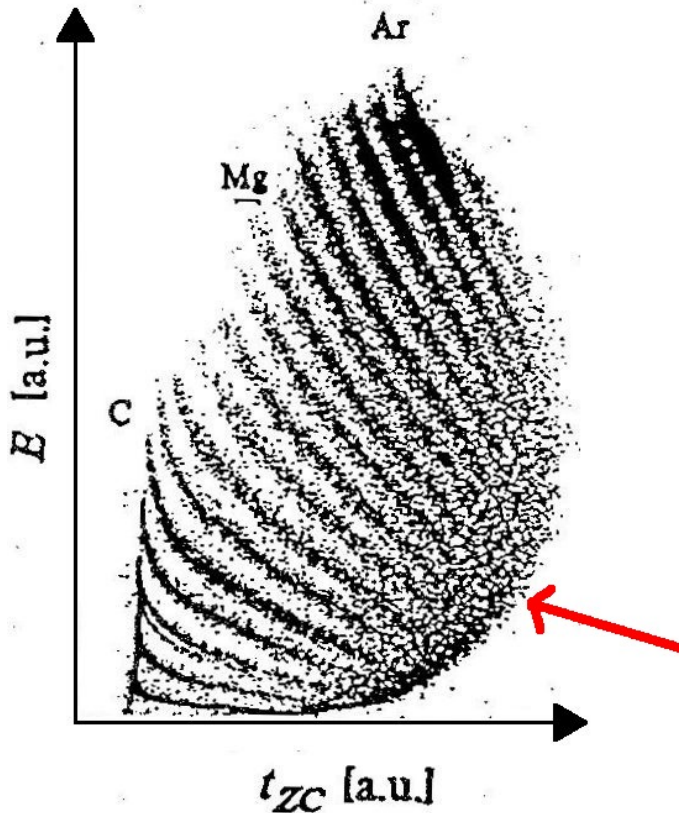


Figure 5.2: Pulse shape results (adapted from [54]) using analog methods with a small area reverse mounted silicon detector. Charge identification over a wide dynamic-range is apparent. The “backbending” region is indicated by the solid arrow.

shown (from [54]). Though obtained with different methods and operating conditions, both figures exhibit the same features, notably good identification properties (mainly in charge) for high-energy particles, whereas the identification threshold is limited by a “backbending” of the isotopic lines (see solid arrow in Fig. 4.6). After the backbending point (about ~ 40 MeV for a ^{12}C ion in the experimental configuration used for Fig. 4.6) the identification lines collapse over a single curve, and thus identification is no more feasible (although, due to the finite experimental resolution, one cannot exclude a residual *theoretical* pulse shape dependence). The presence of a backbending can thus be regarded as an effect due to the detector physics, and not as an instrumental artifact. It corresponds to a sudden speed-up of collection

times for low-energy particles exploring the low field side of the detector. This effect is totally unexpected and deserves an investigation on its own. Another surprising experimental finding that has not yet been explained is the nearly independence of the “backbending energy”, i.e. the energy where backbending occurs, of the applied bias voltage to the detector (see [54] and §5.6)

The described backbending can be regarded as the ultimate identification threshold of the detector, and thus a detailed understanding of its properties is necessary. Nevertheless up to date no theoretical explanation has been found for this process in the literature. For example in [54] a possible explanation related to the plasma erosion effect is discussed, leading to contradiction to the experimental data. It is thus literally concluded that “... effort is necessary to understand the underlying physical effects.” [54].

In this Thesis a numerical simulation of the silicon detector signals has been implemented aiming at giving some insight into the processes that lead to the experimentally observed behaviour. Instead of using empirical or semi-empirical hypotheses on the plasma evolution, a computation starting from “first principles” (known semiconductor properties and electromagnetic interactions, see §5.3) is proposed and tested. As described in the following, the proposed simulation does not introduce free parameters for the description of the process, and thus, if successful, can be used to identify the physical processes responsible for the observed behaviour.

5.2 Semiconductors as solid-state detectors

A schematic view of the principle of operation of a silicon detector is shown in Fig. 5.3; a general description of semiconductor devices can be found in many textbooks, as for example [36], and it is only briefly recalled here.

A silicon detector can in practice be regarded as a standard $p - n$ junction having a macroscopic size (with cross sections of few cm^2 and thicknesses of $100 - 500 \mu\text{m}$) with very different doping concentrations between the n and p type materials. While one of the two regions is heavily doped (the p^+ region in Fig. 5.3), the other one (the “bulk” in Fig. 5.3) is very poorly doped, i.e. often only the residual impurities from the silicon manufacturing processes are used as dopants. Due to the many orders of magnitude difference in doping concentrations, the applied bias voltage V_{bias} creates a depletion region that practically

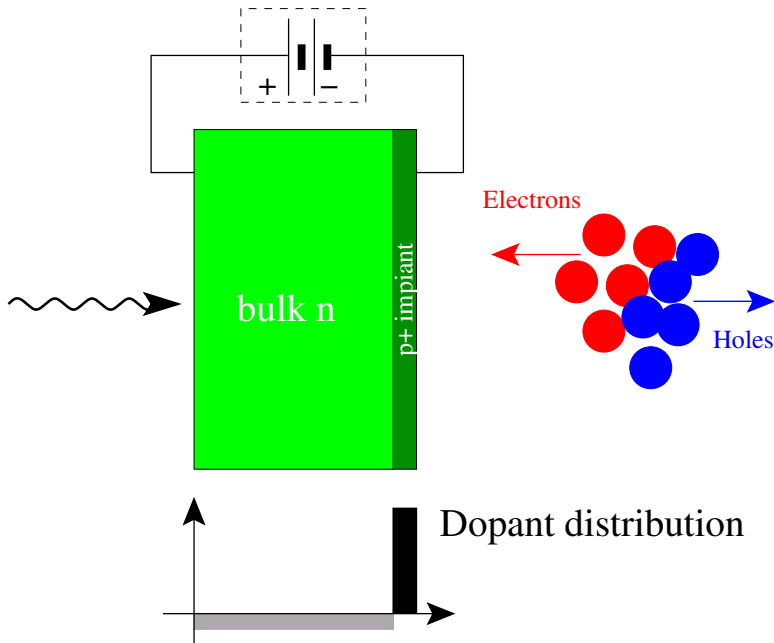


Figure 5.3: Schematic representation of a silicon detector (example with an *n*-type bulk detector). The applied bias voltage as well as the resulting motion of carrier are also shown.

extends only in the “bulk” volume of the detector. Using simplified hypotheses, the depletion region thickness d_{dep} is given by [14]:

$$d_{\text{dep}} = \sqrt{\frac{2\epsilon V_{\text{bias}}}{eN}} \quad (5.1)$$

where ϵ is the permittivity of silicon (equal to $11.9 \cdot \epsilon_0$, ϵ_0 being the permittivity of free space), e is the electron charge and N is the doping concentration of the bulk. One finds that d_{dep} is proportional to the resistivity of the bulk material. The “depletion voltage” of a transmission mounted detector is then defined as the bias voltage needed to have d_{dep} equal to the full detector thickness. Detectors are usually operated at voltages 10 – 100% greater than the nominal depletion voltage.

The electrons and the holes created during the ionization process in the bulk drift because of the presence of the macroscopic electric field. The resulting currents (taking holes as an example) are given by the following expressions (see for example [36]):

$$\vec{\nabla} \cdot \vec{j}_h + e\partial_t \rho_h = 0 \quad \text{continuity equation} \quad (5.2)$$

$$\vec{j}_h = -eD_h \vec{\nabla} \rho_h - e\rho_h \mu_h \vec{\nabla} V \quad \text{drift-diffusion equation} \quad (5.3)$$

where \vec{j}_h is the current density vector, D_h the diffusion coefficient, μ_h the hole mobility, ρ_h the numeric charge density, V the local value of the potential. Similar equations hold for the case of electrons. The carrier mobility is related to the velocity \vec{v}_h by the expression $\vec{v}_h = \mu_h \vec{\nabla} V$.

The quantities $|\vec{v}_h|$ and D_h (as well as $|\vec{v}_e|$ and D_e) are shown in Fig. 5.4 and Fig. 5.5 as a function of the electric-field strength (data from [68]). The carrier velocity exhibits an initial linear dependence on $|\vec{E}|$ (i.e. approximately constant value of D_h or D_e), whereas a saturation is reached for strong electric fields. This behaviour has to be taken into account for a detailed simulation of silicon properties. For example, in a $300\text{ }\mu\text{m}$ silicon detector with 120 V depletion voltage operated at 140 V (as the configuration used in the experimental tests of §4.3) an electric field of $\sim 4 \cdot 10^5\text{ V/m}$ is reached, thus giving a hole mobility about 12% lower with respect to the low-field case.

5.3 Key factors affecting silicon pulse shapes

A solid-state detector is a complex microscopic system: a periodic lattice of crystalline material is present where, due to the low band gap, electrons can be promoted, by various mechanisms, from the valence to the conducting band, so that at finite temperature an equilibrium non-zero carrier concentration is present. The absence of an electron in the lattice structure can be regarded as the presence of a fictitious positive charged particle, the hole, that can be accurately treated as a real particle with properties similar to the electron. A relevant energy loss mechanism for electrons and holes are lattice interactions, that produce the viscosity regime leading to the charge drift as well as the velocity saturation effect seen in Fig. 5.4. Energy is given to the lattice in the form of vibrations, that in turn can be treated as interacting quasi-particles, the phonons. The system is perturbed by the ionization produced by the detected particle: a relevant amount of free charge is produced that drifts under the electric-field action toward the collecting electrodes, apart from recombination effects.

Given this microscopic scenario, it is important to understand what are the key factors affecting silicon pulse shapes, in order to give a description as simple as possible of the underlying physical effects. A quantitative estimate can be obtained by considering, for example, the case of the detection of a $40\text{ MeV }^{12}\text{C}$ ion. Given the range of $\sim 45\text{ }\mu\text{m}$ and with the hypothesis of an average ionization transverse radius of the order of few μm [69], the parameters reported in the following table are estimated:

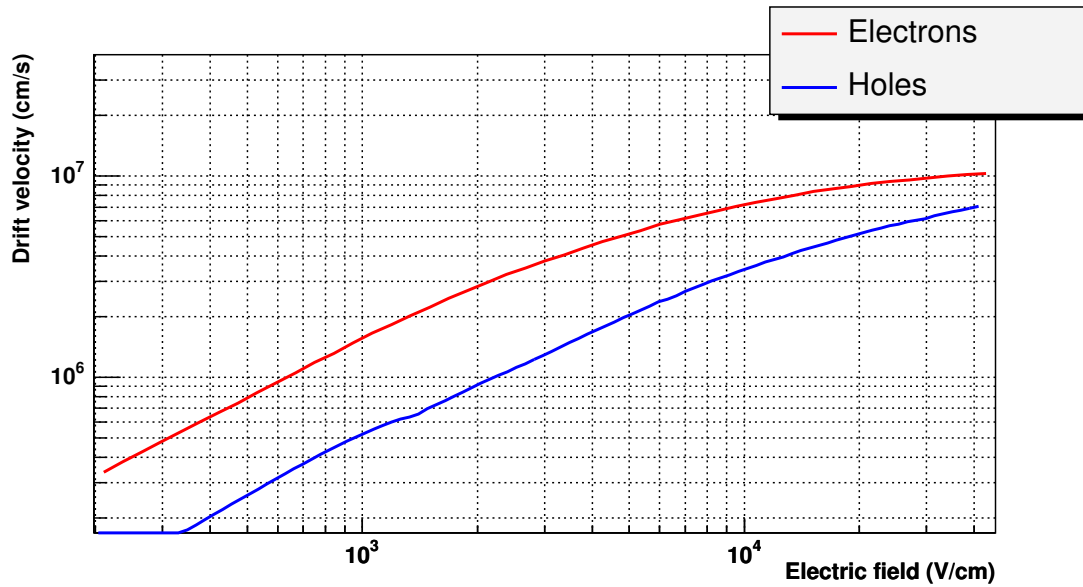


Figure 5.4: Velocity of electrons and holes in silicon at room temperature (data from [68]). Note the logarithmic axes.

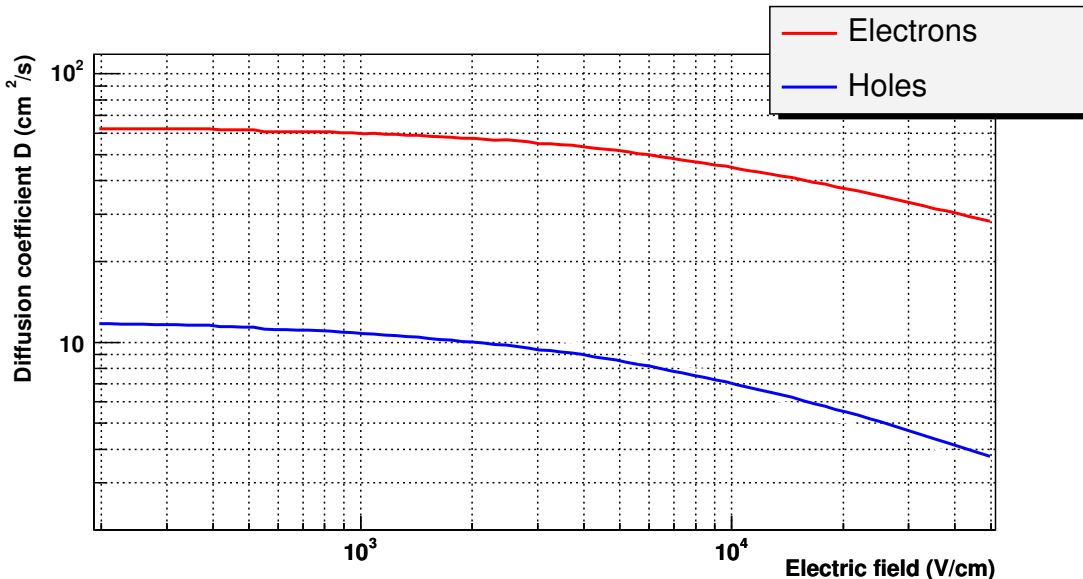


Figure 5.5: Longitudinal diffusion coefficient of electrons and holes in silicon at room temperature (data from [68]). Note the logarithmic axes.

Silicon	Energy for electron-hole pair Bulk doping-concentration Average distance between Si atoms	3.6 eV 2×10^{13} cm $^{-3}$ 0.27 nm
^{12}C (40MeV)	Ionization-pairs number	1.1×10^7
	Ionization-pairs density	7.8×10^{16} cm $^{-3}$
	Average distance between ioniz. carriers	18 nm
	Average linear ionization density	8.9×10^5 eV/ μm
MIP	Ionization-carriers number	2.2×10^4
	Average linear ionization density	2.6×10^2 eV/ μm

For the sake of comparison, the values corresponding to the detection of a Minimum Ionizing Particle, MIP, in a 300 μm detector have been reported, see discussion later.

The number of carriers generated in the ionization wake of ^{12}C is so large to suggest a schematization of the created space charge as a continuous function, i.e. without considering the individual electron and hole behaviour inside the crystal.

It is well known that the electric field inside the semiconductor junction is due to the fixed charge density that is present in the depletion region, given by the bulk doping concentration. Since the injected charge density is much greater than bulk doping, the electric field inside the detector is severely perturbed by the detection of the particle.

In principle the presence of many carriers inside the detector might alter the drift or diffusion properties of electrons and holes, due to additional carrier-carrier (possibly phonon-mediated) interactions, that translate into a deviation from the low ionization density measurements reported in Fig. 5.4 and Fig. 5.5. Usually this effect can be excluded, for example due to the fact that the average linear distance between ionization carriers is still much greater than the average linear size of a silicon crystallographic cell. Thus each carrier does not “see” the presence of the others during its drift motion (except for Coulomb interactions), so that the low density measurements are adequate for our purposes.

These considerations lead to a description of the silicon detector where the continuum charge distributions ρ_h and ρ_e created by the initial ionization processes drift inside the detector in a classical way (i.e. without significant contributions from the interaction with the crystal lattice), except for the presence of a saturation velocity. The Coulomb interactions between the two charge densities as well as with the applied electric field are present and influence the carrier motion. The drift and diffusion of carriers can be treated using Eq. 5.3 and the experimental values of μ_h , μ_e , D_h , D_e that are presented in Fig. 5.4

and Fig. 5.5.

In the proposed approach the simulation of a silicon detector is thus separated (for each time t) in two problems: the electrostatic configuration, i.e. the computation of the electric field inside the detector taking into account the Coulomb interaction between electrons and holes, and the drift/diffusion motion of carriers inside the semiconductor under the action of the computed electric field. The recombination of electron-hole pairs has been neglected, because the related effects are expected to mainly influence the amplitude of the collected signals and not their time evolution.

It has to be noted that, as anticipated, the detection of MIP particles (see table at pag. 123) is characterized by a much lower ionization density than the one typical of a heavy charged-particle.

5.4 Formulation in the continuum

In the previous section it has been shown that, under hypotheses valid for the case of detection of heavy charged particles, the simulation of a silicon detector can be treated as an electrostatic problem where the two interacting charge densities ρ_h and ρ_e drift inside the volume of the semiconductor under the action of the total electric field \vec{E} .

This problem can be mathematically described with the following system of equations:

$$\left\{ \begin{array}{l} \nabla^2 V = -e[\rho_h - \rho_e + \rho_{\text{bias}}]/\varepsilon \\ \vec{j}_h = -eD_h \vec{\nabla} \rho_h - e\rho_h \mu_h \vec{\nabla} V \\ \vec{j}_e = +eD_e \vec{\nabla} \rho_e - e\rho_e \mu_e \vec{\nabla} V \\ \vec{\nabla} \cdot \vec{j}_h + e\partial_t \rho_h = 0 \\ \vec{\nabla} \cdot \vec{j}_e + e\partial_t \rho_e = 0 \\ \text{+ boundary conditions on electrodes and initial conditions} \end{array} \right. \quad (5.4)$$

where ρ_{bias} is the fixed charge density induced by the external bias voltage. The unknowns in Eq. 5.4 are thus the potential V , the charge densities ρ_h and ρ_e , and the current densities j_h and j_e . The detector contacts are supposed to be metallic, so that the value of the electric potential is constant on their surfaces. The detector under study is a planar detector. For common detector characteristics, the charge present on the detector surfaces (the detector can be treated as a capacitor), is several orders of magnitude greater than the ionization-related one, so that no difference exists in describing the detector ca-

pacitor between assuming constant charge or a constant voltage on it.

The current induced on the electrodes can be computed using the Ramo's theorem [70, 71], that, in the very simple planar geometry used, states that the induced charge $Q(t)$ at time t is given by:

$$Q(t) \propto \int_{\mathcal{V}} (\vec{j}_h + \vec{j}_e) \cdot \hat{e}_z \, d^3x \quad (5.5)$$

where \mathcal{V} is the silicon volume and \hat{e}_z is the unity vector orthogonal to the electrodes. The initial conditions for Eq. 5.4 are expressed in terms of ρ_h and ρ_e , i.e. the initial ionization densities, whereas $j_h(t=0) = j_e(t=0) = 0$ and $V(t=0) = V_{\text{applied}}$. No perturbation of the applied electric field is present at $t=0$, where $\rho_h(x, y, z, t=0) = \rho_e(x, y, z, t=0)$.

Equation 5.4 is thus a coupled system of partial differential equations having various non-linear terms that cannot be neglected, as for example the $\rho_{h,e} \vec{\nabla} V$ terms describing the carrier drift. The mobility and diffusion parameters are not constants, but depend² on the magnitude of \vec{E} , giving an additional source of non-linearity in the system.

Due to these difficulties, a simulation of the detector behaviour using Eq. 5.4 has not been considered and, on the contrary, a quasi-microscopic simulation has been implemented.

5.5 Quasi-microscopic simulation

The key factors to be included in the simulation have been discussed in §5.3, whereas in the previous section the difficulties associated with their formulation in the continuum (i.e. using Maxwell equations) have been presented.

A straightforward implementation of the simulation can be realized (at least in principle) by considering the single electrons and holes as charges moving within the detector with a velocity corresponding to the tabulated values of drift velocity in silicon. The electric field acting on a carrier k could be computed as:

$$\vec{E}_{\text{total}}^k = \vec{E}_{\text{applied}}^k + \frac{1}{4\pi\epsilon} \sum_{h=0}^N q_h \frac{\Delta \vec{r}_{kh}}{|\Delta \vec{r}_{kh}|^3} \quad (5.6)$$

+ electrostatic boundary conditions

With this simulation approach the computation at each time t reduces to the evaluation of Eq. 5.6 for each carrier k and to the drift

² Mobility and diffusion parameters depend also on the direction of the motion with respect to the crystallographic axes of the crystal, but this effect is not considered here.

of these carriers (that are “classical” particles) with the proper drift velocity.

A direct implementation of Eq. 5.6 cannot practically be performed due to the high number of carriers involved: using the 40 MeV ^{12}C example presented in §5.3 the evaluation of Eq. 5.6 using presently available personal computers would require about half a year for each integration step (assuming a 1 GHz machine with 30 ns computation time for each term of Eq. 5.6). It also has to be noted that the computation of the electric field and the subsequent drift for each carrier would provide details of the charge collection processes that are not relevant for the purposes of simulation of silicon current shapes.

It is possible to shorten greatly the required processing time by considering, instead of the motion of single carriers, the motion of *clusters* of carriers (for example having spherical shapes). The generated clusters do not have any physical interpretation, i.e. they are only mathematical entities used to reduce the complexity of the computation. The internal structure of each cluster is completely neglected, and thus a spherical cluster is completely defined given its position and velocity vectors, its radius and total charge. In order to maintain a good description of the Coulomb interaction between electron and holes, the two charge types are clustered independently, thus giving electron-only and hole-only clusters. If the number N_C of used clusters is not too low, a good approximation of the macroscopic behaviour of the space charge moving inside the detector can be expected, whereas the fine details about the charge distribution are not expected to be reliable.

The implemented quasi-microscopic simulation using charge clustering proceeds as follows:

1. The maximum number of clusters N_C and the integration time step t_{step} is fixed.
2. At time $t = 0$ the ionization track created by the desired ion is computed using standard energy loss tables [72] and N_C clusters are generated. An equal number of electron and hole clusters is produced in the tridimensional space, all having the same absolute charge. The cluster density reflects the energy loss of the particle, i.e. the higher cluster density is situated at the Bragg peak position. A loop is performed on all the clusters: once an intersection is found between two clusters of the same charge sign, their radii are reduced in order to remove the intersection. At the end of this process no overlap occurs between clusters of the same type (electron or hole), whereas intersections exist between positive and negative charges. Clusters located under

the Bragg peak region are thus characterized by a smaller radius with respect to average.

For each time step:

1. A computation of the electric field inside the detector is carried out, taking into account the “microscopic” electric field due to the electron-hole Coulomb interactions.

The problem of N_C bodies interacting with an $1/r^2$ force law is a common problem in gravitational simulations, and several numerical efficient methods can be found in the literature. Two of them have been tested: the Particle-Mesh-Particle method (PMP, [73]) and the Fast Multipole Method (FMM, [74]). In the PMP method the electric field is computed on a grid using the electric field generated by the single carriers (hence Particle-Mesh) and then the electric field on each carrier is computed interpolating the resulting mesh (hence Mesh-Particle). In FMM the space is recursively divided into sub-volumes according to the density of carriers: higher density means more sub-volumes. This hierarchical division allows a numerically efficient approximation of the electric field with a multipole expansion, that can be truncated to the desired order (more details in [74]). For this method an existing library [75] has been used. Both these methods assume to deal with point-like charges (or clusters in the present application), and therefore it is difficult to include in the formalism a finite size charge, as the spherical clusters used in the simulation. The assumption of point-like clusters does not allow the inclusion of the diffusion of the single microscopic carriers included in a cluster, which – on the contrary – could be introduced as a modification of the cluster size as a function of time. The use of point-like clusters it is thus practically equivalent to a zero-diffusion coefficient, that indeed gives results that are not in agreement with the experiment. Moreover, the speed gain of such methods with respect to a direct computation is relevant only for large N_C ($\gtrsim 10^5$, depending on the application), whereas for lower N_C values the speed gain may be too low to justify the increased program complexity.

In order to include in the simulation the finite size of clusters, a direct computation approach has been preferred. The computation of the electric field acting over the cluster k can then be computed using an expression similar to Eq. 5.6:

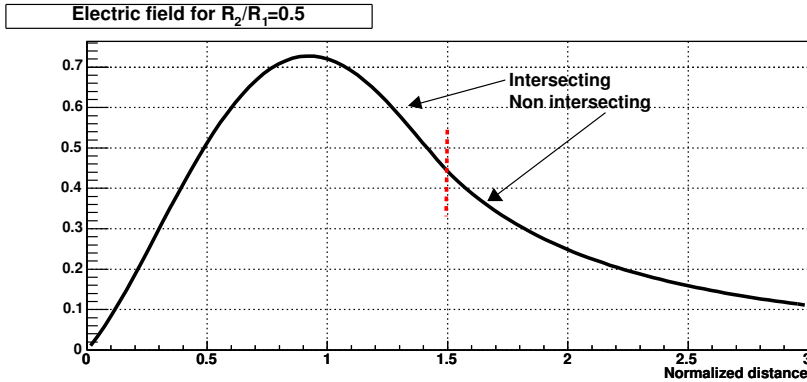


Figure 5.6: Example of the term $f(r; R_1, R_2)$ of Eq. 5.7 for the case $R_2/R_1 = 0.5$. For $r > R_1 + R_2$ the expected $1/r^2$ behaviour is obtained.

$$\vec{E}_{\text{total}}^k = \vec{E}_{\text{applied}}^k + \frac{1}{4\pi\epsilon} \sum_{h=0}^{N_C} Q_h \frac{\Delta \vec{r}_{kh}}{|\Delta \vec{r}_{kh}|} \cdot f(|\Delta \vec{r}_{kh}|; R_k, R_h) \quad (5.7)$$

+ electrostatic boundary conditions.

where N_C is the number of clusters used and Q_h is the charge of the h cluster. The factor $f(r; R_1, R_2)$ in Eq. 5.7 is a function of the inter-cluster distance r and of the radii R_1 and R_2 of the two considered clusters. When the two spherical clusters are non overlapping (i.e. $r > R_1 + R_2$) $f(r; R_1, R_2) = 1/r^2$, whereas for intersecting clusters a reduction factor is present. The function $f(r; R_1, R_2)$ has been estimated by an “ad-hoc” independent calculation, tabulated, and included in the computation: an example for $R_2/R_1 = 0.5$ is given in Fig. 5.6.

The boundary conditions for V (i.e. constant V on the electrode surfaces) have been taken into account using the method of mirror charges [76] applied to a two conductive planes configuration. It is well known that the required boundary conditions can be exactly obtained using an infinite number of mirror copies. As shown in Fig. 5.7 mirrors of the real clusters are built and placed into the mirror volumes. In the simulation only the first mirror copy on each side has been considered, so that the summation in Eq. 5.7 now runs over N_C “real” cluster and $2N_C$ “mirror” ones: the inclusion of more terms gives a negligible contribution to the final results, so that this approximation has been used.

2. Each cluster radius is increased during the current time step in order to approximately take into account the diffusion of car-

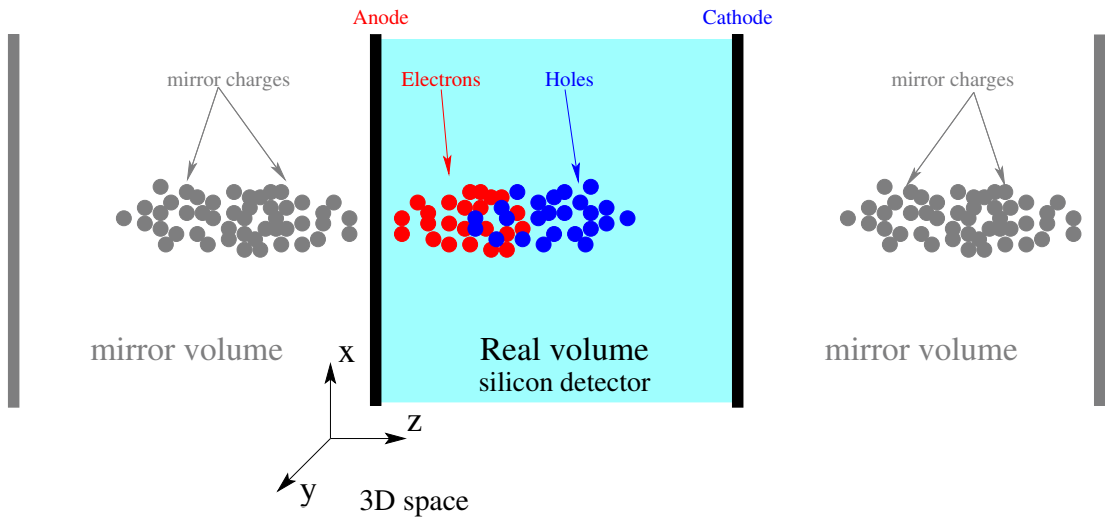


Figure 5.7: Configuration used for the microscopic simulation of output pulses from a silicon detector. See text for details.

riers inside the cluster. The radius R at time $t + t_{\text{step}}$ is given by $R^2(t + t_{\text{step}}) = R^2(t) + D \cdot t_{\text{step}}$ (the diffusion constants used are reported in Fig. 5.5).

3. For each cluster the drift velocity corresponding to the calculated local electric field is extracted from the tabulated values of Fig. 5.4. The cluster then moves for a time t_{step} with a velocity vector parallel to the computed electric field \vec{E} (a Runge-Kutta integration method has been used over contiguous time steps).
4. The induced current is computed using the Ramo's theorem as previously discussed.
5. Clusters that move outside the detector volume are considered as collected by the electrodes and removed from the cluster list. In order to improve the simulation accuracy, for each removed cluster a new cluster is created in the Bragg peak region, keeping the total remaining charge fixed.

The used simulation thus performs a full tridimensional computation of the charge motion and it can be easily adapted to various detector sizes and particle configurations (for example rear or front side injection).

The simulation has been implemented inside the Linux operating system using the C++ programming language. The most time-consuming step in the simulation is the computation of the electric

field using Eq. 5.7. Since it has an easily parallelizable expression, a parallel implementation of Eq. 5.7 has been carried out using the PVM [77] message passing interface. The data presented in the next section have been obtained using a setup consisting in 14 Linux machines with 2 GHz processors connected by standard GigaBit network interfaces.

5.6 Preliminary results

In order to test the simulation predictions, a comparison with the experimental results of Fig. 4.6 has been performed. The parameters describing the silicon detector used in the experimental tests of §4.3 have been introduced inside the simulation code. From the digitally collected data (see §4.3) the preamplifier response function has been extracted and used to convolve the current output signals produced by the simulation. The same digital signal processing analysis used in §4.3 have been performed on the simulated signals.

Before the comparison with the experimental results, it is instructive to study the simulated evolution of the plasma column, that is a useful though experimentally inaccessible quantity for understanding the detector behaviour. The data presented in this section have been obtained using a number of cluster $N_C = 5000$; higher values of the N_C parameter do not alter significantly the achieved results.

As an example, in Fig. 5.8 three steps of the simulated charge evolution are shown for the case of the detection of a 40 MeV ^{12}C ion. The projection of the tridimensional charge densities over the z axis is reported for three different times; the black thick curve corresponds to the initial position of the Bragg peak. In Fig. 5.9 the same case is presented as seen in a bidimensional projection at time $t \simeq 15$ ns. The considered ion corresponds to the experimentally observed “back-bending point” for ^{12}C in Fig. 4.6.

In the early times of the process the macroscopic field begins separating the electron and hole charge densities. When some induced displacement occurs the Coulomb interaction between electrons and holes becomes so important to “stick” together the higher-density part of the two distributions regardless of the macroscopic field action. The applied electric field is now able only to erode charge from the peripheral areas of the space charge (see Fig. 5.9), and this process, together with the diffusion mechanism, gradually removes charge from the high-density region. This situation holds as long as the charge density is high enough to shield the effect of the macroscopic field. Later, when the charge densities are sufficiently reduced, the two charge

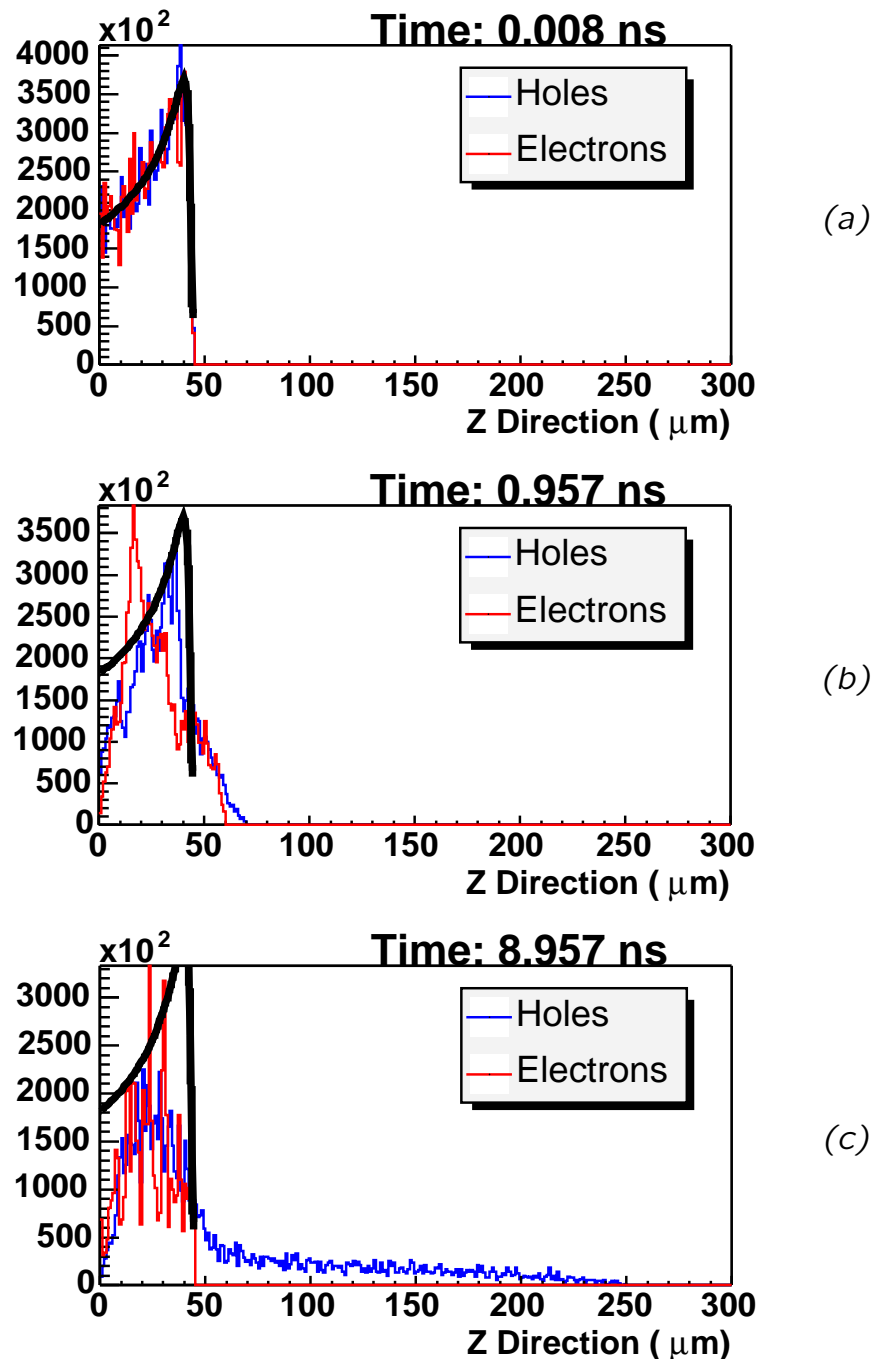


Figure 5.8: Various stages of the evolution of the space charge inside a silicon detector. The electron-hole interaction is powerful enough to screen the macroscopic electric field so that the initial (a) Bragg peak distributions are difficult to separate and collect (b) and plasma erosion occurs (c). See text for details.

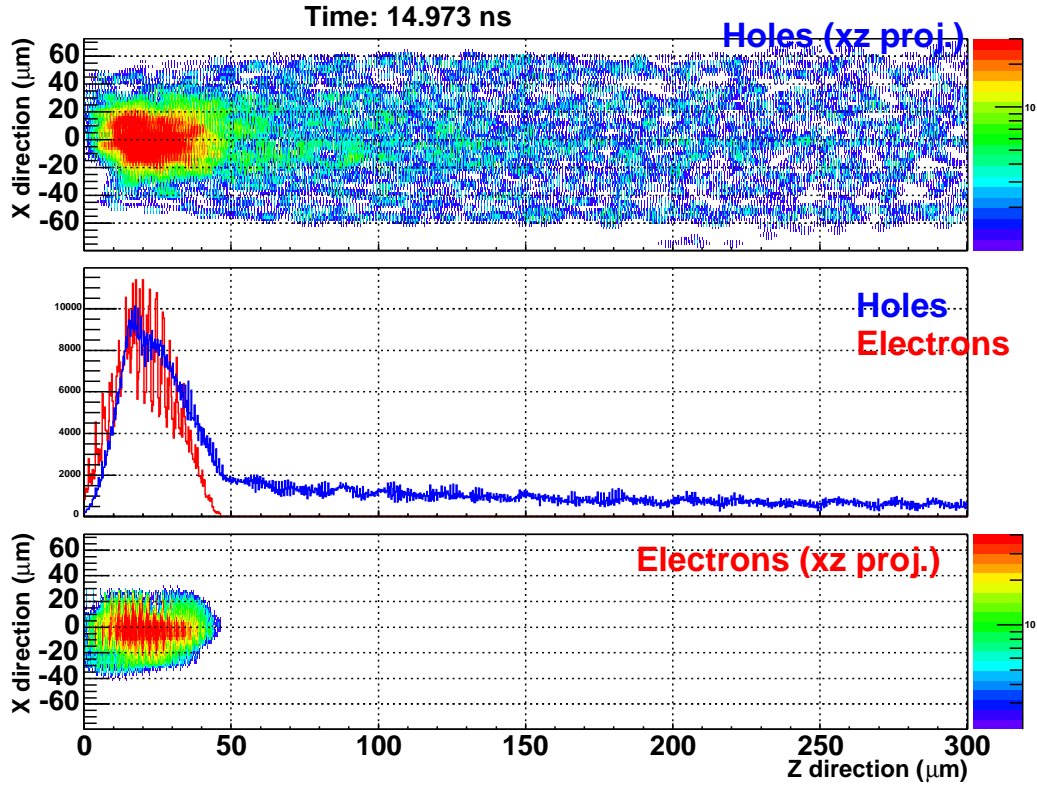


Figure 5.9: Bidimensional $x - z$ projection of the holes (top) and electrons (bottom) charges during the plasma erosion process. The projection of both distributions on the z axis is shown in the middle panel as a reference.

types are separated by the macroscopic electric field and finally collected on the electrodes.

In Fig. 5.10 a correlation plot between the simulated energy and risetime is presented. Two lines corresponding to ^{16}O and ^{12}C are shown: it is interesting to note that the backbending of the experimental lines for low-energy values is reproduced (more details are discussed later). On the same figure simulated points for ^{12}C with no microscopic interaction between electrons and holes are reported (\star symbols): the resulting behaviour is very different with respect to the one simulated with the full interaction: most notably the zero-crossing time variation as a function of particle energy is less important and no significant backbending of Z lines occurs.

Finally a (preliminary) direct comparison with the experimental data obtained in §4.3 is presented in Fig. 5.11. Current signals corresponding to a detection of a ^{16}O particle have been simulated for various

Pulse shape simulation results @ 140V (120V depl.)

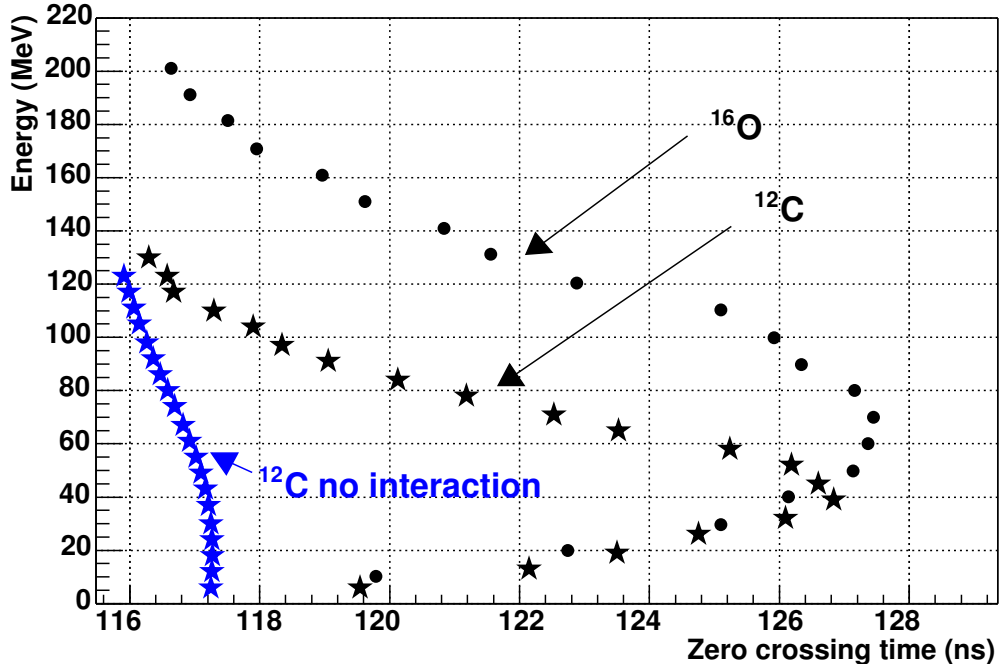


Figure 5.10: Effect of the space charge interactions in the energy versus risetime plane. The simulated points corresponding to ^{16}O (\bullet) and ^{12}C (\star) are shown. For the case of ^{12}C , points simulated with no microscopic interaction are also shown as \star .

incident energies and, after convolution with the measured preamplifier response function, they have been processed with the same digital signal processing algorithms used in the experiment. The simulated points are plotted with \bullet markers superimposed to the experimental data of Fig. 4.6.

The overall agreement with the experimental data is satisfactory, taking also into account that the maximum deviation from the experimental ^{16}O line is of the order of 1 ns or less. The achieved quantitative agreement is a stringent test of the simulation, and it is a clear improvement with respect the semi-qualitative results presented in [78].

From the presented comparison it is possible to recognize that all the main experimental features of the detector are correctly reproduced by the simulation, that is based only on the electrostatic interaction between electrons and holes that are drifting inside the semiconductor. No adjustable free parameters are present in the simulation, so that the obtained agreement can be regarded as an evidence

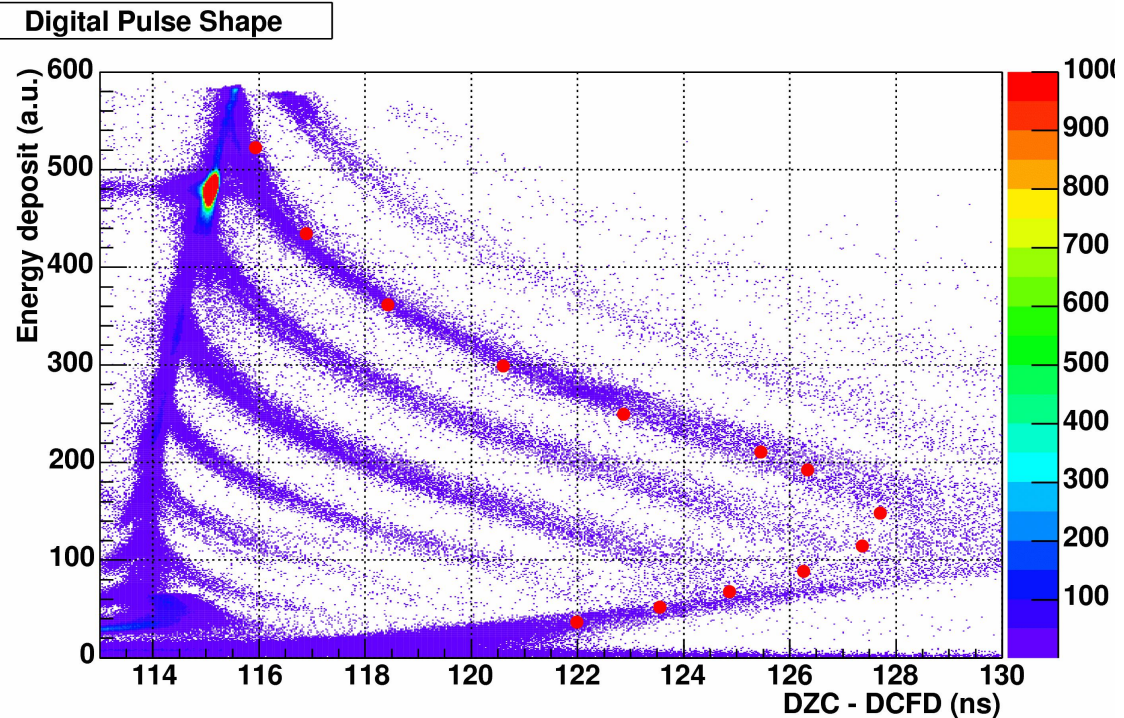


Figure 5.11: Preliminary results of the parameter-free simulation discussed in the text (● markers) as compared with experimental data. A good overall agreement is evident.

for a good understanding of the physics processes underlying charge collection.

The diffusion of carriers plays an important role in the final simulation results, i.e. very different results (still exhibiting backbending but far from agreement with the experiment) are obtained when diffusion processes are switched off in the simulation (or when PMP or FMM methods are used, see previous discussion).

The achieved reproduction of the backbending of Z -lines (that is a somewhat surprising experimental result) makes it possible to describe the processes leading to this behaviour with electrostatic considerations only, taking also into account the comparison shown in Fig. 5.10 between the full simulation and the simulation in absence of electron-hole Coulomb interaction. The collected experimental data can be described within the following scenario (the first two points have been known in literature since decades, at least qualitatively):

- For stopped particles the ionization produced in the Bragg peak is very high and thus the electron-hole Coulomb interactions do

not allow fast collection times, i.e. the signal risetime is longer than the one in absence of microscopic Coulomb interactions. As a consequence, the final charge-collection time depends on the applied electric field, i.e. faster signals are obtained using a higher macroscopic electric field, as for a higher bias voltage.

- Whereas this effect is small for high-energy ions having a Bragg peak located in the strongest electric-field area, a progressive slackening of the signals is expected for lower-energy particles. As the particle energy decreases, the Bragg peak moves towards lower-field regions, where the macroscopic field is less effective in the erosion of the plasma column. From the simulations (see also Fig. 5.9) it is possible to see that the erosion attacks the “surface” of the plasma column, whereas the core is almost unaffected by the low-intensity macroscopic field, due to the screening.
- For even lower energy particles (about 40 MeV for the ^{12}C line in Fig. 5.11) a new charge collection mechanism becomes important, thus altering significantly the behaviour of the identification lines in the energy-risetime plane. We call this mechanism “close electrode” effect. For these low-range particles (less than $\sim 40 - 50 \mu\text{m}$ in Fig. 5.11) the collecting electrode is very close to – almost inside – the core of the ionization column, i.e. the Bragg peak (see also Fig. 5.8). The resulting geometric and electrostatic configuration makes it possible to collect charge directly from the core of the ionization plasma, instead of waiting for the slower erosion processes. In this situation any charge identification capability is jeopardized, because the collection time for a given particle range is almost independent of the particle type. This effect is present for any energy of the incoming particle, but it becomes important (and even the dominant effect) only when the Bragg peak core comes close to the electrode, thus qualifying the mechanism as a mainly geometrical one.

The applied bias voltage to the detector has a little influence on this effect, since the field is perpendicular to the lateral diffusion direction and the electron and hole diffusion coefficients are practically constant for low electric-fields, see Fig. 5.5. Erosion processes are still active and thus a residual small dependence on the applied bias voltage may be present.

The proposed scenario makes use of the same physics processes that have been included in the simulation, namely charge drift and electrostatic interactions. Apart from performing new experiments, a confir-

mation of the proposed scenario can be found in the already known experimental results of nearly independence of the “backbending energy” of the applied bias voltage to the detector. These results have been reported in [54] and, for the digital setup used in §4.3, are shown in Fig. 5.12. The same experimental configuration of Fig. 5.11 has been used, except for different bias voltages to the detector, namely 120 V, 140 V, 160 V (the measured depletion voltage of the used detector is ~ 120 V). Higher bias voltages correspond indeed to faster signal (first point of the previous discussion) whereas the backbending energies are almost unaffected by the applied voltage (“close electrode” effect).

5.7 Conclusions and future developments

In this chapter a microscopic simulation of silicon detectors has been described, aiming at a detailed understanding of the current output from the detector. A description of the main physical processes that are relevant in the detection of a highly-ionizing particle has been presented, together with preliminary simulated results, which show a satisfactory agreement with experimental data. The detector response is reproduced over the tested range of energies and particle charges without any adjustable parameter. The pulse shape properties are interpreted by electrostatic plasma erosion and by a “close electrode” effect, that are responsible for the observed backbending of identification lines.

It has to be noted that the implemented simulation, possibly due to the strong non linearity of the modeled system (see Eq. 5.4), shows an oscillatory behaviour in the simulated space charge (that can be seen in Fig. 5.9, middle panel) and a residual sensitivity to the interpolation method used to extract mobility, diffusion and cluster-cluster interaction strength from tabulated values.

Further work is planned in order to improve the numerical stability of the simulation and to extend the comparison with experiment (an experimental test with heavier beams is planned). The possibility of using a numerical solution of Eq. 5.4 in the continuum (for example using Finite Elements Methods or similar ones) is also envisaged.

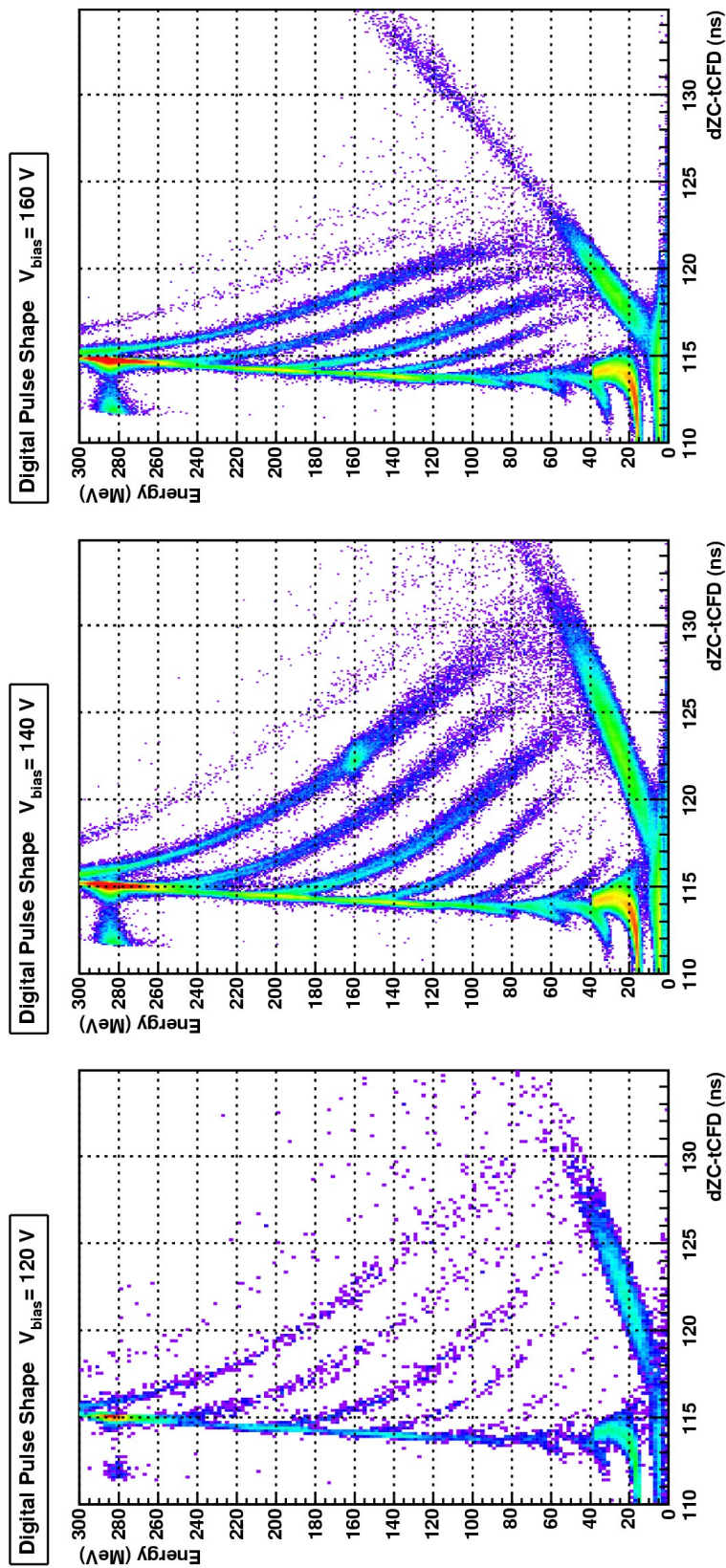


Figure 5.12: Pulse shape identification plots, obtained with the experimental setup of §4.3, for three different detector bias voltages

Chapter 6

Conclusions

During this Thesis an extensive evaluation of digital sampling techniques has been carried out from both theoretical and experimental points of view, in order to understand the limit of applicability of such methods to Nuclear-Physics experiments.

These methods represent an attractive alternative to standard analog processing, due to their flexibility and ease of application to different detection configurations, to the associated reduction in the needed electronics (for example quite sophisticated pulse-shape analyses can be performed with a single module) and to the reduced costs. Analog to Digital converters characterized by resolution and sampling speed adequate for the purposes of high-resolution energy and timing measurements are available on the market only since few years, and an example of a custom digital sampling system (using a 12 bit-100 MSamples/s converter) well suited for practical implementation in large Nuclear-Physics experiments has been presented (both in its prototype and definitive version).

A detailed discussion of the algorithms needed for extracting the desired information from digitized signals has been presented, focusing mainly on energy (i.e. signal amplitude) and time measurements. The ability of performing such measurements allows a complete signal processing of a wide class of Nuclear-Physics detectors, used for example in Nuclear-Reaction or Nuclear-Structure studies. All the proposed algorithms are meant to be used in on-line digital signal processing applications (for example running on a DSP processor) and thus an important point is the ability to extract high-resolution measurements with small processing time.

The case of high-resolution energy measurements has been discussed for the case of digital sampling systems where only a finite time window is available for processing (event-based systems). Detailed calculations as well as simulations have shown that the attain-

able performances are mainly limited by the effective number of bits of the converter and by the available baseline time. An interesting result is the possibility of keeping good energy resolution while applying a baseline subtraction algorithm. Actually a resolution close to the theoretical best value can be achieved with this method by using a baseline time as short as $\sim 6 \mu\text{s}$, i.e. about half the time needed for the shaped signal to reach its maximum. This permits to extend the range of applicability of event-based digital systems also to high energy-resolution experiments (for example γ ray measurements in Nuclear-Structure studies).

The timing properties of digital sampling systems have been studied and original solutions are presented. The results are discussed, taking into account both the AD converter properties and the algorithms used for the extraction of the desired time mark. From the presented discussion and simulation results, it is evident that a timing resolution much smaller than the ADC sampling period can be achieved with a proper interpolating procedure (for example 100 ps FWHM resolution with a 10 ns sampling period converter, experimentally verified). A detailed discussion of several interpolating kernels has been presented, taking into account their contribution to the final performances as well as the need for fast algorithms to be used for on-line signal processing. These results have been included in two Constant Fraction-like algorithms to be used for high-resolution timing of pulse-shape analyses for example in Nuclear-Reaction studies. An original method for the synchronization of many digital acquisition channels has been also presented, to be used in those experiments where high-resolution time-of-flight (mainly for Nuclear Reactions) or coincidence (mainly for Nuclear Structure) measurements are needed.

The presented algorithms have been experimentally tested with various detector types in order to better understand their properties and the factors that, in each case, are limiting the achievable performances. Tests have also been performed to check whether a digital sampling system can be used for effective replacement of the standard analog measurement techniques. Using a beam test at Laboratori Nazionali di Legnaro (LNL) and several laboratory tests with small radioactive sources, it has been possible to study energy, timing and pulse-shape analysis performances of digital sampling systems using silicon and germanium solid-state detectors, organic and inorganic scintillators, and Gas detectors. The achieved results demonstrate that, using the proper signal processing algorithms, a digital sampling system can be effectively used in many Nuclear-Physics applications. The today available AD converters make it possible to replace standard analog systems in almost all the considered cases.

Pulse-shape applications in silicon detectors require a good understanding of the physics underlying charge-collection processes in the detector. A microscopic simulation of current signals induced by the detection of highly ionizing particles has been presented and compared with experimental data. A good agreement between the two has been obtained with no free adjustable parameters, so that a successful description of the detector signals is obtained.

Further work is planned in order to study the performances of digital sampling systems over wider dynamic ranges, for example using experimental tests with heavy beams (the already performed tests are limited to $Z \sim 8$). In particular, a deeper study of pulse-shape applications (for example in silicon detectors) as well as time-of-flight measurements is planned. The possibility of studying novel digital processing algorithms is also envisaged, due to the greater processing capabilities of digital sampling systems with respect to analog ones.

Index

Symbols

- $\Delta E-E$ method 86
 $\Sigma - \Delta$ ADCs 26

A

- ADC 23
ADC input range 24
aliasing 31, 32, 41
analog mixing 77
analog pipelining 26
analog to digital converter 44
antialiasing filter 32, 41, 71, 73, 107–109
ArcCFD 20, 76
assembler 38

B

- ballistic deficit 19
bandlimited signal 29
baseline subtraction 50, 87, 89, 91
baseline time 45, 46
Bethe-Bloch formula 7
biquad digital filter 36
Bragg peak 7, 116, 127

C

- canonic form implementation 36
CFD 19
charge-sensitive preamplifier 13
circular buffer 38, 45
clock 24
coincidence measurements 77
Compton continuum 9

- Compton scattering 8
constant fraction timing 19
continuously running systems 45, 52
convolution 29
Coulomb interaction 115, 123, 124, 126, 127, 130, 134, 135
CR–RC shaping 17
CR–RC⁴ shaping 17, 46, 51, 54, 57
CsI detector 10, 14, 15, 57–59, 61, 86, 88–90, 101, 102
cubic interpolation 57, 63, 64, 68, 69, 71–73, 76, 91, 93, 101, 107

D

- DAC 23, 27
dArcCFD 76, 97, 100, 107
dCFD 69, 70, 73–76, 85, 91–93, 96, 97, 106–108
delay line 38
depletion voltage 120
differential evolution 60
differential non-linearity 25
diffusion coefficient 121–125, 127–130, 134–136
digital deconvolution 79
digital filters 34, 79
digital replica of a spectroscopy amplifier 59
digital semigaussian shaping 87, 91
digital signal processors 37

-
- digital to analog conversion 27
 digital zero-crossing 91
 Dirac delta 30
 direct form I 36
 direct form II 36
 dithering 33, 56
 DSP 37–39, 42–45, 59–61, 72,
 77, 78, 81, 85, 95
 dynamic range 87, 90, 101–103
 dZC 91–93
- E**
- effective number of bits 24, 25,
 32–34, 54–56, 65, 70, 80,
 87, 91, 97, 99, 140
 energy resolution 52
 ENOB 25
 entertainment systems ix
 ergodic hypothesis 49
 event-based systems 44–46, 52,
 53, 56
- F**
- FAIR 43
 Fano factor 13
 fast plastic scintillator 99, 106
 fast-slow pulse shaping 89, 102
 FFT 29
 FIR 34
 first photoelectron timing 107
 flash ADCs 26
 Fourier transform 28, 62
 FPGA 38, 44, 45
 fractional delay 76
- G**
- GARFIELD 43, 59
 gas multiplication 12
 genetic algorithm 60
 germanium detector 13–15, 17,
- 19, 22, 44, 54, 57, 97–100
- I**
- IIR 36
 IIR digital filters 35
 infinite-cusp shaping 17
 integral non-linearity 25
 interpolation kernel 32, 62
 isospin 2
- K**
- Klein-Nishina formula 9
- L**
- Laboratori Nazionali di Legnaro 85,
 95, 140
 least significant bit 24
 linear interpolation 63
 lookup table 82, 90, 112
 low-frequency noise 46
 LSB 24
- M**
- MAC 37
 missing codes 25
 MMX 37
 mobility of carriers 121, 125, 136
 modular system 42
 moving average 35
 multicore architecture 38
- N**
- NaI detector 109
 neutrons 9
 noise-to-signal-ratio 66
 Nyquist frequency 29, 51, 63, 73
- P**
- pair production 8
 Parseval's theorem 29
 peak Sensing 59

- phoswich detector 110
 photoelectric absorption 8
 photoelectron 8
 photomultiplier 10
 pipelined flash ADCs 26, 40
 poles of a digital filter 36
 position sensitivity 104
 preamplifier noise density 13
 PSA 15, 76
 PSPPAC 12, 103
 pulse shape 14–16, 21, 57, 90–92,
 97
- Q**
- QDC 17
 quantized filter 60
 quenching 14
- R**
- radio-frequency 95
 range of a charge particle 7
 rear side injection 90
 ROOT 82
 rule of thumb 40
- S**
- sample and hold 41
 sampling comb 30, 63
 sampling frequency 24
 sampling period 24
 sampling theorem 31, 62, 66, 68,
 69
 SAR 26
 scintillation detectors 9
 SCT 101
 shaping parameters 17
 shift register 45
 signal interpolation 32, 57,
 58, 62–72, 75–77, 93, 107,
 108
 signal-mixing electronics 95
 silicon detector x, 7, 8,
 13–15, 17, 44, 67, 86, 87,
 90–96, 101, 102, 115–126,
 129–131, 136
 silicon detector simulation 115
 SIMD 37
 single or dual slope ADCs 25
 single-chip telescope 101, 103
 SNR 16, 25
 spectral noise density 14, 34, 53
 SSE 37
 successive-approximation ADCs 26
- T**
- TAC 77
 time of flight 21, 77, 95, 96
 timestamped clock 77, 81
 timing measurements 62, 106
 trigger-based acquisition 43
- V**
- VME 43
- Z**
- Z transform 29
 Z transform poles 29
 zeros of a digital filter 36

Bibliography

- [1] L.Bardelli, Diploma Thesis, 2001, University of Florence.
- [2] L.Bardelli *et al.*, Nucl. Instr. and Meth. **A 491** (2002) 244.
- [3] L.Bardelli *et al.*, *Application of a fast digital sampling system to $\Delta E/E$ identification and subnanosecond timing*, Laboratori Nazionali di Legnaro Annual Report 2002.
- [4] L.Bardelli *et al.*, Proc. of RNB6 Conf., 2003, Nucl.Phys. **A 746** (2004) 272.
- [5] L.Bardelli *et al.*, Nucl. Instr. and Meth. **A 521** (2004) 480.
- [6] L.Bardelli *et al.*, Proc. of the IWM2003 Workshop, 5th-7th November 2003, Ganil, France.
- [7] L.Bardelli *et al.*, Proc. of NPL 2003 workshop, 28th April 2004, National Physics Laboratory, Teddington, UK.
- [8] L.Bardelli *et al.*, Proc. of IEEE2004 conference, 16th-22nd October 2004, Rome, Italy.
- [9] L.Bardelli *et al.*, Proc. of the 5th Italy-Japan meeting, 3rd-7th November 2004, Naples, Italy, to app. in World Scientific.
- [10] Final report of the EURISOL project (European Isotope Separation On-Line Radioactive Ion Beam Facility), available on <http://www.ganil.fr/eurisol/>.
- [11] G.Casini, *et al.*, Eur. Phys. J. **A 9** (2000) 491.
- [12] S.Piantelli, *et al.*, Phys. Rev. Lett. **88** (2002) 052701.
- [13] R.D.Evans, *The Atomic Nucleus*, Krieger, 1982.
- [14] G.F.Knoll, *Radiation detection and measurement*, John Wiley & Sons, 1989.

- [15] M.Bini, *et al.*, Nucl. Instr. and Meth. **A 515** (2003) 497.
- [16] G.Poggi, *Appunti sul rumore elettrico*, 2002, unpublished.
- [17] F.N.H.Robinson, *Noise and fluctuations in electronic devices and circuits*, Clarendon Press, 1974.
- [18] Technical proposal for the "Advanced GAMMA Tracking Array" (AGATA) project, available on <http://agata.pd.infn.it/>.
- [19] M.A. Deleplanque *et al.*, Nucl. Instr. and Meth. **A 430** (1999) 292.
- [20] E.Kowalsky, *Nuclear Electronics*, Springer–Verlag, New York, 1970.
- [21] P.W.Nicholson, *Nuclear Electronics*, Wiley, London, 1974.
- [22] M.Bertolaccini, C.Bussolati, and E.Gatti, Nucl. Instr. and Meth. **41** (1966) 173.
- [23] D.A.Gedcke, W.J.McDonald, Nucl. Instrum. Meth. **55** (1967) 377.
- [24] R.L.Chase, Rev.Sci.Intrum. **38** (1968) 1318.
- [25] J.J.Kozyczkowski and J.Bialkowsky, Nucl. Instrum. Meth. **137** (1976) 75.
- [26] Analog Devices, *Fundamentals of Sampled Data Systems*, Application note AN-282.
- [27] P.Horowitz W.Hill, *The Art of Electronics*, Cambridge University Press, 1989.
- [28] H.Taub, *Digital Integrated Electronics*, McGraw-Hill, 1977.
- [29] A.V.Oppenheim and R.W.Shafer, *Digital Signal Processing*, Prentice Hall, 1975.
- [30] Steven W. Smith, *The Scientist and Engineer's Guide to Digital Signal Processing*, available on <http://www.dspguide.com/>.
- [31] H. Nyquist, *Certain factors affecting telegraph speed*, AT&T, 1924 and *Certain topics in telegraph transmission theory*, Trans-

- actions of the American Institute of Electrical Engineering **47** (1928) 617.
- [32] G.Goertzel, *An algorithm for the evaluation of finite trigonometric series*, American Math. Montly, **65** (1958) 34.
- [33] A.V.Oppenheim, A.S.Willsky, S.H.Nawab, *Signals and systems*, Second Edition, Prentice Hall, 1997.
- [34] E.Brandt, *Statistical and Computational Methods in Data Analysis*, North Holland, 1983.
- [35] B.W.Kernighan, D.M.Ritchie, *the C programming language*, Prentice Hall, 1978.
- [36] J.Millman A.Grabel, *Microelectronics*, McGraw-Hill, 1994.
- [37] G.Pasquali, private communication.
- [38] T.Quarles, A.R.Newton, D.O.Pederson, A.Sangiovanni-Vincentelli, *SPICE3 Version 3f3 User's Manual*, University of California, 1993.
- [39] M.Bini, R.Ciaranfi, G.Pasquali, *to be published*, 2004.
- [40] F. Gramegna et al., Nucl. Instr. and Meth. **A 389** (1997) 474.
- [41] Motorola, *The VMEbus Specification Manual*, revision C.1, October 1985.
- [42] A.Ordine et al., IEEE Trans. Nucl. Science, **45** no.3, (1998), 873.
- [43] E. Gatti et al., Nucl. Instr. and Meth. **A 523** (2004) 167.
- [44] M.Pârlig, et al., Nucl. Instr. Meth., **A 482** (2002) 674.
- [45] The MINUIT minimization package, CERN, WEB page: <http://www.cern.ch/>.
- [46] R.Storn et al., *Differential Evolution Algorithm*, WEB page: <http://www.icsi.berkeley.edu/~storn/code.html>.
- [47] *Improving ADC Resolution By Oversampling and Averaging*, CYGNAL Application note AN018, available on <http://www.cygnal.com/>.
- [48] The ROOT analysis framework, WEB page: <http://root.cern.ch/>.

- [49] C.J.Crannel, R.J.Kurz, W.Viehmann, Nucl. Instrum. Meth. **115**, (1974) 253.
- [50] J.Poutas *et al.*, Nucl. Instr. Meth., **A 357** (1995) 418.
- [51] C.A.Ammerlaan *et al.*, Nucl. Instr. and Meth. **22** (1963) 189.
- [52] G.Pausch *et al.*, Nucl. Instr. and Meth. **A 365** (1995) 176.
- [53] M.Mutterer *et al.*, IEEE Trans. Nucl. Science, **47** no.3 (2000), 756.
- [54] G.Pausch *et al.*, IEEE Trans. Nucl. Science, **44** no.3 (1997) 1040.
- [55] A.Pagano *et al.*, Proc. of IEEE2004 conference, 16th-22nd October 2004, Rome, Italy.
- [56] N.Taccetti *et al.*, Nucl. Instr. and Meth. **A496** (2003) 481.
- [57] Timing performances of GMX30p series, ORTEC, WEB page: <http://www.ortec-online.com/>.
- [58] G.Pasquali *et al.*, Nucl. Instr. and Meth. **A 301** (1991) 101.
- [59] F.J.Lynch, IEEE Trans. Nucl. Sci. **NS-13** no.3 (1996), 140.
- [60] C.Hohenemser, R.Reno and A.P.Mills, IEEE Trans. Nucl. Sci. **NS-17** no.3 (1970), 390.
- [61] A.Schwarzschild, Nucl. Instr. and Meth. **21** (1963) 1.
- [62] E.Gatti and V.Svelto, Nucl. Instr. and Meth. **30** (1964) 213.
- [63] G.Present *et al.*, Nucl. Instr. and Meth. **31** (1964) 71.
- [64] M.Bertolaccini *et al.*, Nucl. Instr. and Meth. **51** (1967) 325.
- [65] J. Alarja, *et al.*, Nucl. Instr. and Meth. **A 242** (1986) 352.
- [66] D.W. Stracener, *et al.*, Nucl. Instr. and Meth. **A 294** (1990) 485.
- [67] R.T. De Souza, *et al.*, Nucl. Instr. and Meth. **A 295** (1990) 109.
- [68] Jacoboni *et al.*, Solid State Electron., **20**, 2(1997), 77.
- [69] SRIM software, WEB page: <http://www.srim.org/>.
- [70] G.Cavalleri *et al.*, Nucl. Instr. and Meth. **92** (1971) 137
- [71] Z.He, Nucl. Instr. and Meth. **A 463** (2001) 250.

- [72] F.Hubert *et al.*, Nucl. Instr. and Meth. **B 36** (1989) 357.
- [73] E.Bertschinger and J.M.Gelb, *Cosmological N-body simulations*, Computers in Physics, Mar/Apr 1991, 164.
- [74] L.Greengard and V.Rokhlin, *A fast algorithm for particle simulations*, J.Comp. Phys, **73** (1987) 325.
- [75] DPMTA - Distributed Parallel Multipole Tree Algorithm, WEB page <http://www.ee.duke.edu/~wrankin/Dpmta/>.
- [76] J.D.Jackson, *Classical Electrodynamics*, Wiley; 3 edition (July 27, 1998).
- [77] PVM, Parallel Virtual Machine library, WEB page: <http://www.csm.ornl.gov/pvm/>.
- [78] H. Hamrita *et al.*, Nucl. Instr. and Meth. **A 531** (2004) 607.